INTERNATIONAL SCHOOL FOR ADVANCED STUDIES

DOCTORAL THESIS

COMPETING INTERACTIONS IN CORRELATED HETEROSTRUCTURES

Author:	*Supervisor:*
Francesco PETOCCHI	Prof. Massimo CAPONE

A thesis submitted in fulfillment of the requirements

for the degree of Doctor of Philosophy

in

Condensed Matter Theory

To my daughter

CONTENTS

INTRODUCTION

In the last decade, the field of heterostructures involving transition-metal oxides as building blocks has grown to become one of the most active areas in the field of correlated materials and, more in general, in condensed matter. The interest in these systems is motivated by the possibility to artificially design and manipulate electronic phases inaccessible in the bulk constituents. The prototypical and most studied heterojuncion is formed by the two band insulator $LaAlO_3$ (LAO) and $SrTiO_3$ (STO) where an insulator-metal transition occurs at the interface as a function of the thickness of the LAO layer. When the latter exceeds a universal threshold, a few-layer thick two-dimensional electron gas establishes on the STO side. A similar phenomenology is realized at the interface between STO and the Mott insulator $LaTiO_3$. In both cases the 2DEG turns into a superconductor at $300mK$. The phenomenology of these systems, which are only an example of the many opportunities offered by heterostructures formed by transition-metal oxides and correlated materials, reveals immediately that a number of physical effects conspire to determine their fascinating properties. Electron-electron correlations are certainly expected to play a role because of the narrow bands arising from the d electrons of transition-metal oxides. Moreover, there are strong evidences of an important role of electron-phonon coupling already in bulk STO, and the phonon-driven interaction is the most likely candidate for the two-dimensional superconductivity found at the interfaces. Moreover, an important role of spin-orbit coupling is expected at interfaces, and it will be particularly important for 5d systems like iridates. All these competing interactions should be treated on the same footing without assuming a clear hierarchy in order to disentangle their effects in the rich phenomenology. This means that any theoretical treatment should be able to handle competing interactions. This can be realized using the Dynamical Mean-Field Theory, a powerful approach which freezes spatial fluctuations in order to fully account for the local quantum dynamics arising from the different relevant interactions. In order to treat layered systems, Dynamical Mean-Field Theory must be extended in order to allow for different physics on different layers. In this thesis we contribute to the theoretical understanding of heterostructures of transition-metal oxides and correlated materials touching all the above-mentioned points. We now briefly introduce the structure of the thesis and the content of the different chapters. The first Chapter is devoted to an introduction about transition-metal heterostructures with some emphasis on the LTO/STO and LAO/STO systems. In the second Chapter we introduce the several theoretical models we use in the rest of the thesis, namely single-band and multi-band Hubbard modeling of strong correlations, electron-phonon interaction and spin-orbit coupling.

Chapter 3 briefly introduces DMFT and its extensions to treat all the interactions discussed in the second Chapter.

The fourth chapter contains a novel extensions of DMFT to layered systems which minimizes finite-size effects and approximation, as well as an application of the method to the attractive Hubbard model, which allows us to study the proximity effects as a function of the various model parameters.

In Chapter 5 we discuss the interplay between strong correlations and electron-phonon interaction, identifying the conditions under which an s-wave superconductor can be realized in the presence of strong correlations. An application to a model version of the LTO/STO system is presented.

Finally, in Chapter 6 we study the interplay between strong correlations, Hund's coupling and spin-orbit interaction in a three-fold degenerate model for d electrons. A study of the magnetic phase of the iridate compound Sr_2IrO_4 is finally presented.

All these result contribute to improve our understanding of the complex interplay underlying the physics of transition-metal oxides and will represent the basis to build a more complete modelization of there systems.

CHAPTER

1

INTERFACE PHYSICS

The surface of a material, or the interface with a different compound can display electronic properties far different from the bulk. Even a clean and regular surface can induce remarkable effects associated to the breaking of the translational and rotational symmetries. One of the most obvious effects is the reduction of the effective kinetic energy at the surface due to the missing bonds, but also the crystal fields are modified, leading to the lifting of degeneracy between different orbitals. An interface between two materials also leads to stress and strain, which further complicates the theoretical study of these systems. Furthermore, interfaces often host disorder effects of different origin: point defects, dislocations and stacking faults tend to be incorporated into the lattice with their own electronic or magnetic properties and may act as scattering centers. Hence also the chemical composition may change close to the interface. The relevance of these phenomena obviously depends on the specific microscopic properties of different surfaces or interfaces, leading to an immense variety of physical responses. The huge variety of control parameters also leads to the opportunity to design systems in order to optimize some properties.

This scenario becomes even richer if we consider materials with sizable interaction leading to strong correlation effects, like transition-metal oxides (TMOs). Since the electronic states are altered at interfaces, their correlations might be strongly modified as well, resulting in a dramatic change of the collective electronic and magnetic properties, which can also lead to a completely different phenomenology of the interface with respect to the bulk constituents. An interface-driven reduction of the electronic screening is expected to enhance the correlation effects driven by the Coulomb interaction, but, on the other hand theon-site Coulomb energy U can be lowered by several eV if the screening is enhanced by image charges, as is the case of an interface between a TMO and a conventional metal[4, 28]. In $La_xCa_{1-x}VO_3$, for example, due to the reduced atomic coordination, the bands are expected to be narrowed at the surface, thus the ratio of U/W is expected to be enhanced and, for a range of dopant concentrations x, these compounds display insulating surfaces while the bulk is metallic[47]. Conversely, at the interfaces or surfaces of Mott/band-insulators, since U or the charge transfer gap Δ may decrease to values smaller than the bandwidth W, a phase transition to a metallic phase may be initiated[4]. Interface effects might be exploited to assess specific requirements of electronic devices without degrading the bulk, for example creating ferromagnetic interfaces in between lattices whose groundstate is naturally antiferromagnetic[80]. Another set of correlated system in which the interface has an electronic phase different from the bulk are junctions involving TMOs. Surprisingly at the interface between two insulating TMOs a high-mobility electron gas arise which, at low enough tmeperature, may also become superconducting [10] as will be explained in the following.

In the following sections we briefly review first some basic properties of interfaces involving copper-based high-temperature superconductors (cuprates) and then we give a broad overview of interfaces between transition-metal oxides, in order to provide a general introduction of the main ideas of the experiments that motivate the theoretical work reported in this Thesis.

1.1 Some basic aspects of interfaces of high-temperature superconductors

The high-temperature superconductors are arguably the most studied compounds in the last decades. Despite the lack of a consensus on a general theory for these materials, their phase diagram is well established. This is not the place for a comprehensive review of these materials, but we limit ourselves to remind that superconductivity emerges by doping holes into an antiferromagnetic charge-transfer insulator, whose existence is a consequence of the strong Coulomb repulsion. The whole phase diagram is believed to derive from the physics of strong correlations, including the elusive pseudogap region, where the system has a spectral gap, but it is no longer superconducting, and the d-wave symmetry of the order parameter, with nodes in the gap function. The superconducting properties of the cuprates are indeed strongly affected by interfaces due to the short superconducting coherence lengths, which are comparable with the size of the unit cells, and the sensitivity on defects [26]. A further reason is the key role of the electronic density in determining the critical temperature. Therefore any mismatch in the carrier density can lead to huge changes in the superconducting properties, as it is realized at interfaces between high-Tc superconductors and conventional metals such as silver or gold[54, 27].

1.1.1 Influence of the order parameter on the interface

The superconducting order parameter in the cuprates is almost universally a robust $d_{x^2-y^2}$ symmetry[87, 86], with nodal lines in the Brillouin zone, which reflects in a precise symmetry of the oder parameter in real space. The electronic phase at an interface is strongly affected by this symmetry, in particular when the junctions between different grains have a finite angle. In this case the lobes of the order parameter connect each other with misorientation and the superconducting coupling across the junction is damped with increasing angle[77, 6]. Such characteristics have never been reported for Josephson junctions built from conventional s-wave superconductors, and imply the existence of areas with negative critical current[34], which is easily understood in terms of the above arguments. The sign-difference between the phases of neighboring lobes of the $d_{x^2-y^2}$-wave shift the local phase differences by π, resulting in a negative Josephson current: $J = J_c \sin(\phi + \pi)$.

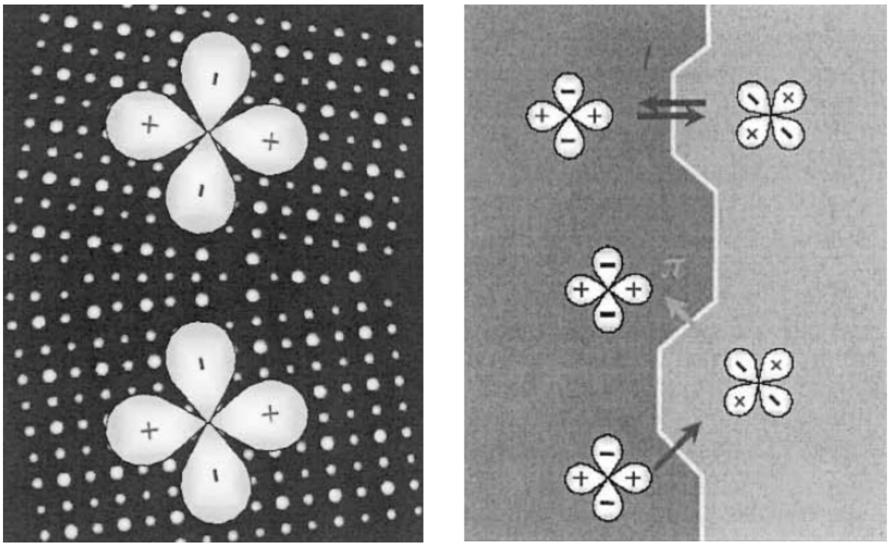

Figure 1.1: (right) Schematic view of the $d_{x^2-y^2}$ order parameter configuration at a grain boundary with a symmetric [001]-tilt misorientation of 15°; (left) sketch of a misoriented interface between the superconducting lobes showing how the additional phase shift of π can induce a backward current across the junction

In this kind of misoriented junctions, the order parameter is strongly suppressed as a combined effect of the short coherence length[6, 35] and of the orientation of the adjacent grain. Among the consequences of the order parameter symmetry there is the occurrence of bound states in the barrier and midgap states at zero energy[38]. All these observations confirm the expectation that the superconduciting properties of cuprate junctions are strongly influenced by the interfaces and their detailed geometry, much more than what happens in conventional s-wave Josephson junctions.

1.1.2 Band Bending

The bending of the electronic band structure induced for example by local variations of the work function can lead to charge-transfer processes[83]. A precise description of the modification in the interface electronic properties due to charge transfer processes is hard to develop: the length scales involved, the electrostatic screening length, the inverse of the Fermi vector $^{1}/_{k_F}$, and the coherence lengths are all comparable to the lattice-spacing. This invalidate the average approaches typically used to define charge and potential distributions. An alternative method to assess the charge-transfer effects relies on the microscopic description of the pairing mechanism, which is still missing. On the other hand, it is known experimentally that the band bending and the associated charge transfer lead to an insulating interface at a grain boundary[48] and transport is expected to occur by tunneling.

1.2 Interfaces between Transition-metal oxides

Transition-metal oxides occupy a special place in the field of material science because they offer a huge variety of physical properties, which ultimately arise from the strong correlation properties associated to the electrons populating the narrow $3d$ bands of the transition metal ions, while the p-bands are fully populated because of the large electronegativity of oxygen (even if there are notable exceptions in which the p orbitals play an active role, especially in "late" transition metal oxides such as cuprates or nickelates). The intrinsic correlation effects experience by these electrons lead to a local entanglement of charge, spin, orbital and lattice degrees of freedom. Within this picture, electrons collective behavior result in a complex plethora of emergent phenomena such as Mott insulators and different long-range ordered phases of different kind, ranging from superconductivity to magnetism and more exotic phases. The word of transition-metal oxides is also very rich, and it allows to handle and control these emergent phases by means of artificially grown heterostructures tailored to optimize known phenomena or to give rise to new and surprising results. The lowered symmetry at the interface clearly favors the appearance of broken symmetry phases which can not occur in the bulk system. Indeed, in several cases, these emergent phase have a two-dimensional nature, where electronic correlation are enhanced by a local reduction of the competing kinetic energy. A common feature in many TMOs directly follows from the common ABO_3 perovskite crystal structure where the transition metal is surrounded by six oxygens located at the vertex of an octahedron. As will be discussed in detail, this structure produce a crystal field splitting that pushes the e_g orbitals ($d_{x^2-y^2}$ and $d_{3z^2-r^2}$) at a much higher energy than the three-fold degenerate t_{2g} orbitals (d_{xy}, d_{yz} and d_{zx}) as in fig.[1.2].

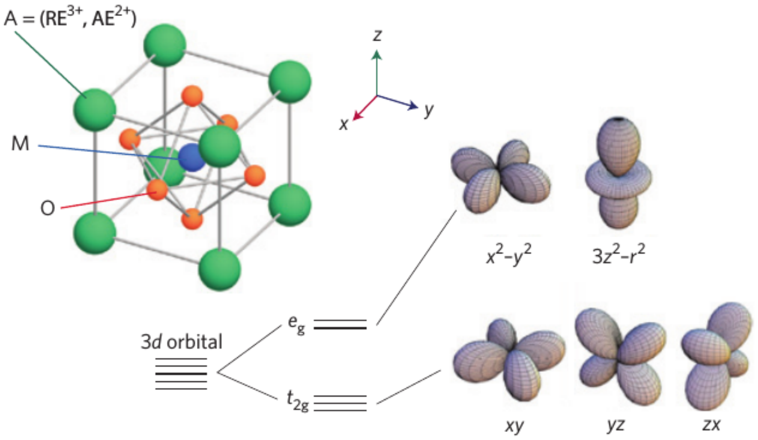

Figure 1.2: Effect of the cubic crystal field splitting on d orbitals

In "early" TMOs, where the valence bands are of pure t_{2g} character, and their radial distribution leads to a vanishing overlap with the interstitial oxygen p

orbital because of the different parity. Therefore the p bands can only be visited through virtual processes eventually leading to a ferromagnetic or antiferromagnetic superexchange across the interface. Another effect which makes interfaces different from the bulk counterparts is the increased relevance of relativistic effects like Spin Orbit Coupling (SOC) which is another topic that will be addressed in the present thesis. The emergence of SOC within this context can be naively understood in terms of the electric field induced by the broken inversion symmetry induced by the surface. A moving electron will therefore experience a magnetic field causing the precession of the spin. This is the well-known Rashba SOC, which adds to the more intrinsic SOC arising from the coupling between atomic spin and orbital angular momentum, which is not so large in TMO, but it becomes very important for $5d$ compounds such as iridates and osmates. In the final chapter of this thesis we will address the interplay between SOC and strong correlation effects, including the Hund's coupling at a simple model level, a necessary step before considering the more involved and realistic situation of the Rashba coupling at strongly correlated interfaces.

1.2.1 Controlling factors

1.2.1.1 Strain and interdiffusion

Any interface implies a lattice mismatch, tipically $\sim 1-2\%$, which leads to compressive or tensile strain on each of the constituents. This effect can be enhanced by atomic reconstruction at a surface and it leads to a modulation of the hopping amplitude and to a a lifted orbital degeneracy. This can result in strong modification of the electronic phase such in $La_{0.7}Ca_{0.3}MnO_3$. For this compound it has been demonstrated that the compressive strain induced by the growing substrate can bring the groundstate from metallic to insulating, while no such effect occur with tensile strain[12, 11]. Due to similarities in size and chemical bondings, the interdiffusion of ions is another feature that can strongly influence the interface properties especially when layers are thinner than $10\dot{A}$[46].

1.2.1.2 Atomic and electronic reconstruction

The Mott transition is controlled by the ratio between the screened Coulomb repulsion and the electronic bandwidth. The latter is controlled by the interatomic distance and by the geometrical arrangement of atoms. Both control parameters are expected to change at a surface or an interface because of its reconstruction. In the case of a surface layer the reduced number of neighboring atoms (coordination number) results in a reduced kinetic energy and a consequent increase of the effect of the interaction. On the other hand, a change in screening may diminish the effective U controlling the charge transfer gap[29, 3]. The change may become larger, for a TMO-normal metal interface or smaller, for a TMO-vacuum interface. For example experiments on the compound $Ca_{1.9}Sr_{1.1}RuO_4$ have shown that the surface undergoes a Mott transition at $T_c \sim 125K$ while the bulk remains metallic only until $T_c \sim 150K$. This deviation from the bulk behavior has been explained noticing that the RuO_6 octahedra have a smaller tilt angle at the surface, this decrease the $Ru - O$ distance therefore enhancing the orbital overlap and the bandwidth.

The TMO heterojunctions with the ABO_3 perovskite structure are influenced by another kind of reconstruction that involve mainly electronic degrees of freedom. Electronic reconstruction may occur in a different way depending wether in the presence of an interface or a surface. In the latter case, a charged polar layer may emerge from an insulating bulk, as in the case of $LaTiO_3$[60]. In junctions between TMO's charge leakage from one compound to another may induce an electronic density different from the bulk in the interface region.

This is the case of the two-dimensional electron gas (2DEG) at the interface of two insulating oxides $LaTiO_3$ (LTO) and $SrTiO_3$ (STO)[60]. The electronic configuration of bulk LTO is one d-electron per Ti atom, owing a Mott insulating state at a commensurate filling, while STO is a band insulator. The two compounds have substantially the same crystal structure and lattice constant, then strong atomic reconstruction effects can be safely ruled out leaving only electronic reconstruction to be accounted for the interfacial properties. Naively one could expect the electronic reconstruction to lead to doped band and Mott insulators in the layers close to the interface. The details of this process and the properties of the emerging two-dimensional electron gas are far less intuitive and proved very hard to theoretically tackle.

1.2.2 Two-dimensional electron gas at the LAO/STO interface

One of the most exciting phenomena at oxide interfaces is the electronic reconstruction that results in the creation of an interfacial electron gas occurs at the interface between $LaAlO_3$ (LAO) and STO[59, 7, 21, 67]. This is one of the most studied junctions involving TMO's due to his robustness agains degradation and the east growth of these two large bandgap insulators ($5.6eV$ for LAO and $3.2eV$ for STO) on the substrate. In their bulk electronic configurations those two TMO are band insulator with ABO_3 perovskite structure. For this class of compounds, the crystal in the 001 direction can be divided into AO and BO_2 alternating planes. Considering the oxygen formal valence of -2, only a finite set of cations can be used in order to preserve charge neutrality in the bulk unit cell. In this framework the STO consists of subsequent neutral planes of $Sr^{+2}O^{-2}$ and $Ti^{+4}O_2^{-4}$, while LAO has alternating net charges $La^{+3}O^{-2}$ and $Al^{+3}O_2^{-4}$, resulting in a polar discontinuity at the interface that introduces a large energy cost for atomically abrupt junction. How the system responds to this energy cost can be understood in terms of a simple electrostatic model for interfacial reconstruction.

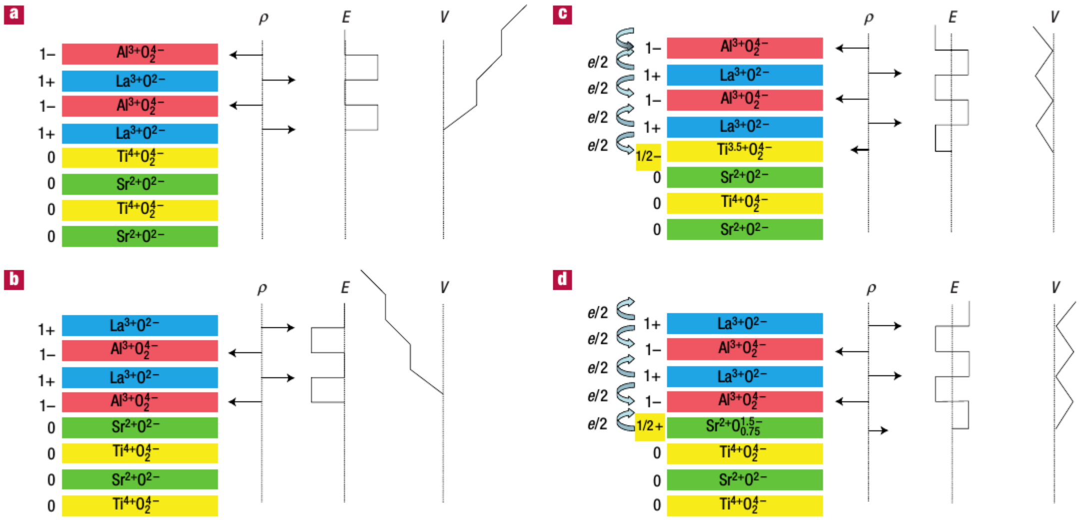

Figure 1.3: (a) Unreconstructed n-type interface showing schematically the non-negative electric field (E), leading to an electric potential (V) that diverges with thickness. (b) Unreconstructed p-type interface where the potential diverges negatively. (c) The divergence catastrophe at the n-type interface can be avoided if $1/2$ electron per unit cell is added to the last Ti layer. This produces an interface dipole that causes the electric field to oscillate about 0, and the potential remains finite. The uppermost AlO_2 layer would be missing $1/2$ electron, which would bring the electric field and potential back to zero at the upper surface. (d) The divergence for the p-type interface is avoided by removing $1/2$ electron per unit cell from the SrO plane in the form of oxygen vacancies.

Depending on the extremal planes, the polar junction can be *n-type* $\left(AlO_2^{(-1)}/LaO^{(+1)}/TiO_2^{(0)}\right)$ or *p-type* $\left(AlO_2^{(-1)}/SrO^{(0)}/TiO_2^{(0)}\right)$, and in both cases an alternating electric field, generated by the layer net charge, leads to an electrostatic potential that diverges with the thickness. For an abrupt interface the bare dipole is $D_o = -0.5e \times c_{LAO} = -1.9e\mathring{A}$ that, in terms of electrostatic potential, gives a potential drop of $\Delta V = 15V$ per each LAO unit cell. For comparison, this would exceed the LAO band gap just with a single unit cell. Nonetheless, considering a dielectric polarizability for LAO of $\varepsilon_r = 24$, the effective electrostatic potential energy is reduced to $0.20eV/\mathring{A}$ and it will equal the band gap only when the number of

LAO layers is about 5 unit cells [65]. This electrostatic divergence is commonly known as the polar catastrophe, and it requires some kind of charges redistribution, over a critical LAO thickness, to be eliminated. The conducting properties of the n-type interface are consistent with the polar catastrophe picture: if the LAO coating is less than four unit cells thick, the otherwise metallic junction is a strong insulator and below a separation distance of six unit cells, the sample resistivity is found to increase with decreasing LAO thickness[81]. The coating thickness dependence of the interfacial reconstution can be seen as the consequence of the increase of the electrostatic potential, which is proportional to the LAO thickness.

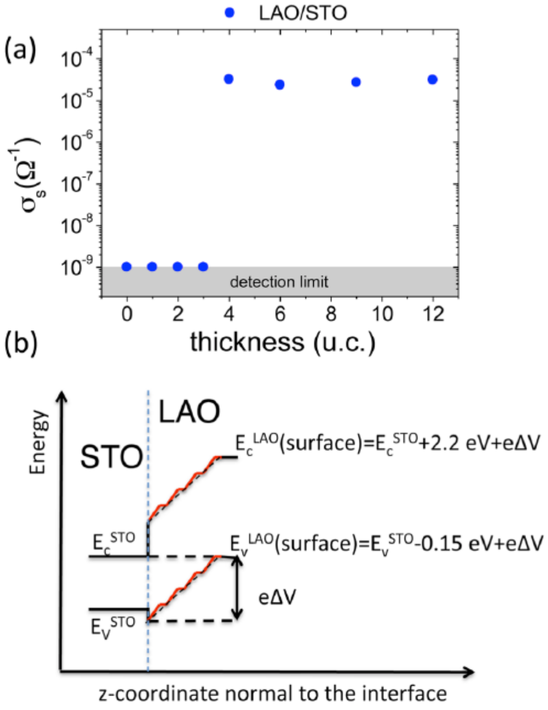

Figure 1.4: Sheet conductance of LAO/STO heterostructures as function of the LAO thickness. (b) A schematic band diagram of the LAO/STO interface just before the electronic reconstruction.

The electronic reconstruction mechanism In TMO charge rearrangement can occur thanks to the possibility of a mixed valence charge state on the individual ions, in contrast to semiconductors where the ions have a fixed valence. In fact one of the most popular mechanisms to understand the charge reconstruction at the LAO/STO interface relies on the net transfer of half of the unit charge per two-dimensional unit cell from LAO to the first layer of STO, maintaining the overall charge neutrality. For n-type junction the transfer involves negative charge: Titanium in STO is in a $3d^0$ configuration and has a Ti^{+4} valence, thus the charge transferred from the AlO_2 layer will change the valence of 50% of the titanium ions at the interface to Ti^{+3}. The resulting configuration for the last layer of STO is $Ti^{+3.5}$, leading to a metallic interface. In this *electronic reconstruction* the uppermost AlO_2 plane of LAO would be missing half an electron. In the p-type junction the last STO layer must acquire an extra half-hole and, due to the fact that, for Titanium, the $Ti^{+4.5}$ mixed valence is energetically inacessible, an *atomic reconstruction* is required, in the form of oxygen vacancies in the SrO plane, leaving the interface insulating. In both cases the reconstruction generates an interface dipole that causes the electric field to oscillate around zero, keeping the potential finite and avoiding the polar catastrophe. This mechanism is sketched in Fig.[1.3]. Spectroscopic studies corroborate this picture finding, for n-type interfaces, $(0.7 \pm 0.1)\, e^-/u.c.$ per unit cell on the Ti atoms, and a relevant fraction of oxygen vacancies $(0.32 \pm 0.06)\, e^+/u.c.$ in the p-type interface and no free holes[56]. It worth mentioning that in this kind of reconstruction oxygen vancancies act as hole donors in contrast with their standard role in bulk oxides as electron donors, and they are far more robust against annealing.

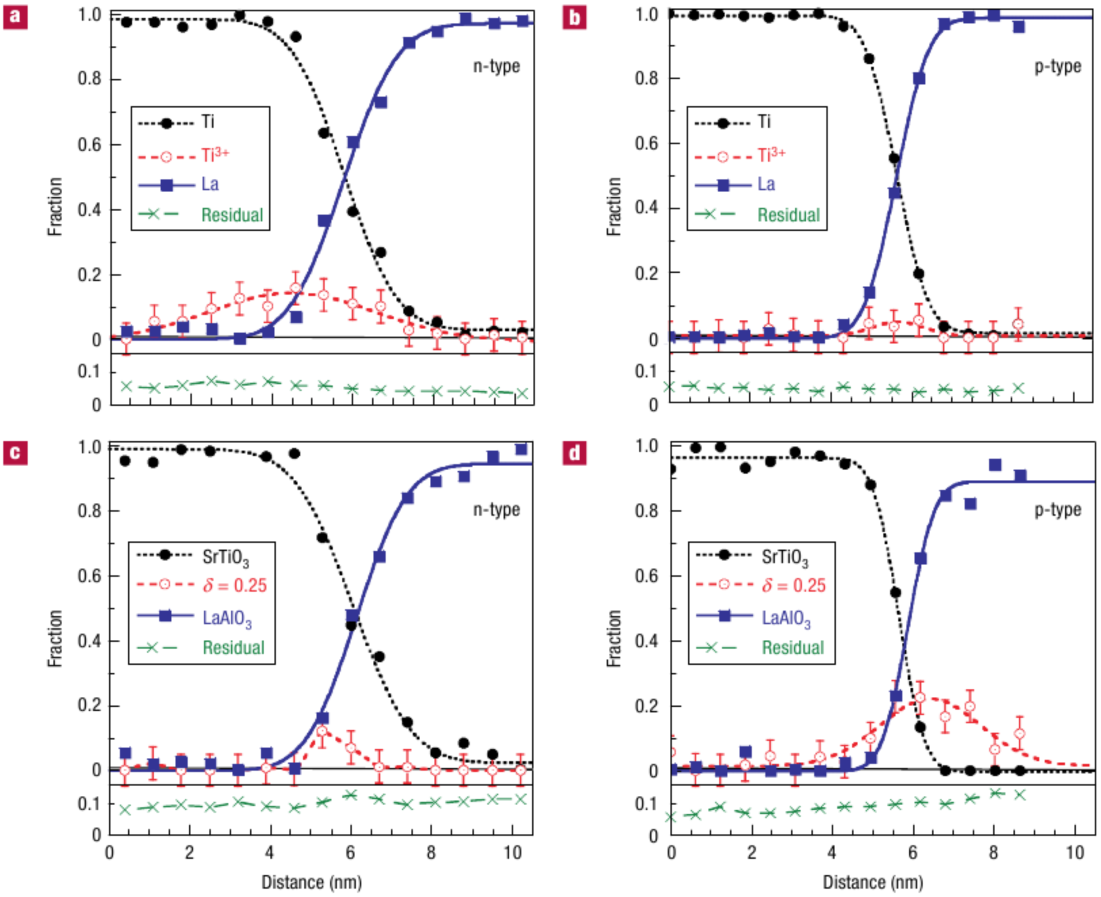

Figure 1.5: In each panel, the $SrTiO_3$ substrate is on the left and the $LaAlO_3$ on the right.
(a) n-type interface showing the fractions of elemental Ti and La and the Ti^{+3} fraction. There is excess Ti^{+3} on the substrate side of the interface. (b) Corresponding Ti and La EELS profiles for the p-type interface, showing almost no excess Ti^{+3}. (c) Fractional compositions the n-type interface, showing a net vacancy excess of $\delta = 0.1 \pm 0.04$. (d) Fractional composition for the p-type interface showing a significant accumulation of excess vacancies $\delta = 0.32 \pm 0.06$.

As it can be seen from Fig.[1.5], at the n-type interface the electrons are not confined in a single layer but they spread into a screening cloud delocalized along a few unit cells, in a width of about $10nm$, containing slightly more electrons than expected, which in turn are compensated for by a smaller number of oxygen vacancies. This increase in the dipole moment at the interface can be explained in terms of interface defects due to the exchange of Sr cation with La on the STO side. A more recent [47salluzz] approach to the electronic reconstruction of n-type interfaces relies on a ionic picture, in which an initially neutral LaO layer acts as a half-electron donor for the neighboring AlO_2 layers. The resulting charge stacking along the growth direction is the same described above, with the advantage of not requiring the tunneling of the half-electron from the far topmost layer to the interface and naturally explaining the appearance of the compensating charges on both sides of the LAO film.

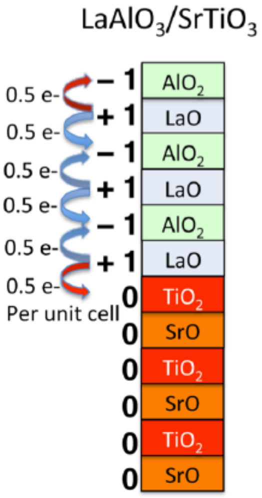

Figure 1.6: Stacking of $LaO^{(+1)}$ and $AlO_2^{(-1)}$ planes along the [001] direction of LAO/STO interface. Starting from neutral planes, at the equilibrium the LaO layers donate electrons which becomes bound in the neighbouring AlO_2 planes. In particular 0.5 electrons are donated to two neighbour AlO_2 planes in the bulk of LAO (on the upper and lower unit cells), and 0.5 electrons are donated naturally to the charge neutral TiO_2 plane (a positive uncompensated charge of -0.5 e should remain on the surface)

Open questions Although this model captures many features of the observed phenomena, few open questions still remain. One among the others is the difference between the experimentally measured electronic carrier density ($2-4\times 10^{13}cm^{-2}$) in n-type interface [81, 76] and the one predicted by the polar catastrophe model ($3\times 10^{14}cm^{-2}$). A possible explanation is that part of the electrons injected from LAO become localized and do not contribute to the conduction. The electronic localization at the interface has been extensively studied in the context of strong-correlation effects, lattice deformations, polarons, etc. (see, e.g., Refs.[88, 93, 64, 63, 70]). One of the latest proposal to explain the carrier density relies on a phase-separation at the interface, with non-percolating conducting regions surrounded by insulating ones. Increasing the LAO thickness, more electrons are injected and give rise to conduction. The onset of conduction may arise because electrons start to occupy higher-energy interfacial orbitals, e.g., different $Ti\ 3d-t_{2g}$ sub-bands[66, 22, 72] . Indeed the two-dimensional spatial confinement has the consequence of lifting the t_{2g} orbital degeneracy and to produce a sub-band structure[73] where heavier d_{xz} and d_{yz} orbitals are pushed to higher energies.

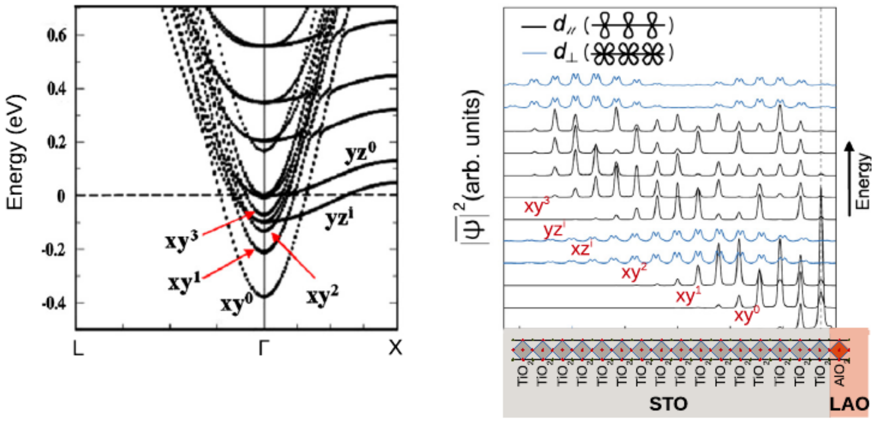

Figure 1.7: (Left) Electronic sub-band structure in the Brillouin zone calculated for the LAO/STO interface[37]. (Right) Spatial dependence of the square of the associated sub-band eigenfunctions in the direction perpendicular to the interface; $d_{||}$ refers to d_{xy} orbitals while $d_\perp$ refers to d_{xz} and d_{yz} orbitals [38]. The orbital character of the states is shown in both panels; for each orbital a superscript labels the energy of the band at the Gamma point. One notices that, for the first three dxy sub-bands, it also identifies the location of the TiO_2 layer counted from the interface where the probability of presence of the carriers in that band is dominant.

As can be seen from fig.[1.7] showing the modulus square of the eigenfunctions of the low energy sub-bands, the conduction bands come from d orbitals with a strong d_{xy} character in the first three TiO_2 layers next to the interface. For the narrow bands arising from the confined d shell, the ratio between the Coulomb repulsion energy and the bandwidth is no more a negligible quantity, hence theoretical approaches relying on a independent particles picture are not appropriate. The framework of this kind of physic is the that of strongly correlated electron systems in which $e - e$ correlation must be taken into account in a many-body scheme despite the original building blocks are band insulators.

1.2.3 Two-dimensional electron gas at the LTO/STO interface

Another spectacular example of an emergent metallic state at the interface between naturally insulating TMO compounds has been extensively studied at the junction between STO and $LaTiO_3$ (LTO), where the latter is a Mott insulator. In [60] it has been reported the synthesis of a $(SrTiO_3)_n/(LaTiO_3)_m$ multilayered structure showing a well defined one dimensional charge modulation due to an extra electron per Ti sites resulting in a metallic state at the interface. As we discussed above, the formal valence of the STO Titanium atom is Ti^{+4} giving rise to a band insulator, while in LTO the formal valence is Ti^{+3} resulting in a single electron in a narrow d shell. At integer fillings the short-range Hubbard repulsion can localize the carriers leading to a Mott insulator. It has been argued that minor deviation from this picture might occur considering that the LTO crystal has not perfect a perfect orthorhombic symmetry but presents an tetragonal distortion [39] due to the small lattice constant mismatch ($a_{STO} = 3.91\AA$ and $a_{LTO} = 3.97\AA$). This eventually results into non diagonal components in the t_{2g} density of states at the inteface, which implies that a slightly different basis diagonalizes the system with a slightly larger density of states possibly leading to a strongly correlated metal rather than a Mott insulator. Therefore the ideal charge depletion we are referring to occurs at the interface between a band insulator and a strongly renormalized metal with non integer $3d$ occupancy. Any other perturbation of the electronic d state is negligible at the Fermi level despite the chemical abruptness of the interface. As in the previous case also in this junction a threshold thickness of LTO is required to retrieve bulk-like electronic properties.

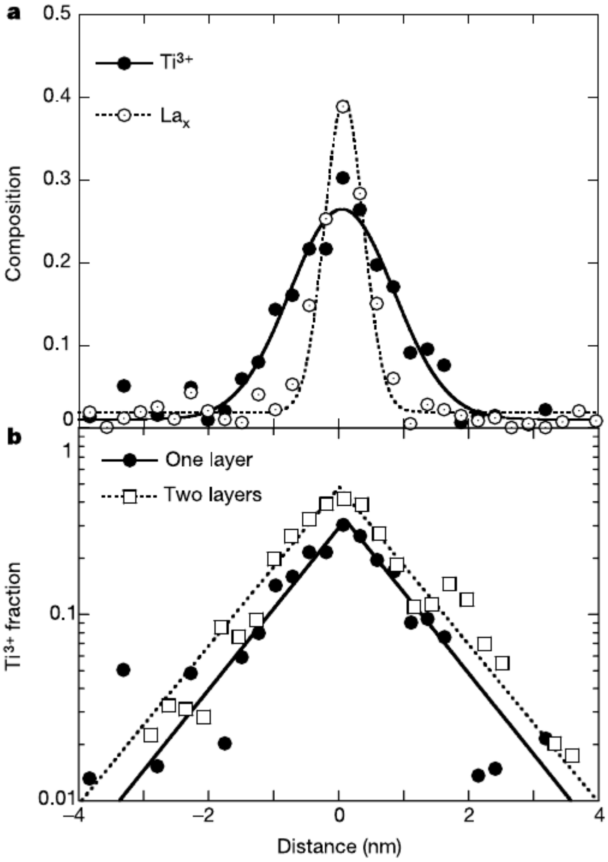

Figure 1.8: (a) Spatial distribution contributions of Ti and La atoms comnig forom EELS spectroscopy; (b) decay of the Ti^{+3} signal away from the single and double LTO layer.

In Fig.[1.2.3] we show how the Ti^{+3} signal can be fitted through an exponential decay with a characteristic length of $l = 1.0 \pm 0.2nm$. A rough estimate for this value has been given in the context of an effective mass description which confirms that this system can be understood only in terms of a strongly correlated metal. Indeed considering a dielectric constant-effective mass ratio of $\varepsilon/m^* \sim 10 \div 100$ the resulting Thomas-Fermi screening length would be $l = 0.23 \div 0.72$ in rather good agreement with the above estimate. Finally in

Fig.[1.2.3] we report the summary of the electronic properties of the LTO/STO interface where the overall conductivity has been found to be roughly $^2/_3$ the La fraction present in the superlattice. Since the interface charge modulation results from the equilibrium distribution of LaO donor layers, an appropriate theoretical description of this interface would be the one provided by the Hubbard model with the inclusion of long range mean-field interactions.

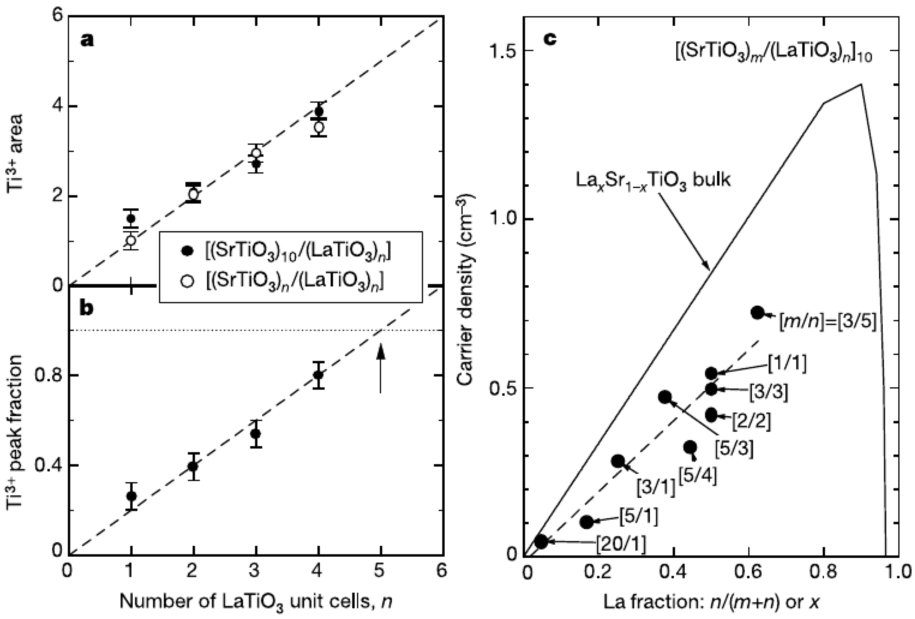

Figure 1.9: (a) Ti^{+3} area across the LTO unit cell as a function of the LTO thickness; (b) Ti^{+3} fraction as a function of the LTO thickness; (c) measured carrier density for different superlattice composition compared with the bulk results for Sr doped LTO, the slope of the dashed line is $^2/_3$.

1.2.4 Superconductivity at oxide interfaces

In both LAO/STO and LTO/STO heterojunctions a superconducting phase appears below the common critical temperature of $T_c \sim 300mK$. This is a most remarkable result in many respects, but perhaps the most distinctive aspect lies in the two dimensional nature of the superconducting condensate, testified by critical field measurements which reveal a strong differentiation between the parallel and perpendicular H_c components. Considering H_c one can extrapolate the Landau-Ginzburg coherence length of the superconducting sheet:

$$\xi\left(T\right)=\sqrt{\frac{\phi_o}{2\pi\mu_o H_c^{\perp}\left(T\right)}} \tag{1.1}$$

which gives $\xi^{LAO}=60nm$ and $\xi^{LTO}=42nm$, while the thickness of the condensate is given by:

$$d=\frac{\sqrt{3}\phi_o}{\pi\xi\left(T\right)H_c^{\parallel}\left(T\right)} \tag{1.2}$$

resulting in $d^{LAO}=10nm$ and $d^{LTO}=12nm$. These values demonstrate the close similarity between the superconducting phases in the two junctions, regardless the different nature of one of the two constituents. Another independent confirmation of the two-dimensional nature of the system comes from conductivity that, in this geometry, has a peculiar logarithmic dependence on the temperature:

$$\sigma\left(\omega\right)=\sigma_o+\frac{pe^2}{\pi h}\ln\frac{T}{T_c} \tag{1.3}$$

where p depends on the most relevant scattering process which is responsible for the loss of phase coherence and to the resistive behavior. In LTO/STO such logarithmic dependence has been clearly observed with an estimated value of p very close to the one characteristc of $e-e$ interactions. Both the phase diagrams, reported in Fig.[1.10], have a dome-shaped aspect with an "underdoped" and an "overdoped" regime where a continuous tuning of the superconducting transition has proven feasible with the direct observation of a superconductor to insulator transition via a gate voltage [9].

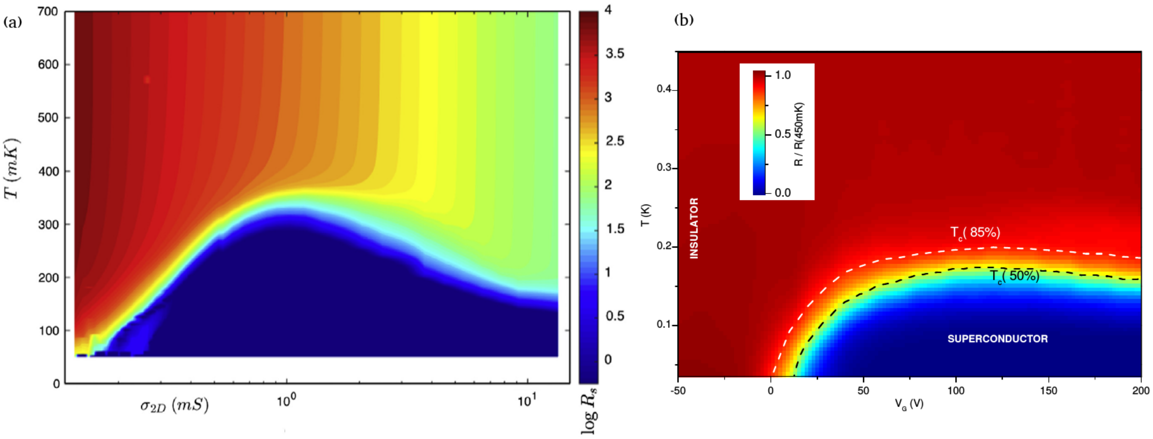

Figure 1.10: (a) SC phase diagram for the LAO/STO (a) and LT)/STO (b)junctions.

We have already described that the electronic reconstruction is responsible for the 2DEG at the LAO/STO junction and how this conducting sheet is located in the STO surface. Also this feature is shared by the LTO/STO interface, where the 2DEG is confined within few unit cells on the STO side [10]. Thus the main difference between the two system is in the electronic structure band differentiation due to the inversion symmetry breaking, that takes place in the LAO junction. The effect that this band splitting have on superconductivity can be deduced from the doping dependence of T_c: in bulk STO the superconducting phase develops at very low density and it is stable over a wide doping range. On the other hand the interfacial superconductivity in LAO/STO develops only over a density threshold of $5 \cdot 10^{18}\text{cm}^{-1}$. This can be roughly understood considering that "heavy" electron bands imply a large effective density of states for the quasiparticles which, in a simple picture, can favor superconductivity by enhancing the effective coupling. The fact that, in bulk STO, the lowest band is "heavy" would explain the wide doping range in which superconductivity has been found. On the other hand in LATO/STO the lowest band has a d_{yx} character with a much smaller effective mass and it lies approximately $300meV$ below the Fermi level. This would explain why superconductivity sets in only at a given doping, which corresponds to the filling of the heavier d_{xz} and d_{xz} subbands. The reduction of SC in the overdoped region is believed to be caused by the filling of bands different from those where superconductivity is expected to establish, which causes an higher cross section for $e-e$ scattering processes [10].

The pairing mechanism that binds the electron in Cooper pairs, and eventually leads to their condensation in an actual superfluid phase at low temperature, has recently been addressed[15, 13], obtaining enlightening results in the framework of the electron-phonon ($e-ph$) coupling. When carriers and the hosting lattice site are strongly coupled, a moving electron, or hole, can displace ions from their equilibrium position. The two kind of excitation, electronic and phononic, cannot be considered disentangled and form a quasiparticle called polaron. A polaron is a fermionic carrier surrounded by the lattice distortion caused by its own presence, which in turn reduces its mobility as measured by a phonon-driven enhancement of the effective mass. We will discuss these features at length in the original chapters of this thesis. A fingerprint of a polaronic excitation is a hump in the spectral weight at the binding energy of the phonon ω_o.

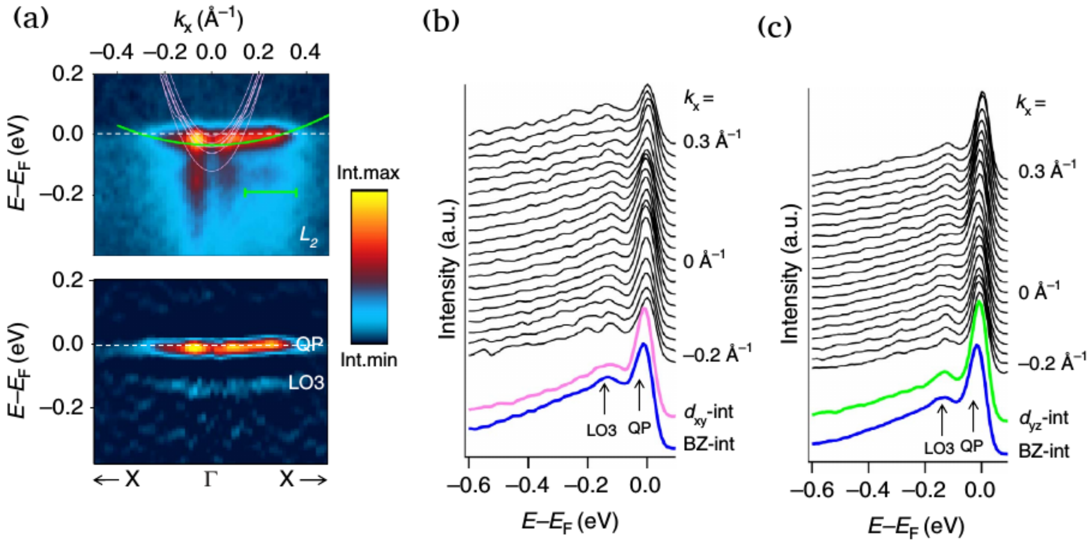

Figure 1.11: (a)High-resolution ARPES images along the $k_y = 0$ line with the superimposed theoretical d_{xy} (pink) and d_{yz} (green) bands. The lower panels show the corresponding second derivative plots, which clearly show both the quasiparticle peak and the dispersive hump formed by the LO3 phonon. (b,c) The characteristic energy distribution curves manifests a polaronic metal state formed by the LO3 phonon identified by the the clear hump dispersion.

In Fig.[1.11] we report ARPES measurements on the buried STO doped region, in the LAO/STO junction along the $k_y = 0$ direction, with superimposed the theoretical dispersion of d_{xy} and d_{yz} sub-bands. We first notice the agreement between theory and experiment as far as the band differentiation is concerned. Moreover the experiment detect clear signs of interaction by means of a reduced effective mass $m^* = 2.5m$ with respect of those computed numerically. The energy distribution curves reported in Fig.[1.11], which correspond to ARPES intensities as a function of the photon energy for different **k** points, present a hump at about $118meV$ which is a the signature of a bosonic mode excitation and, since, the hump structure is the same for d_{xy} and d_{yz}, then the additional coupling does not depend on the orbital spatial distribution. It has been shown[15] that this peak in the **k**-resolved spectral function can be attributed to phononic modes suggesting that the conducting 2DEG at the LAO/STO interface is a polaronic metallic state with a carrier density of roughly $n = 0.12$electrons per unit cell.

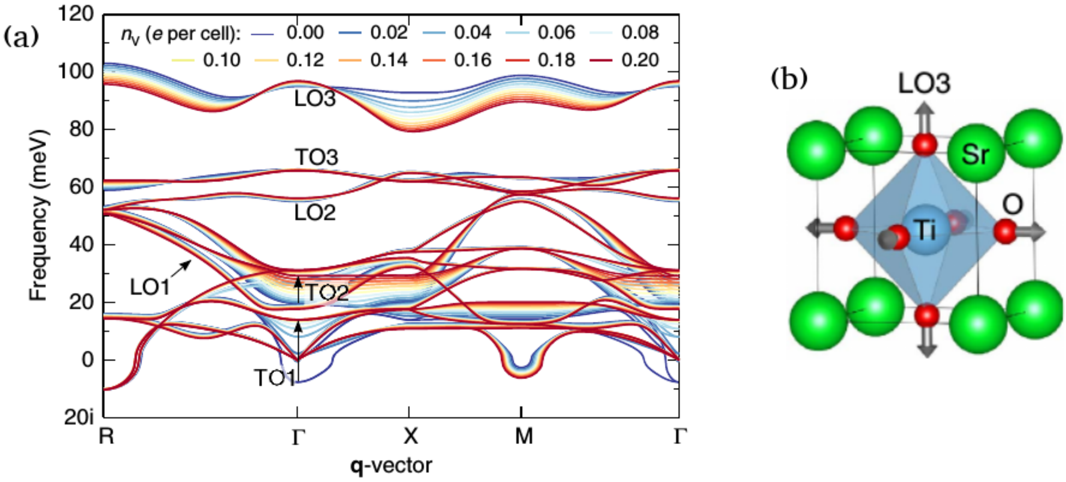

Figure 1.12: Phonon dispersion at various electron doping levels with arrows indicating the mode shifting as a function of the density; (b) Atomic displacements associated with the LO3 mode at the R-point.

In order to address the nature and symmetry of this phononic excitation the authors of Ref.[15] computed the phonon mode dispersion in a cubic lattice of doped STO that we reproduce in Fig.[1.12] identifying the optical longitudinal LO3 phonon mode as the only one at the energy of the hump $\omega_o \sim 118meV$. This lattice excitation correspond to the "breathing distortion" of the octahedral cage around the Ti ion which is charachteristic of a short-range and screening insensitive $e-ph$ coupling well reproduced by an Holstein coupling with a Einstein model from the theoretical point of view. Estimates [13] on the $e-ph$ coupling interaction have found the rather high value of $\lambda \sim 1$ which explains the strong renormalized quasiparticle feature and the fact that, according to BCS theory, phonon coupling must be unusually strong to explain superconductivity with such a low carrier density. On the other hand BCS estimate based on the value $\lambda \sim 1$ would predict a critical temperature of $T_c > 60K$ while, two order of magnitude above the measured value. On the other hand, a weak-coupling BCS superconductivity has been proposed owing to the value of the ratio $\frac{2\Delta_o}{K_B T_c} = 3.56 \pm 0.03$ where Δ_o is the extrapolated zero temperature gap. Thus, another valid path is to estimate λ from the spectroscopic superconducting gap, from which a value of $\lambda_{BCS} \sim 0.1$ has been extracted together with the conclusion that Coulomb repulsion interaction must be responsible for the reduced effective attractive interaction.

The quest for a unifying solution that connects low density, strong Coulomb repulsion, high $e-ph$ interaction in a two-dimensional geometry and s-wave superconductivity has enthralled theoretician for quite a long time nowadays and this is precisely the framework where an important part of the work reported in the present Thesis must be placed.

CHAPTER

2

MODELING CORRELATED ELECTRONS AT INTERFACES

In the previous chapter we gave a brief overview of the complex properties of heterostructures of transition-metal oxides. Even if we limited to the most basic aspects of their phenomenology, our summary has emphasized that a proper theoretical modeling of these compounds should include electron-electron and electron-phonon interactions, as well as the spin-orbit coupling. The multi-orbital nature of the relevant d bands also requires a multi-band description including the Hund's coupling. Last, but not least, a theoretical approach should be able to account for the inhomogeneous electronic properties at the interface, which can change the hierarchy between the several energy scales associated to the variety of interactions we mentioned before. In this chapter we introduce the basic ideas behind the theoretical description of the main interaction effects taking place in TMO heterostuctures. We start from the basic concepts of electron-electron correlations (Sec. 2.1) and their extension to multi-orbital systems (Sec. 2.1.1). We take a little detour to discuss the attractive Hubbard model, which is introduced as the simplest model to study superconductivity beyond the BCS limit (Sec. 2.1.2). Sec. 2.2 is devoted to the electron-phonon interaction in the simplest Holstein moel and its interplay with strong correlation physics in the Hubbard-Holstein model. Finally in Sec. 2.3 we discuss the local spin-orbit coupling in multi-orbital systems. We postpone to Chapter 3 the discussion of the methodology we employ in this thesis to study the above interactions, the Dynamical Mean-Field Theory and, in Chapter 4, its extension to inhomogeneous layered systems, which is one of the novel results of this work.

2.1 The Hubbard Model and electron-electron interactions

Within the Born-Oppenheimer the Hamiltonian which describes N_e electrons interacting with N_I ions forming a regular lattice is:

$$\mathcal{H} = \sum_i^{N_e} \left[\underbrace{-\frac{\hbar}{2m_e}\nabla_i^2}_{T} - \underbrace{\frac{e^2}{4\pi\epsilon}\sum_j^{N_I} \frac{Z_i}{|\mathbf{r}_i - \mathbf{R}_j|}}_{V} \right] + \underbrace{\frac{1}{2}\frac{e^2}{4\pi\epsilon}\sum_{j\neq i}^{N_e} \frac{1}{|\mathbf{r}_i - \mathbf{r}_j|}}_{U} \tag{2.1}$$

where $\mathbf{r}$ and $\mathbf{R}$ are the positions of the electrons and ions respectively. Eq.[2.1] is composed by a single-electron contribution $T + V$, consisting of a kinetic and static potential terms, and a electron-electron (e-e) interaction term U. The latter prevents to write the whole hamiltonian as a sum of single-particle disentangled hamiltonians, which is the main reason why this *many-body* problem defies any simple solution. As we will discuss in the following, the difficulty lies also in the different nature of the two terms of Hamiltonian of Eq.[2.1]. While the single-particle contribution can be diagonalized in the momentum representation $\{|\mathbf{k}\rangle\}$ giving rise to a set of bands, the U term is diagonal in the configuration representation $\{|\mathbf{r}_i\rangle\}$, which makes the simultaneous diagonalization very hard. From this dichotomy follow two different approaches to attack this problem according to the effective strength of the two terms. For weakly interacting systems, as it happens when the valence electrons populate s or d shells, the effect of the interaction can be recast into an effective single-particle description, as in Hartree-Fock approximation or in Kohn-Sham density functional theory (DFT).

On the other hand, for systems with valence electrons in open d or f shells, the e-e correlations due to the Coulomb repulsion are not negligible and the single particle picture fails. The most spectacular effect of the electron correlation is to challenge one of the most basic results of the band-theory of solids. According to this theory, which relies on a single-particle picture, a solid is an insulator if the electrons completely populate one band leaving the following band empty, while any other filling of the bands corresponds to a metallic state. In strongly correlated systems instead the Coulomb repulsion between electrons can results in a insulating phase even though the bands are partially filled as long as the number of electrons per ion is integer. These systems are called Mott insulators since N. Mott has been the first to propose this correlation-driven breakdown of the band-theory of solids. Rephrasing the Hamiltonian of Eq.[2.1] in second quantization, on a basis of localized Wannier functions associated to the ionic positions produces the following lattice model:

$$\mathcal{H} = -\sum_{\alpha\beta}\sum_{\sigma\bar{\sigma}}\sum_{ij}\hat{t}\left(\hat{c}^{\dagger}_{i\alpha\sigma}\hat{c}^{\dagger}_{j\beta\bar{\sigma}} + h.c.\right) + \frac{1}{2}\sum_{\alpha\beta\gamma\delta}\sum_{\sigma\bar{\sigma}}\sum_{ijlm}\hat{U}\hat{c}^{\dagger}_{i\alpha\sigma}\hat{c}^{\dagger}_{j\beta\bar{\sigma}}\hat{c}_{k\gamma\bar{\sigma}}\hat{c}_{l\delta\sigma} \tag{2.2}$$

Here $\hat{c}_{i\alpha\sigma}$ $\left(\hat{c}^{\dagger}_{i\alpha\sigma}\right)$ is the destruction (creation) operator of a fermion with spin σ of the α band of the i-th lattice site. The hopping matrix $\hat{t} = t^{\alpha\beta\sigma\bar{\sigma}}_{ij}$ is the parametrization of the non-interacting dispersion of the $T + V$ operator:

$$t^{\alpha\beta\sigma\bar{\sigma}}_{ij} = \int d\mathbf{r}\psi^{\dagger}_{i\alpha\sigma}\left(\mathbf{r}\right)\left[\frac{\hbar}{2m_e}\nabla^2 - V\left(\mathbf{r}\right)\right]\psi_{j\beta\bar{\sigma}}\left(\mathbf{r}\right) \tag{2.3}$$

and $\hat{U} = U^{\alpha\beta\gamma\delta}_{\sigma\bar{\sigma},ijkl}$ encloses all the correlations:

$$U^{\alpha\beta\gamma\delta}_{\sigma\bar{\sigma},ijkl} = \int d\mathbf{r}d\mathbf{r}'\psi^{\dagger}_{i\alpha\sigma}\left(\mathbf{r}\right)\psi^{\dagger}_{j\beta\bar{\sigma}}\left(\mathbf{r}\right)U\left(\mathbf{r}-\mathbf{r}'\right)\psi_{k\gamma\bar{\sigma}}\left(\mathbf{r}'\right)\psi_{l\delta\sigma}\left(\mathbf{r}'\right) \tag{2.4}$$

The energy associated to the scattering process of two particles in the quantum states $|i\alpha\sigma, j\beta\bar{\sigma}\rangle$, scattering into the states$|k\gamma\bar{\sigma}, l\delta\sigma\rangle$, is given by $U^{\alpha\beta\gamma\delta}_{\sigma\bar{\sigma},ijkl}$. It is easy to realize that the therm with $i = j = k = l$ (on-site interaction) is the largest term. This obviously descends from the fact that the Coulomb interaction decays with the distance, but in many materials it is reasonable to neglect all the non-local terms because of the screening of the Coulomb interaction between valence electrons given by the core levels, which can make the interaction short ranged. In order to illustrate the basic interplay between the two terms, it can be useful to simplify the general hamiltonian of Eq.[2.2] by restricting to the case of a singular orbital band. This leads to the popular single-band Hubbard model, arguably one of the basic and most studied models in condensed matter:

$$\mathcal{H} = -t \sum_{\sigma} \sum_{ij} \left(\hat{c}^{\dagger}_{i\sigma} \hat{c}^{\dagger}_{j\sigma} + h.c. \right) - \mu \sum_{i} \left(\hat{n}_{i\uparrow} + \hat{n}_{i\downarrow} \right) + U \sum_{i} \hat{n}_{i\uparrow} \hat{n}_{i\downarrow}. \tag{2.5}$$

Already the simples single-band formulation of the problems features the archetypal competition between the delocalizing effect of the kinetic energy and the localizing tendency driven by the electron-electron interaction. As we shall see in the next chapter, when the number of electrons equals the number of sites (half-filling), this simple model presents a metal-insulator transition (Mott-Hubbard transition) increasing the strength of the interaction U and changing the ratio with respect to the bare half-bandwidth $D \sim d \cdot 2t$. For small U/D the system is in fact in a metallic Fermi-liquid state, where the effects of interactions are largely included in the effective mass renormalization, while for very large U/D the electrons are localized, one per lattice site, in order to minimize the repulsive potential energy.

In this phase, the charge degrees of freedom are frozen out since double occupations become energetically very unfavorable resulting in a strong suppression of the hopping. Thus, in the $U/W \to \infty$ limit and for $n = 1$, only the spin degrees of freedom persist and the Hubbard model simplifies to the quantum Heisenberg model. If we move away from half-filling, double occupancy is still forbidden, but the presence of empty sites allows the charge tunneling resulting in the so-called $t - J$ model. An insulator-to-metal transition can occur also by changing the density away from half-filling when the interaction is kept constant at $U > U_c$. This is the so-called filling-driven transition, which –for a two-dimensional lattice– is believed to entail the main physics of the high-temperature superconductors.

Indeed this simple model, or its extensions to multi-band configurations, is able to describe many of the effects which are experimentally observed in strongly correlated materials, like, e.g., the transition-metal oxides we briefly discussed in Chapter 1.

2.1.1 Multi-band Hubbard Model and Hund's coupling

The single-band Hubbard Model can be very helpful to understand and visualize the physics of strongly correlated materials, but it is a reasonable miscroscopic model for a rather small set of real materials, with the notable example of the cuprates, which have a single active electronic band at the Fermi-level. The majority of the known transition metals oxides, as well as iron-based superconductors, are instead multi-band materials, with several bands crossing the Fermi level.

The presence of several bands does not merely make the problem more complicated, but it gives rise to interesting novel phenomena which have attracted a lot of interest in the last few years. Indeed many compounds with multiorbital configurations d^2, d^4 and d^6 display clear signatures of strong correlations despite being far from a Mott transition because of a moderate value of the U/D ratio. The key player in these anomalies has been identified in the Hund's coupling. This effect is peculiar of multi-orbital correlated systems and it correspond to the energy scale associated with intra-atomic exchange, which lowers the cost in repulsive Coulomb energy when placing two electrons in different orbitals with parallel spin, as opposed to two electrons in the same orbital. Different studies, in the context of iron pnictides and multi-orbital Kanamori model[25, 90], revealed that the low-energy quasiparticle coherence scale is considerably reduced by Hund's coupling. For systems with integer filling different from global half-filling, however, the Hund's coupling shifts the Mott transition to larger values of the interaction, therefore creating a large region of interactions where the system is in a strongly correlated metallic state but it is not close to full Mott localization. There two-fold effect of the exchange interaction has been called a Janus effect to underline the dual nature[25]. For half-filled band, instead, the Mott transition is pushed to smaller values of the interactions, coherently with the decrease of the coherence scale.

The intermediate region with strong correlations but far from the Mott transition has been shown to display remarkable properties including a finite-temperature incoherent non-Fermi liquid metallic state with frozen local moments, anomalies in the magnetic response function [33], and a marked orbital-selective behavior in which different orbitals have a completely different degree of correlation[24, 23]. Quantitatively, one can derive additional intra-orbital local interactions for multi-orbital systems directly from Eq.2.4:

$$\begin{aligned}
U &= \int d\mathbf{r}d\mathbf{r}' \left|\psi_{\alpha\uparrow}\left(\mathbf{r}\right)\right|^2 U\left(\mathbf{r}-\mathbf{r}'\right) \left|\psi_{\alpha\downarrow}\left(\mathbf{r}'\right)\right|^2 \\
U' &= \int d\mathbf{r}d\mathbf{r}' \left|\psi_{\alpha\uparrow}\left(\mathbf{r}\right)\right|^2 U\left(\mathbf{r}-\mathbf{r}'\right) \left|\psi_{\beta\downarrow}\left(\mathbf{r}'\right)\right|^2 \\
J &= \int d\mathbf{r}d\mathbf{r}' \int d\mathbf{r}d\mathbf{r}' \psi^{\dagger}_{\alpha\sigma}\left(\mathbf{r}\right) \psi^{\dagger}_{\beta\bar{\sigma}}\left(\mathbf{r}\right) U\left(\mathbf{r}-\mathbf{r}'\right) \psi_{\beta\bar{\sigma}}\left(\mathbf{r}'\right) \psi_{\alpha\sigma}\left(\mathbf{r}'\right)
\end{aligned}$$

The full many-body multi-orbital Kanamori interaction term of the Hamiltonian is:

$$\begin{aligned}\mathcal{H} &= U\sum_{\alpha}\hat{n}_{\alpha\uparrow}\hat{n}_{\alpha\downarrow}+U'\sum_{\alpha\neq\beta}\hat{n}_{\alpha\uparrow}\hat{n}_{\beta\downarrow}+(U'-J)\sum_{\alpha\neq\beta,\sigma}\hat{n}_{\alpha\sigma}\hat{n}_{\beta\sigma} \\ &\quad +J_X\sum_{\alpha\neq\beta}\hat{c}^{\dagger}_{\alpha\uparrow}\hat{c}_{\alpha\downarrow}\hat{c}^{\dagger}_{\beta\downarrow}\hat{c}_{\beta\uparrow}+J_P\sum_{\alpha\neq\beta}\hat{c}^{\dagger}_{\alpha\uparrow}\hat{c}^{\dagger}_{\alpha\downarrow}\hat{c}_{\beta\downarrow}\hat{c}_{\beta\uparrow}\end{aligned} \tag{2.6}$$

composed by the density-density interaction, involving the $\hat{n}$ operators, and the J_X spin-flip and J_P pair hopping interactions. As described in [32], rewriting Eq.[2.6] by means of the total density, spin and angular momemtum operators:

$$\hat{N}=\sum_{\alpha\sigma}\hat{n}_{\alpha\sigma} \qquad \hat{S}=\sum_{\alpha}\sum_{\sigma\bar{\sigma}}\hat{c}^{\dagger}_{\alpha\sigma}\hat{\sigma}\hat{c}_{\alpha\bar{\sigma}} \qquad \hat{L}=i\sum_{\alpha\beta\gamma}\sum_{\sigma}\epsilon_{\alpha\beta\gamma}\hat{c}^{\dagger}_{\alpha\sigma}\hat{c}_{\beta\sigma} \tag{2.7}$$

the simultaneus charge, spin and orbital $U_C(1)\otimes SU_S(2)\otimes SO_O(3)$ invariance is mantained provided:

$$J_X=J \qquad J_P=J \qquad U'=U-2J \tag{2.8}$$

With these restriction Eq. 2.6 can be written as:

$$\mathcal{H}=(U-3J)\frac{\hat{N}\left(\hat{N}-1\right)}{2}-2J\hat{S}^2-\frac{J}{2}\hat{L}^2+\frac{5}{2}J\hat{N} \tag{2.9}$$

The three Hund's phenomenological rules for the (orbitally degenerate) ground-state are now justified:

- the total spin S should first be maximized;
- given S, total angular momentum L should be maximized;

It has been clarified by many authors how, the Hund's coupling has a strong influence on the critical interaction stregth U_c.

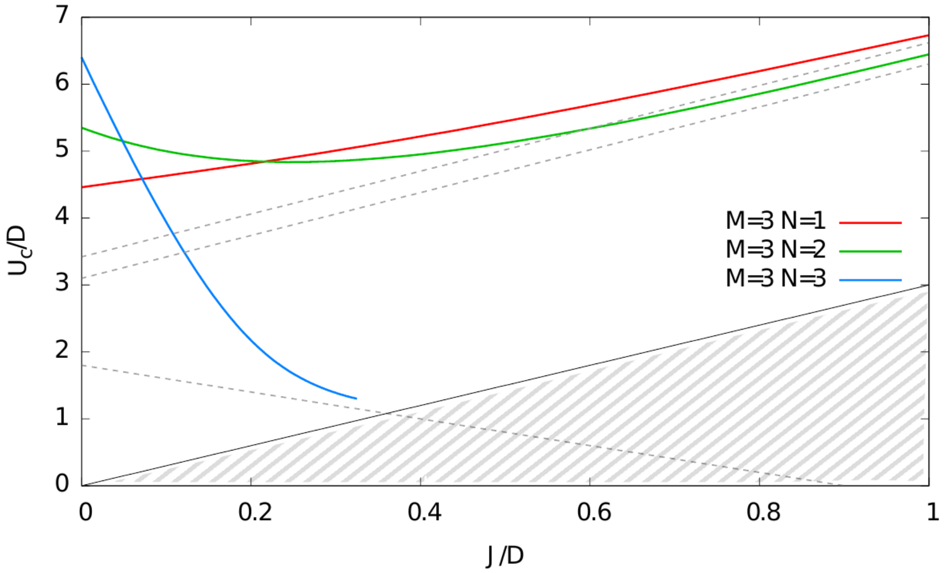

Figure 2.1: Critical coupling separating the metallic and Mott insulating (paramagnetic) phase, as a function of Hund's coupling, for a Hubbard-Kanamori model of three degenerate bands with one (red), two (green) and three (blue) electrons per site. The model is solved with DMFT, with a semi-circular density of states of bandwidth $2D$ for each band. Dashed lines indicate the atomic-like estimates. The shaded region corresponds to $U - J < 0\,(J > U/3)$.

Fig. 2.1 shows the dependence of U_c on J for a Hubbard-Kanamori model of three $(M = 3)$ degenerate orbitals. As we mentioned above, in the $N = 1, M, 2M-1$ cases, at small J, the effect is to strongly reduce U_c then to increase it roughly linearly at larger J, making the Mott phase harder to reach. An exaustive review on this topic is given in Ref.[32].

2.1.2 Attractive Hubbard Model

In this section we take a little detour from our main direction and we consider an attractive Hubbard model as a simple model for superconductivity. We will indeed use this model in Chapter 4 to discuss the effect of an interface on superconductivity beyond the weak-coupling limit. This model is indeed widely used to study the crossover from a weak-coupling superconductivity, which is essentially described within a mean-field approach analogous to the BCS theory, and a strong-coupling superconductivity, in which tightly bound pairs of bosonic nature are formed at high temperature and superconductivity is associated with their condensation (Bose-Einstein condensation, BEC)[44, 84, 85]. This two regimes are continuously connected by the so called BCS-BEC crossover.

The model has exactly the same form of the repulsive model except for the sign of the interaction and it consists of two competing terms, namely, the hopping kinetic energy and a local istantaneous pairing:

$$\mathcal{H} = -t\sum_{\sigma}\sum_{ij}\left(\hat{c}^{\dagger}_{i\sigma}\hat{c}^{\dagger}_{j\sigma} + h.c.\right) - \mu\sum_{i}\left(\hat{n}_{i\uparrow} + \hat{n}_{i\downarrow}\right) - U\sum_{i}\hat{n}_{i\uparrow}\hat{n}_{i\downarrow}, \tag{2.10}$$

where U is a positive quantity in order to describe an attraction between electrons. The on-site density-density interaction term favors double occupancy and, below a critical temperature T_c, the formation of s-symmetric pairs. The electron pairs become local in the strong-coupling limit. The model is suitable to descibe the evolution from conventional BCS superconductivity, at $U/D \ll 1$, to bosonic pair condensation when $U/D \gg 1$, just tuning the ratio U/D. A mean field analysis [69] of the weak-coupling limit shows indeed a BCS-like behavior with a Hartree critical temperature of $k_B T_c \sim \sqrt{n(2-n)}e^{-2W/|U|}$ while, in the opposite limit[68], the bounded electron behave like hard core spin 0 bosons with a mean-field estimate of the critical temperature that goes like: $T_c \sim \frac{1-n}{\ln\frac{2-n}{n}}\frac{2t^2}{U}$ in the high density limt. This BEC phase is peculiar of systems with short-range, unretarded pairing and characterized by an extremely short coherence length, which can be found in materials with strong couplings between electrons and lattice[91] or electron and bosonic excitations such as plasmons[37, 79]. The ground state of the attractive Hubbard model is a singlet s-wave superconductor for any interaction U and filling n, in contrast to the case $U > 0$, where a gap exists only at integer fillings. It can be shown how, through the staggered particle-hole canonical transformation on a bipartite $A - B$ lattice:

$$\hat{c}_{i\downarrow} \rightarrow (-1)^{\text{sign}(i \in A,B)}\,\hat{c}^{\dagger}_{i\downarrow} \tag{2.11}$$

the AIM can be exactly mapped in a repulsive Hubbard model in a magnatic field. In particular, the kinetic term is unaltered, the interaction changes its sign while, as most noticeable modification, the chemical potential of the AIM becomes a magnetization operator:

$$-\mu\sum_i\left(\hat{n}_{i\uparrow} + \hat{n}_{i\downarrow}\right) \rightarrow -\mu\sum_i\left(\hat{n}_{i\uparrow} - \hat{n}_{i\downarrow}\right) \tag{2.12}$$

In the particular case of $n = 1$ the SC groundstate of the attractive Hubbard model is degenerate with a staggered charge density wave (CDW) phase, this can be easily understood by means of the mentioned mapping. The antiferromagnetic order parameter of the repulsive model is given by the magnetization defined on the bipartite lattice:

$$\begin{aligned}
\overrightarrow{m} &= \sum_{\alpha=x,y,z} m^{\alpha} \\
&= \sum_{\alpha=x,y,z} \sum_{i \in A,B} (-1)^{\text{sign}(i)} \left\langle \hat{c}^{\dagger}_{i\sigma} \hat{\sigma}^{\alpha} \hat{c}_{i\bar{\sigma}} \right\rangle
\end{aligned}$$

Applying backwards the transformation of Eq.[2.11] to the three components of $\overrightarrow{m}$ one finds that the z-component correspond to the CDW order parameter, while a linear combination of the two components of the in-plane magnetization gives the complex order parameter of the attractive Hubbard model:

$$\begin{aligned}
m_z &\rightarrow \sum_{i \in A,B} (-1)^{\text{sign}(i)} \left(\langle \hat{n}_{i\uparrow} \rangle + \langle \hat{n}_{i\downarrow} \rangle - 1 \right) \\
m_x + i m_y &\rightarrow \sum_{i \in A,B} \left\langle \hat{c}^{\dagger}_{i\uparrow} \hat{c}^{\dagger}_{i\downarrow} \right\rangle \\
m_x - i m_y &\rightarrow \sum_{i \in A,B} \langle \hat{c}_{i\downarrow} \hat{c}_{i\uparrow} \rangle
\end{aligned}$$

The mapping clearly shows that, whenever the repulsive model has an antiferromagnetic state, the attractive model will describe a s-wave superconductor degenerate with a charge-density waves. Indeed as soon as the attractive model is doped, the degeneracy is lifted and the superconducting state remains the most stable. This is easily understood in the repulsive framework, where the mapping implies a uniform magnetic field along the z direction (which corresponds to the chemical potential that drives the attractive model out of half-filling). Hence the z-component of the staggered magnetization will be disfavored with respect to the planar components. Therefore the mapping implies that the s-wave superconductor is the lowest-energy solution for any density in the attractive model.

2.2 The Holstein Model

In this section we review some important aspects of the electron-phonon coupling and its interplay with the electron-electron interaction which can be important at the interface between different transition metal oxides, as we discussed briefly in Chapter 1.

As we mentioned before, when the carriers are strongly coupled with the lattice, their motion becomes strongly entangled with the heavy phononic degrees of freedom. Hence the effective mass cab be very large and the electrons can turn into polarons. The concept of a polaron has been introduced by Landau to describe a state in which the presence of an electron is associated to a finite lattice distortion, which further binds the electron leading to what Landau describes as an electron digging its own potential well. If we follow the properties of an electron as a function of its coupling with the lattice, we find a continuous evolution from a perturbative regime, in which the electron-phonon coupling only leads to a small effective mass correction, to a strongly coupled polaronic regime, in which the hopping is exponentally renormalized and the carrier is almost localized. The crossover becomes sharper and sharper as the phonon frequency is reduced and it turns into an actual transition in the limit of vanishing phonon frequency, when the phonons become classical variables.

The simplest model Hamiltonian that encloses polaron physics and Coulomb electron-electron correlation on equal footing, is the Holstein electron-phonon coupling Hamiltonian, which assumes an on-site coupling between a dispersionless Einstein phonon and the electronic density fluctuations:

$$\mathcal{H} = \mathcal{H}_{tU\mu} + \sum_i \left[\omega_o \hat{b}_i^\dagger \hat{b}_i + g \left(\hat{b}_i^\dagger + \hat{b}_i \right) \left(\sum_\sigma \hat{n}_{i\sigma} - 1 \right) \right] \tag{2.13}$$

where $\mathcal{H}_{tU\mu}$ is the Hubbard Hamiltonian of Eq.[2.5] and $\hat{b}_i \left(\hat{b}_i^\dagger\right)$ are the annihilation (creation) operators of a phonon of frequency ω_o on the site i. Here we introduce directly a Hubbard-Holstein model which also features the Hubbard interaction, but we will first discuss results in the absence of the Coulomb repulsion.

The relevant parameters of the Holstein model are the dimensionless electron-phonon coupling:

$$\lambda = \frac{2g^2}{\omega_o D} \tag{2.14}$$

and the adiabatic ratio between phononic and electronic charateristic energy scales:

$$\gamma = \frac{\omega_o}{D} \tag{2.15}$$

being D the half-bandwith as usual. Depending on γ one can identify two regimes: in the *adiabatic limit*, which is realized in most materials, the phonon energy is small compared to the half-bandwith, $\gamma \ll 1$. This corresponds to the situation in which the phonon timescales are long compared to the electronic ones, and the lattice polarization is retarded due to a large ionic mass.

In the opposite *anti-adiabatic* $\lambda \gtrsim 1$, limit we assume that the phonons are faster than the electrons, so that the phonon-mediated interaction between the electrons becomes instantaneous. This regime is of course hardly realized in actual materials, unless one considers the ratio between a bare phonon frequency and a renormalized bandwidth arising from strong correlations. A similar approach has been employed in studies of superconductivity in alkali-doped fullerides[20, 18].

From basic notions on the quantum harmonic oscillator one knows that the bosonic operators can be expressed in terms of momentum and position operators $\hat{b}_i^\dagger = \sqrt{\frac{1}{2M_i\omega_o}}\,(M_i\omega_o\hat{x}_i - i\hat{p}_i)$ and his hermitian conjugate. With this canonical transformation the Hamiltonian of Eq.[2.13] becomes:

$$\mathcal{H} = \mathcal{H}_U + \sum_i \left[\frac{\hat{p}_i^2}{2M_i} + \frac{1}{2}M_i\omega_o^2\hat{x}_i^2 + \beta\hat{x}_i \left(\sum_\sigma \hat{n}_{i\sigma} - 1 \right) \right] \tag{2.16}$$

from which is clear that, due to the interaction with the electrons, the phononic oscillator amplitude is shifted. In the adiabatic limit, i.e. $M_i \to \infty$, the Born-Oppenheimer principle can be applied and the groundstate can be factorized in the electronic and phononic contribution $|\Psi_o\rangle = |\Psi_{el}\rangle\,|\Psi_{ph}\rangle$ with $|\Psi_{el}\rangle$ depending parametrically from the atomic displacements x_i.

The $e-ph$ incteraction naturally gives rise to an effective interaction which drives the system towards a superconducting instability. As a function of the $e-ph$ coupling we have a crossover from a standard BCS superconductor to a strong-coupling bipolaronic superconductivity, which is the phononic version of the BCS-BEC crossover of the attractive Hubbard model. A bipolaron is indeed a pair of polarons which is bound at very high temperature because of the energetic gain in sharing the same lattice distortion. At much lower temperature bipolarons condense leading to a superconductor. The crossover is also characterized by a reduction of the coherence length of the pairs. While the weak-coupling pairs of BCS theory are extremely delocalized, bipolaronic binding occurs on very short distances, and it is therefore a reasonable candidate to describe the real-space pairing effects observed in TMO[15, 13] and other superconducting materials [6]. In such correlated systems the instantaneous $e-e$ and the retarded $e-ph$ interactions are comparable and, remarkably, the retarded nature of the latter, can stabilize the pair formation even in the presence of large Coulomb repulsion. The $e-ph$ interaction strength of the known correlated materials is in the intermediate region, where perturbative approaches fails. However, analyzing the two limits, one can gain informations which are valid also far from the range of applicability of perturbation expansions.

2.2.1 Weak-coupling limit

Switching on the $e-ph$ interaction the electron becomes weakly dressed resulting in an increase of the effective mass, and an effective retarded interaction between electrons on different sites is introduced. The latter can be deduced from second-order perturbation theory in the coupling constant g but we find it simpler to derive it from a path-integral formulation. The action related to the electron-phonon coupling in the Holstein-Hubbard hamiltonian is:

$$\mathcal{S}_{e-ph}=\int_0^\beta d\tau\sum_i\left[\hat{b}_i^\dagger\left(\tau\right)D^o_{\hat{b}_i}\left(\tau\right)\hat{b}_i\left(\tau\right)+g\left(\hat{b}_i^\dagger\left(\tau\right)+\hat{b}_i\left(\tau\right)\right)\left(\sum_\sigma\hat{n}_{i\sigma}\left(\tau\right)-1\right)\right] \tag{2.17}$$

where we defined the inverse propagator of the non-interacting phonon on the i-th lattice site $D^o_{\hat{b}_i}\left(\tau\right)=\left(\partial_\tau+\omega_o\right)$. Using the standars formulas for multidimensional complex gaussian integration, one can extract the effect of the phonon field over the electronic degrees of freedom computing the effective electron-phonon action:

$$\mathcal{S}_{e-ph}^{eff} = \int_0^\beta d\tau d\tau' \sum_i \left[\left(\sum_\sigma \hat{n}_{i\sigma}(\tau) - 1 \right) \mathcal{G}_{\hat{b}_i}^o (\tau - \tau') \left(\sum_\sigma \hat{n}_{i\sigma}(\tau') - 1 \right) \right] \tag{2.18}$$

where:

$$\begin{aligned} \mathcal{G}_{\hat{b}_i}^o (\tau - \tau') &= -g^2 \left[D_{\hat{b}_i}^o (\tau) \right]^{-1} \delta (\tau - \tau') \\ &= -g^2 \left[\partial_\tau + \omega_o \right]^{-1} \delta (\tau - \tau') \end{aligned}$$

takes the form of an *effective retarded density-density interaction*. We can gain a deeper physical insight in Matsubara frequency representation, where the action of Eq.[2.18] reads:

$$\mathcal{S}_{e-ph}^{eff} = \sum_{nl} \sum_i \left[\left(\sum_\sigma \hat{n}_{i\sigma}(i\omega_n) - 1 \right) \frac{g^2}{i\Omega_l - \omega_o} \left(\sum_\sigma \hat{n}_{i\sigma}(i\omega_n) - 1 \right) \right] \tag{2.19}$$

The denominator can be rewritten as:

$$\begin{aligned} \sum_l \frac{1}{i\Omega_l - \omega_o} &= \sum_{l>0} \frac{1}{2} \left[\frac{1}{i\Omega_l - \omega_o} + \frac{1}{-i\Omega_l - \omega_o} \right] \\ &= \sum_{l>0} \frac{1}{2} \left[\frac{1}{i\Omega_l - \omega_o} - \frac{1}{i\Omega_l + \omega_o} \right] \\ &= \sum_{l>0} \frac{\omega_o}{(i\Omega_l)^2 - \omega_o^2} \end{aligned}$$

Focusing on the half-filling case, i.e. when $\hat{n}_{i\uparrow} + \hat{n}_{i\downarrow} = 1$, the particle-hole symmetric factor $\left(\sum_\sigma \hat{n}_{i\sigma}(i\omega_n) - 1 \right)^2$ gives the additional factor of 2. Finally one obtains the well known renormalized retarded interaction for the half-filled

Hubbard-Holstein model:

$$U_{e-ph}\left(\omega\right) = U+\frac{2g^2\omega_o}{\omega^2-\omega_o^2}=U+\frac{\omega_o^2}{\omega^2-\omega_o^2}\lambda D \tag{2.20}$$

In the antiadiabatic limit, when the ion motion is istantaneous, the interaction becomes istantaneous as well, eventually resulting in an effective attractive Hubbard Model with $U_{e-ph}\left(\omega\right)=U-\lambda D$.

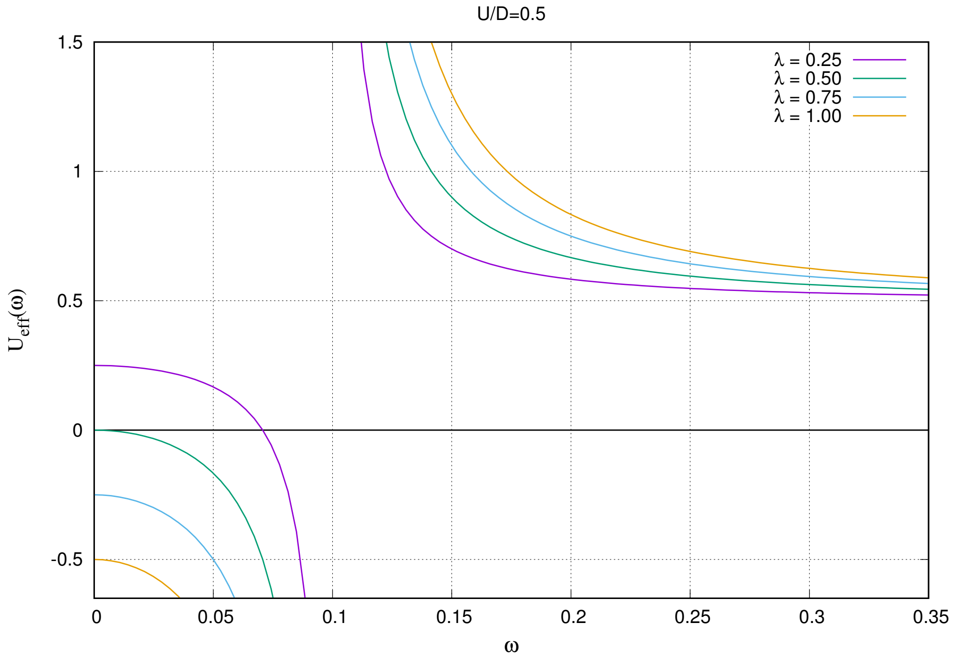

Figure 2.2: Effective potential of Eq.[2.20] for $U=0.5$ and various $e-ph$ interaction strength

2.2.2 Strong-coupling limit

When $\lambda \gtrsim 1$ the hopping part of Eq.[2.13] can be trated perturbatively with the Lang-Firsov canonical transformation with a unitary operator[1] defined as:

$$\hat{\mathrm{S}} = -\frac{g}{\omega_o}\sum_{i\sigma}\hat{n}_{i\sigma}\left(\hat{b}_i^\dagger - \hat{b}_i\right) \tag{2.22}$$

the rotated operators[2] are:

$$\begin{aligned}\tilde{b}_i &= \hat{b}_i + \frac{g}{\omega_o}\sum_{\sigma}\hat{n}_{i\sigma}\\ \tilde{c}_i &= \hat{c}_i e^{\frac{g}{\omega_o}\left(\tilde{b}_i^\dagger - \tilde{b}_i\right)}\end{aligned}$$

---

[1] The canonical transformation can be physically interpreted as a shift of the ions position at the site where the phase fluctuation occurs:

$$\langle\tilde{x}_i\rangle \sim \left\langle\tilde{b}_i^\dagger + \tilde{b}_i\right\rangle = \left\langle\hat{b}_i^\dagger + \hat{b}_i + \frac{2g}{\omega_o}\sum_{\sigma}\hat{n}_{i\sigma}\right\rangle = \langle\hat{x}_i\rangle + \frac{2g}{\omega_o}\sum_{\sigma}\langle\hat{n}_{i\sigma}\rangle \tag{2.21}$$

[2] Where we used:

$$\begin{aligned}\tilde{O} &= e^{\hat{\mathrm{S}}}\hat{O}e^{-\hat{\mathrm{S}}}\\ &= \hat{O} + \left[\hat{\mathrm{S}},\hat{O}\right] + \frac{1}{2}\left[\hat{\mathrm{S}},\left[\hat{\mathrm{S}},\hat{O}\right]\right] + \dots\end{aligned}$$

In this new basis the phononic contribution is diagonal, while the electrons acquire a phase shift $\tilde{\theta}_i = e^{\frac{g}{\omega_o}(\tilde{b}_i^\dagger - \tilde{b}_i)}$. The hamiltonian now reads:

$$\begin{aligned}
\tilde{\mathcal{H}} &= -t\sum_{ij\sigma}\left[\tilde{c}_{i\sigma}^\dagger \tilde{c}_{j\sigma}\tilde{\theta}_i^\dagger\tilde{\theta}_j + h.c.\right] \\
&\quad + \sum_i\left[\omega_o \tilde{b}_i^\dagger \tilde{b}_i - \left(\mu - \frac{g^2}{\omega_o}\right)\sum_\sigma \tilde{n}_{i\sigma} + \left(U - \frac{2g^2}{\omega_o}\right)\tilde{n}_{i\uparrow}\tilde{n}_{i\downarrow}\right] \qquad (2.23) \\
&= \tilde{\mathcal{H}}_t + \sum_i\left[\omega_o \tilde{b}_i^\dagger \tilde{b}_i - \frac{\lambda D}{2}\sum_\sigma \tilde{n}_{i\sigma} + \lambda D \tilde{n}_{i\uparrow}\tilde{n}_{i\downarrow}\right] \qquad (2.24)
\end{aligned}$$

From this expression we can extract valuable information.

- the unitary operator Ŝ involves the total density, rather than density fluctuations as in Eq.[2.13]. This allow us to exactly define the half-filling chemical potential from the atomic $t = 0$ limit of Eq.[2.24], where $\mu = -\lambda D$ results in the lowest energy for the $\sum_\sigma \tilde{n}_{i\sigma} = 1$ configuartion;

- the same quantity can be regarded as the lattice deformation energy gain due to the polaronic formation $E_p = \frac{g^2}{\omega_o} = \frac{\lambda D}{2}$;

- the groundstate of $\tilde{\mathcal{H}}$ is degenerate with respect of the site index i, with an electron for each lattice site. In the strong-coupling limit the translational invariace is broken since all electron are trapped in their "self-digging" hole with a vanishing hopping amplitude at the zeroth order. Consdering the first order kinetic contribution one finds an exponentially decay in the nearest neighbor hopping amplitude [49]:

$$t_{eff} = \langle i|\, \tilde{c}_{i\sigma}^\dagger \tilde{c}_{j\sigma}\tilde{\theta}_i^\dagger\tilde{\theta}_j \,|j\rangle = te^{-\frac{g^2}{\omega_o^2}} = te^{-\frac{\lambda D}{2\omega_o}} = te^{-\frac{E_p}{\omega_o}} \qquad (2.25)$$

- the effective on-site interaction is renormalized by the binding energy of two polarons:

  $$\tilde{U} = U - 2E_p \tag{2.26}$$

  which is the same result of the non-adiabatic limit.

For negative effective interaction $\tilde{U} < 0$ one can easily form bound pairs, but, even for $\tilde{U} > 0$ a polaron bound state can persist. This can be shown with second order perturbation theory with respect of $\tilde{\mathcal{H}}_t$, considering a starting configuration where two electrons with opposite spin resides on adjacent lattice sites $|\Psi\rangle = \hat{c}^{\dagger}_{i\uparrow}\hat{c}^{\dagger}_{i+a\downarrow}|0\rangle$. Following [[49, 55]], two kind of hoppings can be identified: those exponentially vanishing in the strong-coupling limit, of the kind of Eq.[2.25], related to a different initial and final lattice configuration, and the non-vanishing ones. The latter correspond to processes where the lattice configuartion is left unchanged, but electrons hops out on neighbouring sites, without carrying the lattice deformation, and subsequently hops back on the original site. The virtual intermediate state has an energy of $2E_p$, since it contanis a polarized site without the electron and an electron in an undistorted site, then a global energy gain of $-t^2/2E_p$ is provided by this process. If, in the intermediate virtual state, the arrival lattice site already contains an electron an additional energy cost of U has to be considered giving a correction of $-t^2/U$. All these energy contribution are computed from:

$$\tilde{\mathcal{T}} = \tilde{\mathcal{H}}_t \left[\epsilon - \tilde{\mathcal{H}}\right]^{-1} \tilde{\mathcal{H}}_t \tag{2.27}$$

over a small irreducible subset of degenerate states of $\tilde{\mathcal{H}}$. The existence condition for the bipolaron is found upon diagonalizing the operator of Eq.[2.27] with a binding energy of:

$$\Delta E = -\frac{t^2}{E_p} + \frac{4t^2}{U} \tag{2.28}$$

this means that the bipolaron is stable, even if composed by weakly bounded polarons, when:

$$U < 4E_p \tag{2.29}$$

or alternatively:

$$\lambda > \frac{1}{2}\frac{U}{D} \tag{2.30}$$

In conclusion, the bipolaron bound state begin start to appear already when the global interaction of Eq.[2.20] is negative, i.e for $\frac{1}{2}\frac{U}{D} < \lambda < \frac{U}{D}$, and persists when the rescaled interaction becomes attractive at $\lambda > \frac{U}{D}$ eventually stabilizing a superconducting phase.

2.2.3 The bipolaron insulator in the Holstein model and phonon softening precursor

As we discussed bipolarons can condensate with a Bose-Einstein mechanism eventually leading to superconductivity[2]. If superconductivity is prevented, the bipolarons can condense in a charge-ordered insulating state, composed by pairs localized in their self-trapping potential. Indeed it has been demonstrated [17] that the metal-insulator transition (MIT) is not associated to the formation of individual polarons, and insulating behavior can be associated only with localized bipolarons. Calculation performed mainly with DMFT [17, 53] demonstrated that, for the *pure Holstein model*, i.e. when $U = 0$, in the adiabatic regime the MIT is located at $\lambda_c \approx 0.76 \div 0.8$[3].

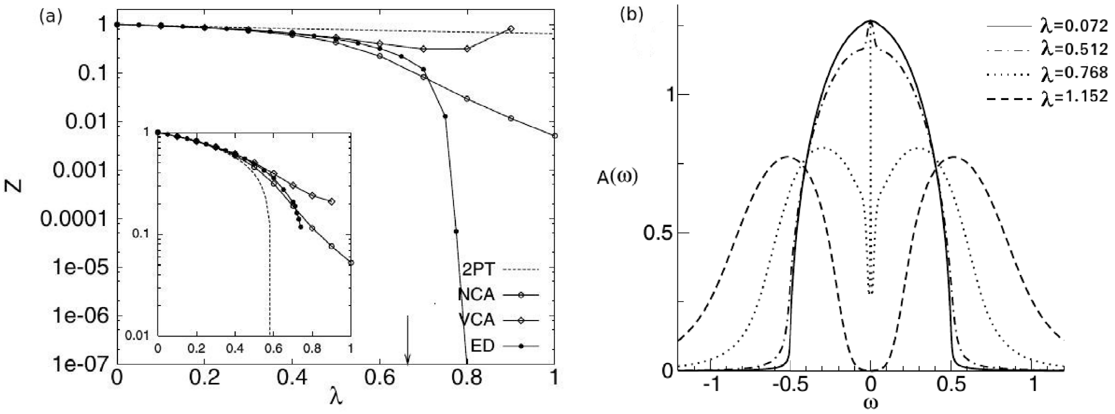

Figure 2.3: (a) z and Ω/ω_o (inset) for $\gamma = 0.1$ vs λ in a DMFT(ED) calculation. The arrow marks the MIT for $\gamma = 0$ as in [16]; (b) Electronic spectral function for various $e-ph$ coupling λ

Through a mean field analysis of the model[8], it has been shown how the nature of this insulating phase is deeply connected with the CDW instability. The latter instability shows up, at mean-field level, at $\lambda_{CDW}^{(mf)} = 0.578$ with two peaks in the spectral functions shifted of $\pm g x_{mf}$ above and below the Fermi level. This behavior can be explained in terms of an effective potential for the ions $V_\lambda(x)$. The static field x can be written in terms of both the average ion displacement and the average of the total density fluctuation either, which are linearly coupled in the Holstein hamiltonian:

$$\begin{aligned} x &= \frac{1}{\sqrt{2M\omega_o}} \left\langle \hat{b}^\dagger + \hat{b} \right\rangle \\ &= -\frac{2}{\sqrt{\omega_o}} \frac{g}{\omega_o} \left\langle \sum_\sigma \hat{n}_\sigma - 1 \right\rangle \end{aligned}$$

---

[3] In the anti-adiabatic limit the MIT occurs when $\lambda_c \approx 1.44$, at the same time the non-vanishing value of Ω/ω_o indicates that the phonon renormalization is less effective.

For $\lambda < \lambda_{CDW}^{(mf)}$, $V_{\lambda}(x)$ is a simple harmonic potential, while at $\lambda > \lambda_{CDW}^{(mf)}$ it becomes a double-well potential with minima at $\pm g x_{mf}$ and a central barrier that rapidly grows with λ. When $\lambda \gg \lambda_{CDW}^{(mf)}$ the central barrier will exponentially restrain the hopping between the two minima making the groundstate an incoherent superposition of doubly occupied and empty sites. This will lead to a charge-ordered state in calculations where the translational symmetry can be broken.

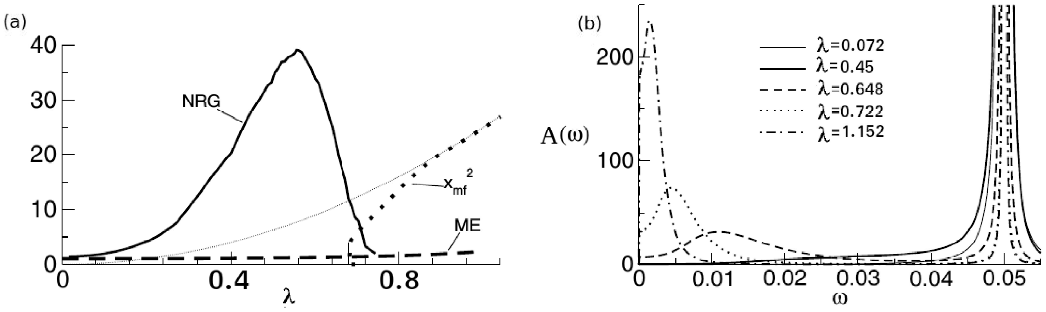

Figure 2.4: (a) Lattice fluctuations $\left\langle \hat{x}^2 - \langle \hat{x} \rangle^2 \right\rangle$ as computed in Ref.[53] ,the thick dotted line represents the mean-field value x_{mf}^2 and the thin dotted line shows the $\lambda \to \infty$ limit for the same quantity; (b) Phonon propagator spectral function $A(\omega) = -\frac{1}{\pi} \Im D(\omega)$ showing a softening with increasing λ.

As shown in Fig.[2.2.3] the expectation value of the fluctuations of the displacement $\left\langle \hat{x}^2 - \langle \hat{x} \rangle^2 \right\rangle$ computed on top of the mean field, extends shortly above $\lambda_{CDW}^{(mf)}$ and has a maximum at $\lambda^* < \lambda_{CDW}^{(mf)}$, in the crossover region towards the double-well structure, where the potential is broad and shallow. The effect of this enhancement in the displacement fluctuation can be understood computing the phonon propagator:

$$D(i\Omega_n) = \int_0^{\beta} d\tau e^{i\Omega_n \tau} \left\langle \mathrm{T} \left[\left(\hat{b}^{\dagger}(\tau) + \hat{b}(\tau) \right) \left(\hat{b}^{\dagger} + \hat{b} \right) \right] \right\rangle \tag{2.31}$$

from which the renormalized phonon frequency ${}^{\Omega}/_{\omega_o}$ can be extracted as:

$$\left(\frac{\Omega}{\omega_o}\right)^2 = -\frac{2}{\omega_o D\left(0\right)} \tag{2.32}$$

As can be seen from Fig.[2.3] this quantity is decreasing with λ, showing that the transition toward the insulator has a precursor in the phonon softening [53]. In particular, looking at the spectral function of the phonon propagator $A\left(\omega\right) = -\frac{1}{\pi}\Im\left\{D\left(\omega + i0^+\right)\right\}$ reported in Fig.[2.2.3], the phonon softening is related to an increase of a low-frequency peak occurring exactly at $\lambda = \lambda^*$ where the two minima in the effective potential starts to deepen and the fluctuations have their maximum. The connection between position fluctuation and phonon softening comes from the fact that in the model the position operator is linearly coupled to the electronic density. Indeed, another way to derive the phonon propagator is:

$$D\left(i\Omega_n\right) = D_o\left(i\Omega_n\right) + D_o\left(i\Omega_n\right) g^2 \chi_c\left(i\Omega_n\right) D_o\left(i\Omega_n\right) \tag{2.33}$$

where $\chi_c\left(i\Omega_n\right)$ is the charge susceptibility and $D_o\left(i\Omega_n\right) = \left(\Omega_n - \omega_o\right)^{-1}$ is the bare phonon propagator. Eq.[2.33] shows how strictly $D\left(i\Omega_n\right)$ depends on χ_c: the peak in $A\left(\omega\right)$ has its equivalence in a low-energy peak of χ_c, which is the precursor of the metal to bipolaronic insulator transition. An alternative argument leading to the same conclusion starts form the mapping of the Holstein model into the attractive Hubbard model in the antiadiabatic limit. As we described above, the latter can be inturn mapped onto a repulsive Hubbard model with an exchange in the spin and charge channels. Hence the low-energy peak in the spin susceptibility, which is the precursor of the insulating phase, will have an equivalent peak in the charge susceptibility in the Holstein model.

2.2.4 The Holstein-Hubbard model phase diagram at half-filling

In the case of the Holstein-Hubbard model the situation is far more involved, since, even if a bound state exists for relatively large values of the Hubbard interaction U, it is not easy to find analytically when the bipolaronic insulating phase becomes the groundstate. The results of several numerical simulations [16, 8, 17, 30, 41] can shed light on this point, in the following we will focus on those based on Dynamical Mean-Field Theory.

In Fig.[2.5] we report the zero-temperature phase diagram of the model for a system with a semi-elliptic density of states of half-bandwidth D in the paramagnetic sector where all the broken-symmetry phases such as CDW, Superconductivity and antiferromagnetism are inhibited.

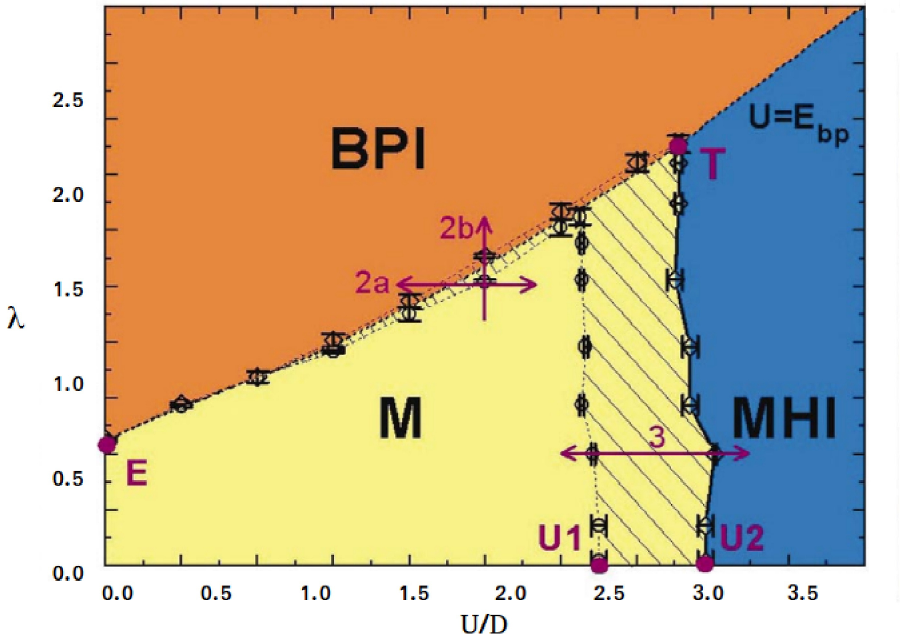

Figure 2.5: Phase diagram of the half-filled Holstein-Hubbard model over the $e-ph$ coupling λ and the Hubbard interaction U/D in the adiabatic $(\gamma = 0.05)$ regime. The yellow region stands for metal (M), orange for bipolaronic insulator (BPI) and blue for Mott Hubbard insulator (MHI)

When both the bipolaron energy $E_{bp}/D = \lambda$ and the Hubbard interaction U/D are small, the groundstate is metallic (M). For large λ and zero or small U we recover the transition to the bipolaronic insulator (BPI), while, in the large U regime and zero or small λ, we reach the standard Mott-Hubbard insulator (MHI). In particular, we obviously recover the two limiting cases of the model, namely the pure Holstein model with $\lambda_c \approx 0.6$ and the Single band Hubbard model with $U_{c1} \approx 2.75D$ and $U_{c2} \approx 3D$. The degree of correlation of the metallic state, reflected by the inverse of the quasiparticle weight z, increases with increasing either λ or U. The boundary of the BPI phase λ_c increasing with U due to the fact that the attractive $e-ph$ interaction must overcome the repulsive interaction to localize the bipolaron after the formation of the bound state. On the other hand the boundary of the Mott phase U_c weakly depends on λ because the phonons are coupled with density fluctuations which are frozen close to the Mott transition.

One can gain more understanding of the phase diagram considering the effective retarded interaction of Eq.[2.20]. The Hubbard repulsion and the phononic potential compete in the adiabatic limit, while in the antiadiabatic limit, for large enough λ, the model can be mapped into the attractive Hubbard model. For this reason the $\lambda = U/D$ line plays a crucial role in the phase diagram as, for large enough interaction strength, the three phases converge on a tricritical point on this line.

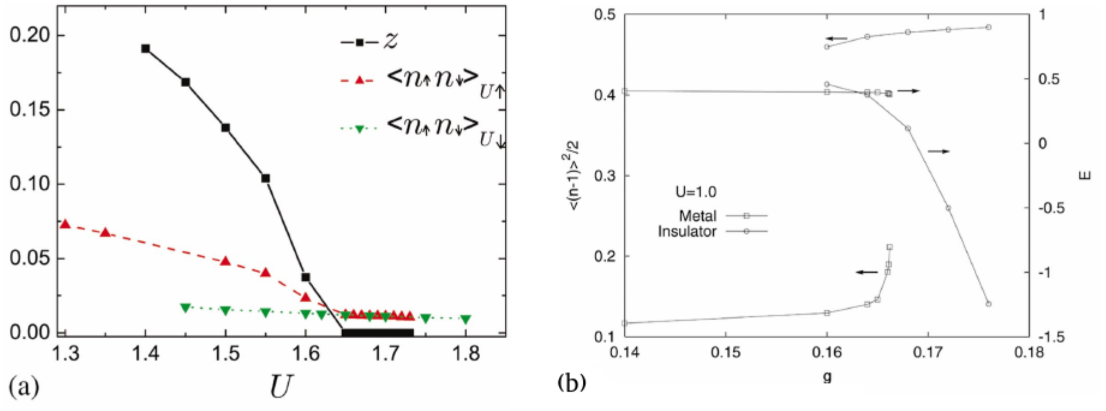

Figure 2.6: (a), z as U is increased, and $\langle n_\uparrow n_\downarrow\rangle$ as U is increased and decreased along the cut 3 of Fig.[2.5]; (b) double occupancy in M state, and ground state energy E along the cut 2a in Fig.[2.5] as U is increased (for M) or decreased (for BPI). The phase transition occurs at $U \sim 0.96$ where the energies of the M and BPI states become the same.

As shown by Fig.[2.6] the M-MHI transition is second order for any value of λ since $\langle n_\uparrow n_\downarrow\rangle^{(M)}$ and $\langle n_\uparrow n_\downarrow\rangle^{(MHI)}$ meets at U_{c2} while the M-BPI one is first order since $\langle n_\uparrow n_\downarrow\rangle^{(M)}$ and $\langle n_\uparrow n_\downarrow\rangle^{(BPI)}$ do not match at λ_c. The nature of the BPI can be understood considering the $U = 0$ and $\lambda = \infty$ limit of the Holstein-Hubbard model, where the $e - ph$ coupling favors only the empty and doubly occupied states. As we discussed, this state is naturally unstable towards a CDW which we was not allowed in the calculations we discuss. For this reason, also in this model, the BPI is identified by a degenerate groundstate with respect of $C = \langle\sum_\sigma \hat{n}_\sigma - 1\rangle \approx 1$ and $C = \langle\sum_\sigma \hat{n}_\sigma - 1\rangle \approx -1$ states, reflecting the nature of the BPI as a incoherent superposition of doubly occipied and empty sites.

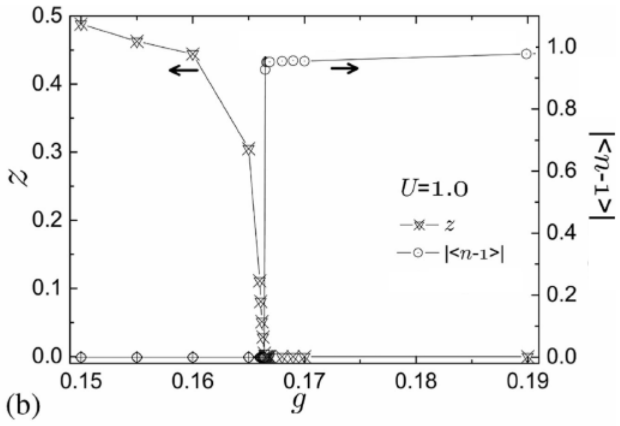

Figure 2.7: Plots of z and C as g is increased along the cut 2b of Fig.[2.5]

Fig.[2.7] shows how the expectation value of C versus the $e-ph$ coupling constant g, at a fixed $U/D = 1$, increases from zero to a finite value discontinuously.

Focusing on the particular case of a strongly correlated metallic regime, i.e. close to the Mott transition, it has been demonstrated that the electronic quasiparticle weight is unaffected by the $e-ph$ coupling[74]. As we described above, at $U = 0$, the effect of the $e-ph$ coupling is to decrease z_{qp}, reflecting the crossover to polaronic carriers and eventually reaching the bipolaronic metal-insulator transition. Switching on the Hubbard repulsion, $z_{qp}(U, \lambda)$ is found to be a decreasing function for any value of the coupling strength. However, the ratio $z_{qp}(U, \lambda)/z_{qp}(U, 0)$ has the non monotonic behavior reported in Fig.[2.8] that can be explained thinking in terms of a reduction of the effective repulsion prevailing against the hopping polaronic renormalization.

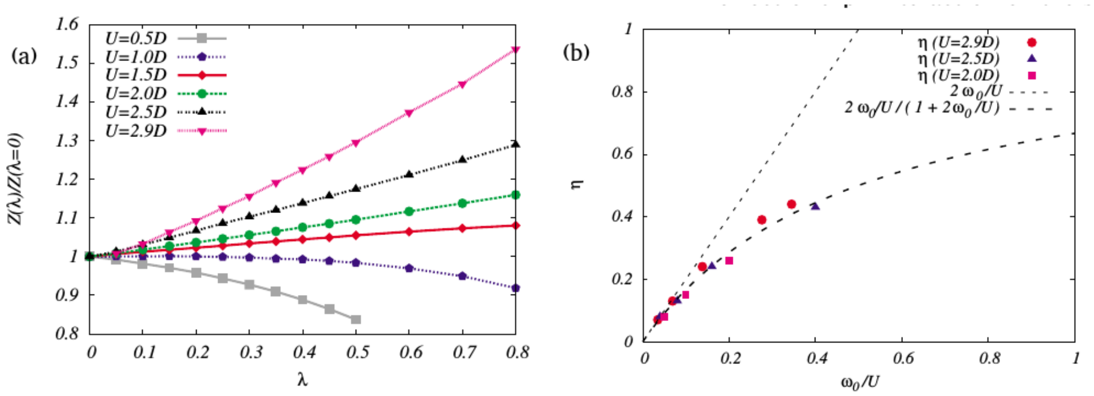

Figure 2.8: (a)The ratio $z_{qp}\left(U,\lambda\right)/z_{qp}\left(U,0\right)$ vs λ is shown for different values of U; (b)the coefficient η, plotted as a function of $\frac{\omega_o}{U}$

We can define an effective static repulsion U_{eff} that, in the pure Hubbard model, gives the same value of the quasiparticle weight so that $z_{qp}\left(U_{eff},0\right) = z_{qp}\left(U,\lambda\right)$. It has been shown in Ref.[74] that the effective repulsion can be parametrized as:

$$U_{eff} = U - \eta\lambda D \tag{2.34}$$

where the dimensionless parameter η can be directly derived from the leading order in the $1/U$ expansion of the Kondo model, whose physic is captured by DMFT. The Kondo coupling is poorly affected by the $e-ph$ coupling in the adiabatic limit due to the fact that the two kind of electronic processes enclosed in the model, namely the double occupancy of a lattice site and the phonon excitation, resides in different time domains. In the strongly correlated regimes, when $U \gg \omega_o$ the first is a “fast” process which takes place in a frozen phononic configuration as we described in Sec 2.1.2.2. The correction of the Kondo coupling due to the phononic degrees of freedom is:

$$\frac{J_K(\lambda)}{J_K(0)} \sim 1 + \eta \frac{\lambda D}{U} \tag{2.35}$$

which gives the effective static U_{eff} of Eq.[2.34] for the Kondo model in terms of the parameter:

$$\eta = \frac{\frac{2\omega_o}{U}}{1 + \frac{2\omega_o}{U}} \tag{2.36}$$

Fig.[2.8] shows how this functional form is able to capture the behavior of η for various ω_o/U obtained from DMFT calculations. Another confirmation that $e-ph$ coupling do not affect the low energy physics of the systems comes looking at the spectral function of the pure Hubbard model at U_{eff} and the one of the Holstein-Hubbard model.

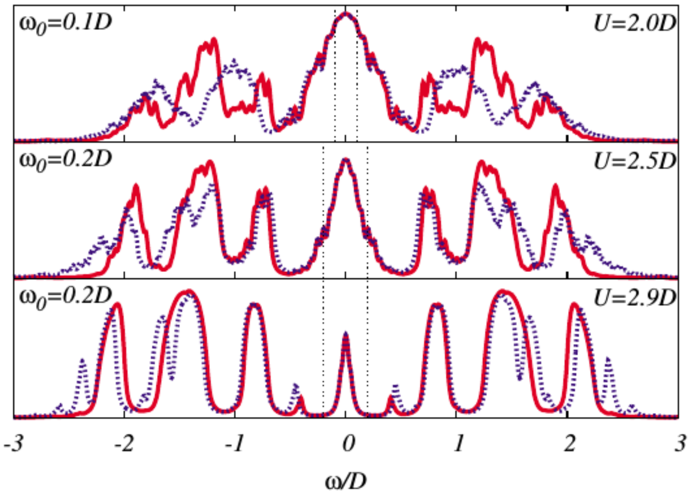

Figure 2.9: The electron spectral function for the Hubbard-Holstein model (dashed line), compared with a pure Hubbard model

Indeed in Fig.[2.2.4] the low energy part of the spectrum is identical, while major changes occur only at high energy scale.

2.3 Spin Orbit Coupling in d orbitals

The Spin Orbit Coupling (SOC) is an interaction between the electronic spin $\mathbf{S}$ and his orbital angular momentum $\mathbf{L}$[4]. It follows from the non relativistic expansion of the Dirac Hamiltonian and, for potentials with spherical symmetry, reads:

$$\mathcal{H}_{SOC} = \frac{1}{2\left(m_0 c\right)^2}\frac{1}{r}\frac{dV}{dr}\mathbf{L}\cdot\mathbf{S} \tag{2.37}$$

Due to this term in Hamiltonian, the groundstate of a single electron atom is no longer degenerate with respect of L ans S, resulting in a so called fine structure splitting between the $(2L+1)(2S+1)$ levels with different $J = L + S$. Indeed this splitting can be evaluated considering the expectation value:

$$\mathcal{H}_{SOC} = \lambda_{SOC}\frac{1}{2}\left(J\left(J+1\right) - L\left(L+1\right) - \frac{3}{4}\right) \tag{2.38}$$

where λ_{SOC} is the expectation value of the coupling strength. Considering a simple $V \sim {}^{1}\!/_{r}$ potential it can be shown that λ_{SOC} scales like Z^4 being Z the atmic number, so it is straightforward for havy elements to have non negligible SOC. For multi-electron atoms the coupling between spin and orbital degrees of freedom can be descibed in two ways:

- In the Russel-Sanders coupling the *total* angular momentum $\mathbf{L} = \sum_i \mathbf{j}_i$ of the electronic shell is coupled with the *total* spin $\mathbf{S} = \sum_i \mathbf{s}_i$ resulting in a splitting with a multiplicity of $2S+1$ if $L \geqslant S$ or $2L+1$ otherwise and an

---

[4] In order to avoid misunderstanding we will use capital bold letters to indicate total vectors resulting from the sum over all the electrons while the standard character refers explicitly to a particular component. When the component is unspecified we refer to the eigenvalue of the matrix representation labelled with “ ˆ ”. Lowercase letters are referred to single electron variable.

energy separation proportional to λ_{SOC}.

- In the *jj* coupling, typical in the case of heavy elements, the SOC is comparable to all the other energy scales, therefore the total angular momentum of a *single* electron $\mathbf{j} = \mathbf{l} + \mathrm{s}$ is the conserved quantity.

These two kinds of coupling are indeed limiting cases of the phenomenology which are usuful to understand the more involved situation in actual materials. In general the SOC will have some intermediate strength that, generally speaking, shifts from the first to the second kind taking into consideration heavier elements. It is important to underline that the Hund's third rule, which states:

- the lowest $J = |L - S|$ should be selected for less than half-filled shell, while highest $J = L + S$ for densities above half-filling

is the direct consequence of the presence of SOC. Focusing on the particular case of interest for TMO, i.e. d orbitals in cubic symmetry, the five-fold degeneracy is already lifted by a crystal field splitting between the e_g and t_{2g} subset.

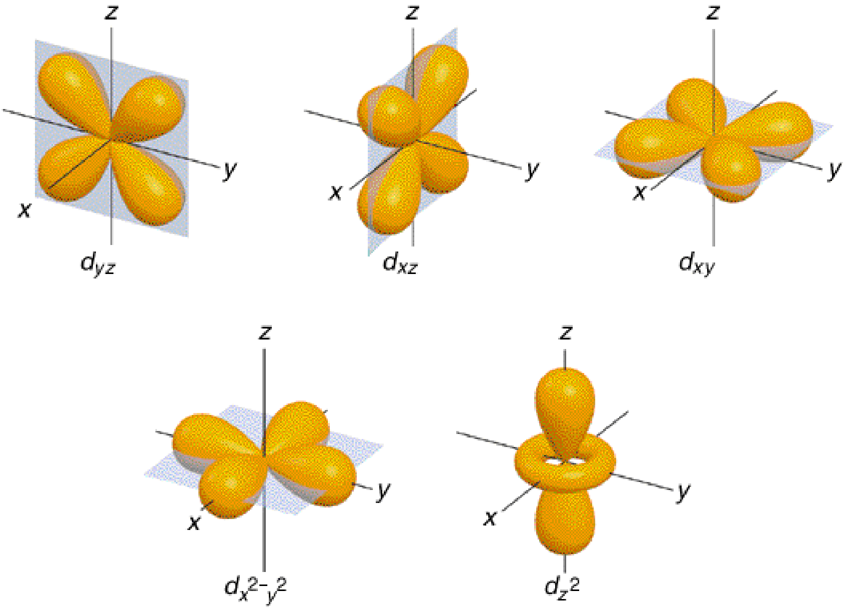

Figure 2.10: Density probability distribution of d orbitals.

This can be naively understood considering that, typically, the transition metal atom is enclosed in an octahedron surrounded by six ligand atoms and looking at Fig.[2.10] one sees that t_{2g} orbitals are not oriented in the direction of the ligand point charges, resulting in a geometrical configuration more stable against the Coulomb repulsion. The energy splitting is given by[71]:

$$\begin{aligned}\epsilon\left(t_{2g}\right) &= \epsilon\left(d\right)+\frac{6Ze^2}{a}-4Dq\\ \epsilon\left(e_{g}\right) &= \epsilon\left(d\right)+\frac{6Ze^2}{a}+6Dq\end{aligned}$$

where $D=\frac{35Ze^2}{4a^5}$ and $q=\frac{2}{105}\int r^6\left|R_{nd}\left(r\right)\right|^2dr$. In the basis $\{d_{yz},d_{zx},d_{xy},d_{3z^2-r^2},d_{x^2-y^2}\}$ the d orbitals are splitted in a e_g doublet and a t_{2g} triplet so the three component of the orbital andular momentum of a single electron have the following representation:

$$\begin{aligned}
\hat{l}^x &= \begin{pmatrix} 0 & 0 & 0 & -i\sqrt{3} & -i \\ 0 & 0 & i & 0 & 0 \\ 0 & -i & 0 & 0 & 0 \\ i\sqrt{3} & 0 & 0 & 0 & 0 \\ i & 0 & 0 & 0 & 0 \end{pmatrix} \\
\hat{l}^y &= \begin{pmatrix} 0 & 0 & -i & 0 & 0 \\ 0 & 0 & 0 & i\sqrt{3} & -i \\ i & 0 & 0 & 0 & 0 \\ 0 & -i\sqrt{3} & 0 & 0 & 0 \\ 0 & i & 0 & 0 & 0 \end{pmatrix} \\
\hat{l}^z &= \begin{pmatrix} 0 & i & 0 & 0 & 0 \\ -i & 0 & 0 & 0 & 0 \\ 0 & 0 & 0 & 0 & 2i \\ 0 & 0 & 0 & 0 & 0 \\ 0 & 0 & -2i & 0 & 0 \end{pmatrix}
\end{aligned} \tag{2.39}$$

These matrices are hermitian with purely imaginary elements. Since the matrix elements in the e_g subspace are zero, the SOC will be zero as well, since for these states the orbital angular momentum is completely quenched. This is true as long as the orbital splitting induced by the crystal symmetry is much larger than the one induced by SOC. Moreover for the non-vanishing block matrix in the t_{2g} subspace the following relation holds:

$$\hat{\mathbf{l}}\left(t_{2g}\right) = -\hat{\mathbf{l}}\left(p\right) \tag{2.40}$$

which means that the expectation value of $\hat{\mathbf{l}}^2\left(t_{2g}\right)$ is $l\left(l+1\right)$ with $l = 1$ rather than $l = 2$ as one would have expected for d orbitals. This is the so called TP-equivalence. It is important to underline that this is only a formal equivalence, indeed $\hat{\mathbf{l}}\left(t_{2g}\right)$ do not satisfy the angular momentum commutation relation, since the off-diagonal elements connecting the t_{2g} and the e_g are neglected. To compute the matrix representation of the SOC hamiltonian $\mathcal{H}_{SOC} = \lambda_{SOC}\hat{\mathbf{l}} \otimes \hat{\sigma}$ in the most general way for d orbitals in cubic symmetry one has to condider the full five dimensional $\hat{\mathbf{l}}$ matrix of Eq. [2.39]. However, it can be shown [71] that the SOC spitting do not mix the two subspaces, being the block off-diagonal elements of $\mathcal{H}_{SOC}$ zero in the $Dq >> \lambda_{SOC}$ limit. Due to this decoupling we are allowed to consider only the t_{2g} orbital angular momentum operator in the SOC hamiltonian:

$$\begin{aligned}
\mathcal{H}_{SOC} &= \lambda_{SOC}\hat{\mathbf{l}}\left(t_{2g}\right) \otimes \hat{\mathbf{S}} \\
&= \lambda_{SOC}\frac{1}{2}\left[\hat{l}^x\left(t_{2g}\right) \otimes \hat{\sigma}^x + \hat{l}^y\left(t_{2g}\right) \otimes \hat{\sigma}^y + \hat{l}^z\left(t_{2g}\right) \otimes \hat{\sigma}^z\right] \\
&= \lambda_{SOC}\frac{1}{2}\begin{pmatrix} 0 & i\hat{\sigma}^z & -i\hat{\sigma}^y \\ i\hat{\sigma}^y & 0 & i\hat{\sigma}^x \\ -i\hat{\sigma}^x & -i\hat{\sigma}^z & 0 \end{pmatrix}
\end{aligned} \tag{2.41}$$

The new good quantum number is therefore $j = l\left(t_{2g}\right) + s$. In this basis the SOC hamiltonian is diagonalized into a $j = 1/2$ doublet, corresponding to the $\xi^{(1)}_{SOC} =$

λ_{SOC} eigenvalue, and a $j = {}^{3}\!/_{2}$ quarted, corresponding to the $\xi^{(2)}_{SOC} = -\lambda_{SOC}/2$ eigenvalue:

$$\mathcal{H}_{SOC} = \lambda_{SOC}\frac{1}{2}\left(j\left(j+1\right) - l\left(l+1\right) - \frac{3}{4}\right) = \begin{cases} \xi^{(1)}_{SOC} = \lambda_{SOC} & (\times 2)\, j = {}^{1}\!/_{2} \\ \xi^{(2)}_{SOC} = -\lambda_{SOC}/2 & (\times 4)\, j = {}^{3}\!/_{2} \end{cases} \tag{2.42}$$

resulting in a global SOC splitting of $\Delta = 3\lambda_{SOC}/2$. The degeneracy can be further split considering the eigenvalues j^z of the z component of the total angular momentum $\hat{j}^z$ defined as:

$$\begin{aligned} \hat{j}_z &= \hat{l}_z\left(t_{2g}\right) \otimes \mathbf{1}^{(2)} + \mathbf{1}^{(3)} \otimes \hat{S}_z \\ &= \begin{pmatrix} \hat{l}_z\left(t_{2g}\right) + \frac{1}{2}\mathbf{1}^{(3)} & 0 \\ 0 & \hat{l}_z\left(t_{2g}\right) - \frac{1}{2}\mathbf{1}^{(3)} \end{pmatrix} \end{aligned}$$

The SOC hamiltonian is then diagonalized in the following basis Θ:

$$\begin{aligned} \left|j = {}^{1}\!/_{2}; j^z = +{}^{1}\!/_{2}\right\rangle &= \frac{1}{\sqrt{3}}\left(-i\left|d_{yz},\uparrow\right\rangle - \left|d_{zx},\uparrow\right\rangle + i\left|d_{xy},\downarrow\right\rangle\right) \\ \left|j = {}^{1}\!/_{2}; j^z = -{}^{1}\!/_{2}\right\rangle &= \frac{1}{\sqrt{3}}\left(-i\left|d_{yz},\downarrow\right\rangle + \left|d_{zx},\downarrow\right\rangle - i\left|d_{xy},\uparrow\right\rangle\right) \end{aligned}$$

$$\begin{aligned} \left|j = {}^{3}\!/_{2}; j^z = +{}^{1}\!/_{2}\right\rangle &= \frac{1}{\sqrt{2}}\left(-i\left|d_{yz},\downarrow\right\rangle - \left|d_{zx},\downarrow\right\rangle\right) \\ \left|j = {}^{3}\!/_{2}; j^z = +{}^{3}\!/_{2}\right\rangle &= \frac{1}{\sqrt{6}}\left(+i\left|d_{yz},\uparrow\right\rangle + \left|d_{zx},\uparrow\right\rangle + 2i\left|d_{xy},\downarrow\right\rangle\right) \\ \left|j = {}^{3}\!/_{2}; j^z = -{}^{3}\!/_{2}\right\rangle &= \frac{1}{\sqrt{6}}\left(-i\left|d_{yz},\downarrow\right\rangle + \left|d_{zx},\downarrow\right\rangle + 2i\left|d_{xy},\uparrow\right\rangle\right) \\ \left|j = {}^{3}\!/_{2}; j^z = -{}^{1}\!/_{2}\right\rangle &= \frac{1}{\sqrt{2}}\left(+i\left|d_{yz},\uparrow\right\rangle - \left|d_{zx},\uparrow\right\rangle\right) \end{aligned}$$

This concludes the description of the fine structure splitting of d orbitals in cubic symmetry.

CHAPTER

3

DYNAMICAL MEAN FIELD THEORY

Despite the formal simplicity the Hubbard model has resisted to the attempts to solve it exactly, except for one dimension, and, as we will discuss in the following, in infinite dimension. A conventional route is given by perturbation expansion around a small parameter such as U/W (weak-coupling expansion), W/U (strong-coupling expansion), $1/T$ (high temperature expansion) or the density n (low density expansion). However, the most interesting and less trivial physics, such as the Mott metal insulator transition at $T = 0$ and half-filling, happens in the case when both kinetic energy and the interaction strength are of the same magnitude, i.e. in the absence of an obvious small parameter and far rom the large-doping and large-temperature limits.

A completely different path has been paved by studies of correlated electrons in infinite coordination, which have shown that a suitable scaling of the hopping matrix elements leads to a finite expectation value of the kinetic energy per site and, consequently, to a "fair" competition with the Hubbard term, which obviously has an extensive expectation value. Therefore an infinite-coordination Hubbard model is expected to display the physics of strong correlations and a Mott transition. On the other hand, this non-trivial physics can exploit important formal simplifications which allow for an exact solution of the Hubbard model. In particular the self–energy of the problem becomes entirely local $\Sigma\left(\mathbf{k}\omega\right) \to \Sigma\left(\omega\right)$, i.e., momentum–independent, while it retains the full ω–dependence[52].

Based on this result, it has been possible to develop the Dynamical mean-field theory (DMFT), one of the most popular and successful theoretical methods to treat strongly correlated electron systems that exploits this result. It extends the classical mean-field approach to the quantum dynamical domain by mapping a lattice model onto an effective impurity model. The latter describes the interaction of the correlated impurity site with a non-interacting self consistently determined electron “bath” through an hybridization function. All the non local degrees of freedom are self-consistently averaged in this effective bath fully retaining the dynamic frequency dependency of the self-energy. In this scheme all the single-site expectation values corresponds to the local projection of the original lattice observables.

3.1 Derivation of the Dynamical Mean-Field Theory Equations

We will briefly sketch the fundamentals steps in the derivation of the DMFT equation following Ref.[31], using functional integral formulation in terms of Grassmann variables. There are several ways to obtain DMFT equations, the one presented relies on the *cavity method*: the underlying idea is to focus on a given lattice site, say "o", assumed to be equivalent to all the other, and to integrate out all the degrees of freedom different from "o". This allows to define an effective local dynamics for site "o" that takes into account the effects of the rest of the lattice. For the single-band Hubbard model the action of the lattice model is defined as:

$$\mathcal{S}\left[\hat{c}^{\dagger}_{i\sigma},\hat{c}_{i\sigma}\right] = \int_0^{\beta} d\tau \sum_{ij\sigma} \hat{c}^{\dagger}_{i\sigma}\left[\left(\partial_{\tau}-\mu\right)\delta_{ij}-t_{ij}\right]\hat{c}_{j\sigma} + U\sum_i \hat{n}_{i\uparrow}\hat{n}_{i\downarrow}$$

The effective action is obtained through field integration over all the fermion fields except of those related to the arbitrary site "o":

$$\frac{1}{\mathcal{Z}_{eff}} e^{-\mathcal{S}_{eff}\left[\hat{c}^{\dagger}_{o\sigma},\hat{c}_{o\sigma}\right]} = \frac{1}{\mathcal{Z}}\int \prod_{ij\neq o\sigma} D\left[\hat{c}^{\dagger}_{i\sigma},\hat{c}_{j\sigma}\right] e^{-\mathcal{S}\left[\hat{c}^{\dagger}_{i\sigma},\hat{c}_{j\sigma}\right]} \tag{3.1}$$

The key quantity will be the Green's function for the fermions on site "o" computed on the effective local action

$$G_{o\sigma\sigma'}\left(\tau\right) = \frac{1}{\mathcal{Z}_{eff}}\int \prod_{\sigma} D\left[\hat{c}^{\dagger}_{o\sigma},\hat{c}_{o\sigma'}\right] \hat{c}^{\dagger}_{o\sigma}\left(\tau\right)\hat{c}_{o\sigma'}\left(0\right) e^{-\mathcal{S}_{eff}\left[\hat{c}^{\dagger}_{o\sigma},\hat{c}_{o\sigma'}\right]} \tag{3.2}$$

and hereafter will refer to this quantity as:

$$G_{\sigma\sigma'}(\tau) = G_{o\sigma\sigma'}(\tau) \tag{3.3}$$

In order to obtain an analytical formulation of the local effective action $\mathcal{S}_{eff}$ it is convenient to split the lattice action into three parts $\mathcal{S} = \mathcal{S}_o + \delta\mathcal{S} + \mathcal{S}^{(o)}$ which correspond, respectively, to

- The contribution of the electrons on the impurity site:

$$\mathcal{S}_o = \int_0^\beta d\tau \left[\sum_\sigma \hat{c}^{\dagger(H)}_{o\sigma}(\tau)\left(\partial_\tau - \mu\right)\hat{c}^{(H)}_{o\sigma}(\tau) + U\hat{n}_{o\uparrow}(\tau)\,\hat{n}_{o\downarrow}(\tau) \right] \tag{3.4}$$

- The connections between site "o" and rest of the lattice:

$$\delta\mathcal{S} = -\int_0^\beta d\tau \sum_{j\neq o\sigma} \left(t_{jo}\hat{c}^\dagger_{j\sigma}\hat{c}_{o\sigma} + t_{oj}\hat{c}^\dagger_{o\sigma}\hat{c}_{j\sigma} \right) \tag{3.5}$$

  this term contains only quadratic terms in a number of the order of the lattice connnectivity;

- The action of the *cavity* i.e. the one of the whole lattice without "o" and the bonds which connect it to the lattice:

$$\begin{aligned}\mathcal{S}^{(o)} \quad &= \textstyle\int_0^\beta d\tau \quad \Bigg[\sum_{i\neq o\sigma} \hat{c}^\dagger_{i\sigma}\left(\partial_\tau - \mu\right)\hat{c}_{i\sigma} + U\sum_{i\neq o}\hat{n}_{i\uparrow}\hat{n}_{i\downarrow} \\ &\qquad - \sum_{\{ij\}\neq o\sigma}\left(t_{ji}\hat{c}^\dagger_{j\sigma}\hat{c}_{i\sigma} + t_{ij}\hat{c}^\dagger_{i\sigma}\hat{c}_{j\sigma}\right)\Bigg]\end{aligned}$$

Now Eq.[3.1] can be reformulated as a quantum average of the operator $e^{-\delta\mathcal{S}}$

over the cavity ensemble:

$$\begin{aligned} e^{-\mathcal{S}_{eff}} &= \frac{\mathcal{Z}_{eff}}{\mathcal{Z}} \int \prod_{i\neq o\sigma} D\left[\hat{c}^{\dagger}_{i\sigma}, \hat{c}_{i\sigma}\right] e^{-\mathcal{S}} \\ &= \frac{\mathcal{Z}_{eff}}{\mathcal{Z}} e^{-S_o} \int \prod_{i\neq o\sigma} D\left[\hat{c}^{\dagger}_{i\sigma}, \hat{c}_{i\sigma}\right] e^{-\delta\mathcal{S}} e^{-\mathcal{S}^{(o)}} \end{aligned}$$

So as to have:

$$\mathcal{S}_{eff} = S_o - \ln\left(\left\langle e^{-\delta\mathcal{S}}\right\rangle_{(o)}\right) \tag{3.6}$$

where we neglect the normalization constant $K = -\ln\left(\frac{\mathcal{Z}_{eff}\mathcal{Z}^{(o)}}{\mathcal{Z}}\right)$. Now we shall make use of the "linked cluster theorem", which states that, given an unperturbed action $\mathcal{S}_o$ and a perturbation $\mathcal{S}_{pert} = \delta\mathcal{S}$, the logarithm of the perturbation averaged over the unperturbed ensemble can be rewritten as the sum of all connected diagrams in a perturbation expansion on $\mathcal{S}_{pert}$:

$$\begin{aligned} \mathcal{S}_{eff} &= S_o - \ln\left(\frac{\int \prod_{i,\sigma} D\left[\hat{c}^{\dagger}_{i\sigma}, \hat{c}_{i\sigma}\right] e^{-\mathcal{S}^{(o)}} e^{-\delta\mathcal{S}}}{\int \prod_{i,\sigma} D\left[\hat{c}^{\dagger}_{i\sigma}, \hat{c}_{i\sigma}\right] e^{-\mathcal{S}^{(o)}}}\right) \\ &= S_o - \ln\left(\frac{\int \prod_{i,\sigma} D\left[\hat{c}^{\dagger}_{i\sigma}, \hat{c}_{i\sigma}\right] e^{-\mathcal{S}^{(o)}} \left[\sum_{n=0}^{\infty} \int_0^{\beta} \prod_{l=1}^{n} -\frac{d\tau_l}{n!} \delta\mathcal{S}\left(\tau_l\right)\right]}{\int \prod_{i,\sigma} D\left[\hat{c}^{\dagger}_{i\sigma}, \hat{c}_{i\sigma}\right] e^{-\mathcal{S}^{(o)}}}\right) \\ &= S_o + \sum \left(\begin{array}{c} \text{all connected diagrams of a} \\ \text{perturbation expansion in } \mathcal{S}_{pert} \end{array}\right) \end{aligned}$$

Defining:

$$\begin{aligned} \eta_i\left(\tau\right) &= t_{oi}\hat{c}_{oi}\left(\tau\right) \\ \overline{\eta}_i\left(\tau\right) &= t_{oi}\hat{c}^{\dagger}_{oi}\left(\tau\right) \end{aligned}$$

one obtains:

$$\begin{aligned}\mathcal{S}_{eff} &= \mathcal{S}_o + \sum_{n=1}^{\infty} \int_0^{\beta} \sum_{\{i_1 \dots j_n\} \neq o} G^{(o)}_{i_1 \dots i_n j_1 \dots j_n} \left(\tau_1, ..., \tau_n'\right) \prod_{l=1}^{n} \overline{\eta}_{i_l}\left(\tau_l\right) \times \eta_{j_l}\left(\tau_l'\right) d\tau_l d\tau_l' \\ &= \mathcal{S}_o + \sum_{n=1}^{\infty} \int_0^{\beta} M\left(\tau_1, ..., \tau_n'\right) d\tau_l d\tau_l' \end{aligned} \tag{3.7}$$

In the last equation $M\left(\tau_1, ..., \tau_n'\right)$ is the sum of all the connected cavity Green's Functions of any order (one-particle, two-particle, . . .) weighted by an hopping amplitude t_{oi} per each fermionic operator. This expression is formally exact, but it is however of little practical use, as it contains correlators af arbitrarily high order which can hardly be computed. A huge simplification occurs in the limit of infinite dimension if the hopping is rescaled as:

$$t_{ij} = \frac{\tilde{t}}{d^{-|i-j|/2}} \tag{3.8}$$

where $|i-j|$ is the distance between the lattice site connected by t_{ij}. As we mentioned above, this condition is necessary to have a finite expectation value of the kinetic energy per site in the $d \to \infty$, a necessary condition to have non trivial physics.

We can easily see that only the first term in Eq.[3.7] survives in the infinite-coordination limit: the two point connected Green's function (single-particle Green's function), which appears in the first term of Eq.[3.7],scales like the hopping connecting the two sites[1]:

$$G_{ij\sigma}^{(o)}(\omega) \propto d^{-|i-j|/2} \tag{3.10}$$

Considering that i and j are two different neighbors of the site "o", all the non local cavity Green's function have at least $|i-j|=2$, which implies that $G_{ij\sigma}^{(o)}(\omega)$ is of the order of $1/d$. From Eq.[3.8] follows that the hopping contribution at the first order will scale as $t_{oi}t_{oj} \propto d^{-1}$. Finally, the first terms features two sums over the lattice sites which bring each one factor d. Therefore the first term, of the expansion remains of order 1. The same arguments show [31] that all higher orders are vanishing in the $d \to \infty$ limit. Any further order brings indeed two more summations over different sites, two more hoppings, and a Green's function with two more legs. Overall this gives a further $1/d$, so that all the other terms vanish in the infinite-coordination limit.

With these approximation the effective local action in the infinite coordina-

---

[1] In order to prove this result, we can express the Green's function as a Neumann series:

$$\begin{aligned} G_{ij\sigma}^{(o)}(\omega) &= \langle i\sigma| \frac{1}{\omega - \mathbf{T}} |j\sigma\rangle = \frac{1}{\omega} \langle i\sigma| \frac{1}{\mathbf{1} - \frac{1}{\omega}\mathbf{T}} |j\sigma\rangle \\ &= \frac{1}{\omega} \langle i\sigma| \sum_{n=0}^{\infty} \left(\frac{t_{ij}}{\omega}\right)^n |j\sigma\rangle = \frac{1}{\omega} \langle i\sigma| \sum_{n=0}^{\infty} \left(\frac{\tilde{t}}{\omega} \frac{1}{d^{-|i-j|/2}}\right)^n |j\sigma\rangle \end{aligned}$$

So the first order contribution scales as:

$$G_{ij\sigma}^{(o)}(\omega) \propto d^{-|i-j|/2} \tag{3.9}$$

tion limit reads:

$$\begin{aligned}\mathcal{S}_{eff} &= -\int_0^\beta d\tau d\tau' \sum_\sigma \hat{c}^\dagger_{o\sigma}(\tau)\left[\delta(\tau-\tau')(-\partial_\tau+\mu)-\sum_{ij} t_{oi}t_{oj}G^{(o)}_{ij\sigma}(\tau-\tau')\right]\hat{c}_{o\sigma}(\tau') \\ &+\int_0^\beta d\tau U\hat{n}_{o\uparrow}(\tau)\hat{n}_{o\downarrow}(\tau) \end{aligned} \tag{3.11}$$

where $G^{(o)}_{ij\sigma}(\tau-\tau')$ is the single-particle Green's function of the cavity, i.e., of the lattice substracted of the special site "o" and the bonds connecting it to the nighbors.

It is customary to define a dynamical *Weiss field*:

$$\begin{aligned}\mathcal{G}^{-1}_{o\sigma}(\tau-\tau') &= \delta(\tau-\tau')(-\partial_\tau+\mu)-\sum_{ij} t_{oi}t_{oj}G^{(o)}_{ij\sigma}(\tau-\tau') \\ &= \delta(\tau-\tau')(-\partial_\tau+\mu)-\Gamma_{o\sigma}(\tau-\tau')\end{aligned}$$

which plays the role of a non interacting Green's function of the effective local theory, but it has not to be confused with the local component of the non-interacting lattice Green's function. In order to proceed in the derivation is useful to Fourier transform from the imaginary-time representation to the Matsubara imaginary-frequency domain:

$$\mathcal{S}_{eff} = -\sum_{\sigma n}\hat{c}^\dagger_{o\sigma n}\mathcal{G}^{-1}_{o\sigma}(i\omega_n)\hat{c}_{o\sigma n}+U\hat{n}_{o\uparrow}\hat{n}_{o\downarrow}$$

with:

$$\mathcal{G}^{-1}_o(i\omega_n) = i\omega_n+\mu-\Gamma_o(i\omega_n) \tag{3.12}$$

where

$$\Gamma_o\left(i\omega_n\right)=\sum_{ij}t_{oi}t_{oj}G^{(o)}_{ij\sigma}\left(i\omega_n\right) \tag{3.13}$$

It can be proved [31, 51] that, for any lattice with one site removed one can directly connect the cavity Green's function with a combination of exact lattice Green's functions so that

$$\Gamma_o\left(i\omega_n\right) \;=\; \sum_{ij}t_{oi}t_{oj}G_{ij}\left(i\omega_n\right)-\frac{\sum_i t^2_{oi}G^2_{io}\left(i\omega_n\right)}{G_o\left(i\omega_n\right)}.$$

This equations is an important step ahead because it only contains Green's function of the full lattice model, and the unphysical cavity quantities have disappeared. Finally the above summations can be turned into integrals, which can all be expressed in terms of the local Green's function of the lattice model. Introducing the self-energy of the local effective theory

$$\Sigma\left(i\omega_n\right)=\mathcal{G}^{-1}_{o\sigma}\left(i\omega_n\right)-G^{-1}\left(i\omega_n\right) \tag{3.14}$$

one finally gets:

$$\mathcal{G}^{-1}_o\left(i\omega_n\right)=\Sigma\left(i\omega_n\right)+\left[\tilde{D}\left(i\omega_n+\mu-\Sigma\left(i\omega_n\right)\right)\right]^{-1} \tag{3.15}$$

being $\tilde{D}$ the Hilbert transform over the non interacting density of states. This is an equation which allows to compute the Weiss field $\mathcal{G}^{-1}_o\left(i\omega_n\right)$ through the knowledge of the self-energy. This equation plays the role of a self-consistency condition connecting two quantities defined within the effective local theory. In the next paragraph we will briefly comment about the solution of the self-consistent equation.

We conclude this section by giving a more transparent and insightful form to the self-consistency condition.

$$G\left(i\omega_n\right) = \sum_k \frac{1}{i\omega_n + \mu - \varepsilon_k - \Sigma\left(i\omega_n\right)} \tag{3.16}$$

where ε_k is the bare dispersion of the model. This formulation implies that the Green's function of the effective theory coincides with the local component of the lattice Green's function once the lattice self-energy is replaced by the momentum-independent self-energy of the effective theory. Hence we have shown that an exact solution of the Hubbard model in the infinite-coordination limit yields a quantum version of a mean-field theory, in which a lattice model is mapped onto an effective single-site theory subject to a self-consistency condition ensuring that the local component of the Green's function coincides with that of the site we chose to construct the effective theory, which is indeed equivalent to any other.

3.2 Solution of the DMFT. Exact Diagonalization

We have demonstrated that in the infinite-coordination limit we can build an exact effective action for a single lattice site. The effective action contains a Weiss field which depends on frequency and it can be computed self-consistently through the knowledge of the Green's function (or the self-energy) of the effective theory.

Therefore a solution of the DMFT can be obtained by means of an iterative procedure. We start solving an effective local theory for some initial Weiss field $\mathcal{G}^{-1}_{o\sigma}$ and we compute the Green's function and the self-energy corresponding to che chosen Weiss field. Then the self-consistency condition Eq.[3.16] is used to compute a new value of the Weiss field. The procedure is then repeated until the Weiss field and the Green's function do not change in the iterations and we have found a self-consistent set of variables. While the self-consistency condition is a trivial algebraic equation in the frequency domain, the solution of the effective local theory is a non-trivial step, due to the interacting nature of the effective theory, which still contains a local interaction term. Therefore, despite the huge simplification with respect to the original lattice model, the effective theory requires some numerical solution. The most popular numerically exact solvers are Numerical Renormalization Group, Continuous-Time Quantum Montecarlo and [36] Exact Diagonalization (ED), [14, 19] which is the method we employ in the present thesis. Besides the manageable computational cost, one advantage of ED solver is that the $T = 0$ spectrum can be directly obtained on real frequency axis. On the other hand, the exponential growth of the Hilbert space impose severe limitation to the number of orbitals to be considered in the bath parametrization. It is important to underline that the parameterizaton of the effective bath in a discrete number of orbitals has no relation with the finite size of the real lattice, as well as the Weiss field correspond only to the non interacting Green's function of the impurity model but not to the local projection of the non interacting lattice Green's function (to be correct they are equal only in the $U = 0$ case).

The ED solution requires to represent the local effective theory in terms of a Hamiltonian representation, in which the dynamical Weiss field is represented in terms of set of auxiliary non-interacting fermions hybridized with the interacting site. The Hamiltonian we described is nothing but an Anderson impurity model, which has been introduced long before the developement of DMFT to study the effect of interacting impurities in metallic hosts.

We start by showing a general representation of a multi-orbital Hubbard model. The effective impurity model can be written as

$$\begin{aligned}\mathcal{H}_{AIM} &= \sum_{\alpha,\beta}\sum_{\sigma,\bar{\sigma}} \hat{d}^{\dagger}_{\alpha\sigma}\hat{\mathcal{H}}^{loc}\hat{d}_{\beta\bar{\sigma}} + \hat{\mathcal{H}}^{int} \\ &+ \sum_{\alpha,\beta}\sum_{\sigma,\bar{\sigma}}\sum_{k,k'=1}^{N_b} \hat{c}^{\dagger}_{\alpha\sigma k}\hat{\mathcal{H}}^{bath}_{kk'}\hat{c}_{\beta\bar{\sigma}k'} \\ &+ \sum_{\alpha,\beta}\sum_{\sigma,\bar{\sigma}}\sum_{k=1}^{N_b}\left(\hat{V}_{kk'}\hat{c}^{\dagger}_{\alpha\sigma k}\hat{d}_{\beta\bar{\sigma}} + \hat{V}^{*}_{kk'}\hat{d}^{\dagger}_{\alpha\sigma}\hat{c}_{\beta\bar{\sigma}k}\right)\end{aligned} \tag{3.17}$$

where $\{\alpha,\beta\}$ and $\{\sigma,\bar{\sigma}\}$ are the orbital and spin index , while k is the effective bath index. $\hat{c}_o(\hat{c}^{\dagger}_o)$ and $\hat{c}_k(\hat{c}^{\dagger}_k)$ represent the destruction (creation) operator in acting on the impurity "o" and on k-th, form 1 to N_b, bath site respectively. This formulation encloses all the possible connection geometries of the AIM depending on the choice of the various contribution:

- $\hat{\mathcal{H}}^{loc} = \mathcal{H}^{loc}_{\alpha\beta\sigma\bar{\sigma}}$ is the non interacting local Hamiltonian of the correlated impurity site. This Hamiltonian capture the real non interacting physics of the model under investigation:

$$\mathcal{H}^{loc}_{\alpha\beta\sigma\bar{\sigma}} = \sum_{\mathbf{k}} \mathcal{H}^{loc}_{\alpha\beta\sigma\bar{\sigma}}(\mathbf{k}) \tag{3.18}$$

- $\hat{\mathcal{H}}^{int}$ is the rotational invariant Kanamori interaction term of Eq.[2.6]. For the single-band model this reduces to the standard density-density interaction $U\hat{n}_{o\uparrow}\hat{n}_{o\downarrow}$.
- $\hat{\mathcal{H}}^{bath}_{kk'} = \mathcal{H}^{bath}_{\alpha\beta\sigma\bar{\sigma}kk'}$ is the Hamiltonian of the bath. This quantity is self consistently determined as well as the following term
- $\hat{V}_{kk'} = V_{\alpha\beta\sigma\bar{\sigma}kk'}$ is the hopping connecting the bath Hamiltonian to the impurity site.

There is a substantial level of arbitrariness in the specific topology of the AIM, i.e. in the matrix representation of $\hat{\mathcal{H}}^{bath}_{kk'}$ and $\hat{V}_{kk'}$, hence the choice can be tailored on the physical properties under investigation. In the following we discuss the optimal choices to address the electron-phonon and spin-orbit couplings.

For the single-band Hubbard model we can use, without loss of generality, a diagonal representation of the effective bath, $\hat{\mathcal{H}}^{bath}_{kk'} = \varepsilon_k \delta_{kk'}$, and the corresponding hoppings $\hat{V}_{kk'} = V_k \delta_{kk'}$.

The few steps of a standard DMFT loop will be briefly described in this simple case. The other extensions, suited for example for multiorbital computations, can be straightforwardly derived. Thus the impurity Hamiltonian of Eq.[3.17] reduces to:

$$\mathcal{H}_{AIM} = -\mu\left(\hat{n}_{o\uparrow} + \hat{n}_{o\downarrow}\right) + U\hat{n}_{o\uparrow}\hat{n}_{o\downarrow} + \sum_{k\sigma}^{N_b} \varepsilon_k \hat{c}^{\dagger}_{\sigma k}\hat{c}_{\sigma k} + \sum_{k\sigma}^{N_b} V_k \left(\hat{c}^{\dagger}_{\sigma k}\hat{d}_{\sigma} + \hat{d}^{\dagger}_{\sigma}\hat{c}_{\sigma k}\right) \tag{3.19}$$

All the information regarding the effective bath is encoded in the hybridization function, written in terms of the anderson parameters ε_k and V_k, representing respectively the onsite energy of the bath level and it's connection to the impurity site. It worth mentioning that the strict self-consistency can only be obtained with a continuous bath of states. The approximation the exact diagonalization solver is the parametrization of hybridization function in terms of a discrete number of poles N_b, which will be cast into a minimization problem in the Anderson parameters. The maximum size of the truncated Hilbert is $n_{tot} = 2^{2n_s}$ where $n_s = N_b + 1$ is on the total number of sites considered in the model. As previously mentioned, the most severe limitations in the ED method is the exponential growth of the number of states with the number of bath levels considered. Simplifications in the diagonalization procedures comes form the symmetry properties of the considered Hamiltonian. In the simplest case the repulsive single band Anderson impurity Hamiltonian commutes with the total spin $\hat{N}_\sigma = \sum_i^{n_s} \hat{n}_{i\sigma}$ operators, indeed it can be decomposed in smaller $\hat{N}_\uparrow$, $\hat{N}_\downarrow$ conserving blocks.

The formal expression of Γ can be trivially obtained by integrating the bath degrees of freedom, i.e., all the indexes different form "o". The expression for the hybridization function in this simple case reads:

$$\Gamma_o\left(i\omega_n\right) = \sum_k \frac{\left|V_k\right|^2}{i\omega_n - \varepsilon_k} \tag{3.20}$$

With a given set of Anderson parameters and interaction strength U, the impurity Hamiltonian is written in a tridiagonal representation through the Lanczos algorithm ad readily diagonalized. Once obtained the groundstate energy E_o and the corresponding eigenvector $|\Psi_o\rangle$, the impurity interacting Green's function is computed in terms of the Kallen-Lehmann formula[2]:

$$G_o^{imp}\left(i\omega_n\right) = \sum_m \sum_j \frac{\left|\langle j|\,\hat{c}_o\left|\Psi_o^{(m)}\right\rangle\right|^2}{i\omega_n - \left(E_j - E_o^{(m)}\right)} \tag{3.22}$$

Where $|j\rangle$ ans E_j represent respectively all the Fock states connected with the groundstate by the destruction operator and the corresponding excitation energy. The latter are again computed with the Lanczos algorithm. In Eq.[3.22] m is the index of the degenerate groundstates.

Then we use the impurity Green's function to compute the exact self-energy of the impurity model

$$\Sigma\left(i\omega_n\right) = \mathcal{G}_o^{-1}\left(i\omega_n\right) - G_o^{imp-1}\left(i\omega_n\right), \tag{3.23}$$

from which we compute the local component of lattice Green's function

$$G_o^{loc}\left(i\omega_n\right) = \sum_{\mathbf{k}} G_o\left(\mathbf{k}, i\omega_n\right) = \sum_{\mathbf{k}} \frac{1}{i\omega_n + \mu - \varepsilon_{\mathbf{k}} - \Sigma\left(i\omega_n\right)} \tag{3.24}$$

which is used to obtain a new Weiss field through the self-consistency condition.

$$\mathcal{G}_o^{new-1}\left(i\omega_n\right) = \Sigma_o\left(i\omega_n\right) + G_o^{loc-1}\left(i\omega_n\right) \tag{3.25}$$

---

[2] The reported equation holds for $T = 0$ calculations, however, in the spirit of the Lanczos, it can be generalized to the $T > 0$ case. Taking into account not only the groundstate $|\Psi_o\rangle$ but also a finite set of, say N_e, excited states $|\Psi_i\rangle$ one gets:

$$G_o\left(T, i\omega_n\right) = \frac{1}{\sum_i^{N_e} e^{-\beta E_i}} \sum_i^{N_e} \sum_j \frac{\left|\langle j|\,\hat{c}_o^\dagger\,|\Psi_i\rangle\right|^2 \left(e^{-\beta E_i} + e^{-\beta E_j}\right)}{i\omega_n - \left(E_j - E_i\right)} \tag{3.21}$$

where $\beta = {}^1\!/_T$

The latter will be used as an input for the minimization procedure aimed to obtain a new set of Anderson parameters. This closes the DMFT loop, that will be perpetrate until convergence of two subsequent solutions $\mathcal{G}_o$ and $\mathcal{G}_o^{new}$ under a given threshold.

3.3 Phase diagram of the single band Hubbard model with DMFT

In the following, we briefly review the key features of the electronic phases of the Hubbard model captured by DMFT. The phenomenology is summarized in the framework of the single band Hubbard model at half-filling in the bethe lattice[31].

3.3.1 The Fermi liquid regime

The Fermi liquid at $T = 0$ is a correlated metal with strongly renormalized, but still coherent, quasiparticle excitations, peculiar of the single band Hubbard model for any value of the interaction as long as $U < U_c$. Within this regime both the real and imaginary part of the self-energy have a well defined frequency behavior:

$$\begin{aligned}\Re\Sigma_o\left(\omega\right) &= \frac{U}{2} + \left(1 - z_{qp}\right)\omega + \mathcal{O}\left(\omega^3\right) \\ \Im\Sigma_o\left(\omega\right) &= -B\omega^2 + \mathcal{O}\left(\omega^4\right)\end{aligned}$$

being z_{qp} the inverse of the effective mass renormalization m^*/m or, equivalentely, the band renormalization factor at the Fermi energy $\varepsilon_F^* = z_{qp}D$. This quantity to some extent measure the level of correlations of the metallic state, whish is the only solution for the single-band Hubbard model for $U < U_c$. z_{qp} can be experimentally probed by means, for example, of the optical conductivity Drude weight. In addition it sets the temperature threshold T^* above which the quasiparticle excitations lose their coherence acquiring a finite lifetime. The effect of interactions on the metallic state can be directly understood in terms of the local spectral function:

$$A(\omega) = -\frac{1}{\pi}\Im\left\{G(\omega + i\delta)\right\} \tag{3.26}$$

which in the Fermi liquid phase displays two high energy bands, accounting for the incoherent excitatioins centered on $\pm U/2$, and a sharp quasiparticle peak pinned to the Fermi level. The latter has a reduced bandwidth proportional to the quasiparticle weight itself $z_{qp} < 1$, that, as we said, can be interpreted as the coherence-scale for the quasi-particles. The missing $1 - z_{qp}$ spectral weight at the Ferm energy is transferred to the high energy bands. The Luttinger-Ward theorem states that the value $A(\omega = 0)$ is pinned to the non-interacting value, which means that the correlations do not modify the Fermi surface. In the $T > 0$ case a finite incoherent scattering term is present even at the Fermi level, resulting in a non vanishing self-energy imaginary part at $\omega = 0$. If this condition occurs in the $T = 0$ case the system violates the Luttinger-Ward therorem resulting in the so called non-Fermi liquid phase.

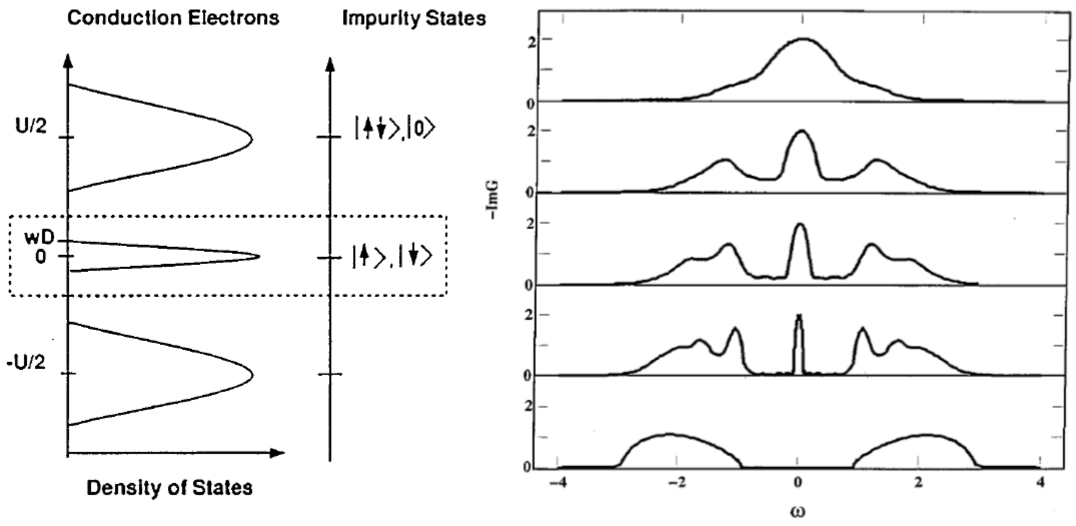

Figure 3.1: Schematic plot of the conduction bath spectral function and impurity orbital configurations, illustrating the separation of energy scales at half-filling, close to the Mott transition and spectral density $A(\omega)$, for increasing values of U/D. The first four curves correspond to an increasingly correlated metal, while the bottom one is an insulator.

3.3.2 The Mott Insulator

In the strong coupling regime the system becomes a gapped Mott Insulator. At half-filling the real part of the self-energy is an anti-symmetric, hence vanishing, function, therefore, in order to have a vanishing spectral function at the Fermi level, the Imaginary part of the self-energy is diverging. The insulating phase is characterized by unscreened local moments ordered into an antiferromagnetic phase. Upon heating, thermal fluctuations tends to fill the gap and eliminate the divergence in the imaginary part of the self-energy that reaches a finite value at $\omega = 0$.

3.3.3 Antiferromagnetism

The solution for the Hubbard model in 3D is an antiferromagnet (AFM) for any finite value of U. The Landau order parameter of this transition is the staggered mangnetization m and it's associated to a gap in the single particle spectrum of the system.

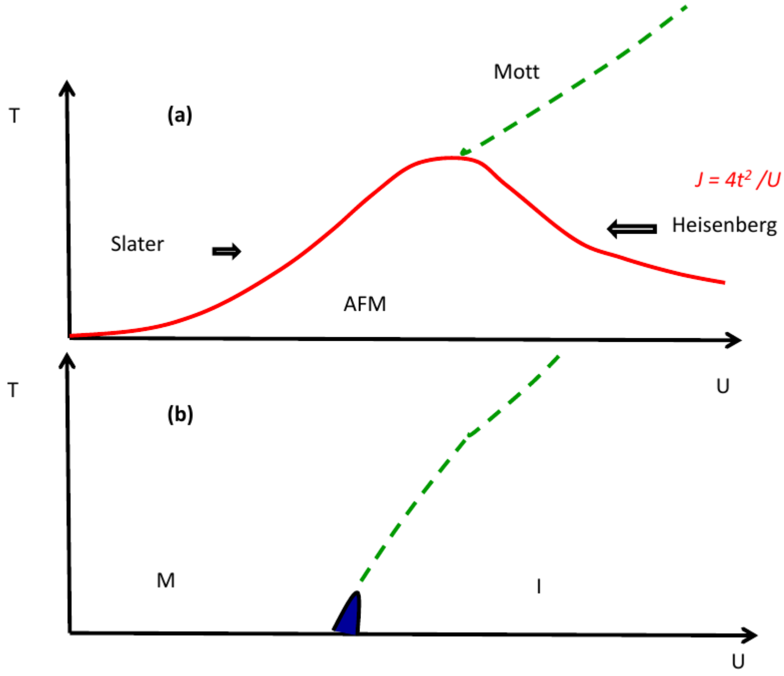

Figure 3.2: Schematic phase diagram of the 3d Hubbard model in the temperature T interaction U plane for perfect nesting. (a) The solid red line is the N´eel temperature T N below which the system is antiferromagnetic. Coming from the left, it is a metallic state that becomes un- stable to antiferromagnetism by the Slater mechanism. Coming from the right, it is a gapped insulator with local moments described by the Heisenberg model that becomes unstable to antiferromagnetism. The dashed green line above the maximum T N indicates a crossover from a metallic state with a Fermi surface to a gapped state with local moments. That crossover can be understood in (b) where antiferromagnetism is prevented from occurring. There dynamical mean-field theory predicts a first-order phase transition between a metal and a Mott insulator, with a coexistence region indicated in blue.

The fact that the normal state, i.e. above T_c, is different wether approaching the transition from the weak or strong coupling side is a consequence of the crossover transition. The sistem goes from an itinerant Slater antiferromagnet phase to a gapped phase, ascribable to an Heisenbeg model, increasing the ratio U/D. While the $0 < T < T_c$ metal-insulator thermodinamic transition is second order, the quantum $T = 0$ transition is overscreend by the fact that, as we said, AFM is the groundstate for any value of U. The DMFT approach overcomes this limitation since it's possible to suppress the AFM solution simply imposing that $G_{\uparrow}^{imp} = G_{\downarrow}^{imp}$. With this symmetry, exception given for a small coexistence region, the groundstate of the Hubbard model is a paramagnetic metal, separated from a paramagnetic Mott insulator by a first order transition that occurs at $U_c \sim 2.5W$. In this sense the $T = 0$ Mott transition is a precursor of the crossover between the metallic and insulating phases. The coexistence region of the $T = 0$, DMFT solution of the Hubbard model extends from the value $U_{c_1} \sim 2.5D$, above which the mean-field insulating solution begins to appear with the opening of the Mott gap, to $U_{c_2} \sim 3D$ where the paramagnetic metal dies by means of a second order vanishing quasiparticle weight. U_{c_1} and U_{c_2} extend at finite temperature into a critical point, above which the phase transition is continuous.

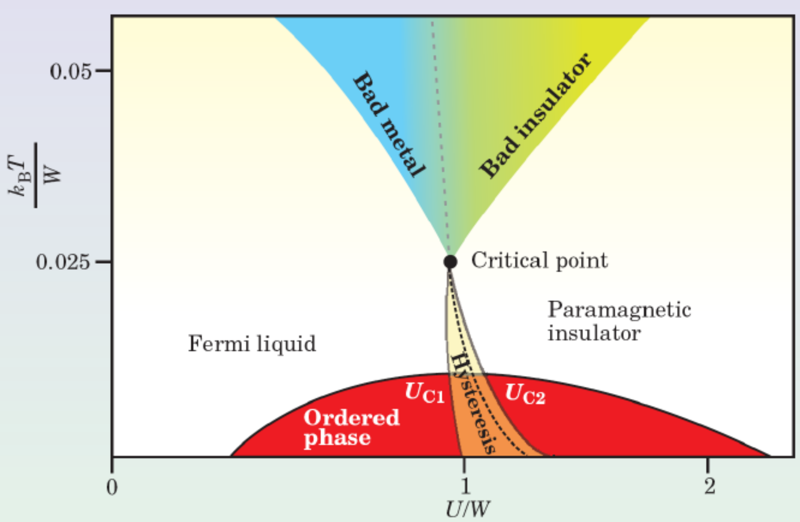

Figure 3.3: Phase diagram in the U–T plane. At low temperatures, two critical lines $U_{c_1}(T)$ and $U_{c_2}(T)$ individuate the coexistence region. The two lines converge at a finite-temperature critical point.

3.4 Electron-Phonon coupling in DMFT

In the Hubbard-Holstein model a single harmonic oscillator is attached to each site of the original lattice. In the spirit of DMFT this term can be viewed as an additional interaction term acting on the impurity, hence it can be taken into account exactly. The electron-phonon coupling on the impurity reads:

$$\hat{\mathcal{H}}^{e-ph} = -g\sum_{\sigma}\left(\hat{n}_{o\sigma} - {}^{1}\!/_{2}\right)\left(\hat{b} + \hat{b}^{\dagger}\right) + \omega_o \hat{b}^{\dagger}\hat{b} \tag{3.27}$$

The most pervasive extension of the ED approach to DMFT will be in the Hilbert space, that has to be expanded over a set of bosonic degrees of freedom onto which the phononic operators $\hat{b}$ and $\hat{b}^{\dagger}$ are going to act. This expansion take the form of a simple external product:

$$|\Psi_{el}, n_{ph}\rangle = |\Psi_{el}\rangle \otimes |n_{ph}\rangle \tag{3.28}$$

In practice, for each electronic Fock state a complete bosonic subspace will be attached. It is important to underline that this is just how we expanded the Hilbert space, not that the groundstate is factorizable between the two subspaces. As a matter of fact in our calculations the electronic and phononic contribution to $|\Psi_o\rangle$ are not disentagled at all. Clearly the number of phonon has not an upper bound, thus also this additional subspace has to be truncated allowing for a maximum number of excited phonons N_{ph}. This value has to be chosen wisely in the adiabatic regime and in strong coupling, where phonon excitations are energetically convenient. For all the result presented in the Thesis we choose $N_{ph} = 8$. The only other minor change is in the evaluation of the impurity Green's function: Eq.[3.22] still holds and the impurity operator will act just on a wider number of states, namely $N_{el} \times (N_{ph} + 1)$. The ED method intrinsically offers the advantage of a direct evaluation of the real frequency electron and phonon spectral functions, as well as phononic observables. Regarding the choice of the maximum number of phonons, the excitation probability distribution $P\left(n_{ph}\right)$ over the electron-phonon groundstate $|\Psi_o, N_{ph}\rangle$ has been computed. This quantity has a peak on the average number of phonons excited for a given set of interaction parameters:

$$P\left(n_{ph}\right) = \langle \Psi_o, N_{ph}|\, \hat{b}^{\dagger}\hat{b}\, |\Psi_o, N_{ph}\rangle \tag{3.29}$$

A key quantity in order to tackle the problem of the polaron crossover, is the phonon displacement probability distribution:

$$\begin{aligned} P\left(X\right) &= \left\langle \Psi_o, N_{ph} \middle| X \right\rangle \left\langle X \middle| \Psi_o, N_{ph} \right\rangle \\ &= \sum_{i_{ph}, j_{ph}}^{N_{ph}} \left\langle \Psi_o, i_{ph} \right| \psi_{i_{ph}}\left(x\right) \psi_{j_{ph}}\left(x\right) \left| \Psi_o, j_{ph} \right\rangle \end{aligned}$$

where $\psi_{i_{ph}}\left(x\right)$ is the Hermite polynom related to the i-th excited phononic level. As we mentioned in the previous chapter, this quantiy ha been used to locate the position of the crossover through the bimodality criterion.

3.5 Superconductivity in DMFT

The ED procedure can be easily extended in order to capture the superconducting phase by means of the anomalous Green's function:

$$F\left(\mathbf{k}, \tau\right) = -\left\langle \mathrm{T}_\tau \left[\hat{c}_{\mathbf{k}\uparrow}\left(\tau\right) \hat{c}_{\mathbf{k}\downarrow}\left(0\right)\right]\right\rangle \tag{3.30}$$

the local nature of the DMFT approach permits only singlet pairings, for which $\hat{S} = 0$, $\hat{S}_z = 0$ and for the $\hat{S}_z = 0$ subspace of a triplet $\hat{S} = 1$ pairing. This limitation is reflected in two symmetry conditions for F:

$$\begin{aligned} F\left(-\mathbf{k}, -\tau\right) &= F\left(\mathbf{k}, \tau\right) \\ F\left(-\mathbf{k}, -\tau\right) &= -F\left(\mathbf{k}, \tau\right) \end{aligned}$$

that allows for a purely real F. The above mentioned DMFT equations have to be reformulated in terms of Nambu spinors $\hat{\Psi}_{\mathbf{k}}^{\dagger} = \left(\hat{c}_{\mathbf{k}\uparrow}^{\dagger}\hat{c}_{-\mathbf{k}\downarrow}\right)$ in order to define a local Green's function as:

$$\begin{aligned}\hat{G}_{loc}\left(i\omega_n\right) &= \sum_{\mathbf{k}} -\left\langle \mathrm{T}\left[\mathbf{\Psi}_{\mathbf{k}n}\mathbf{\Psi}_{\mathbf{k}n}^{\dagger}\right]\right\rangle \\ &= \begin{pmatrix} G_{loc}\left(i\omega_n\right) & F_{loc}\left(i\omega_n\right) \\ F_{loc}\left(i\omega_n\right) & -G_{loc}^{*}\left(i\omega_n\right)\end{pmatrix}\end{aligned}$$

Due to the presence of an anomalous component, the whole impurity problem is now expressed in a 2×2 matrix formulation: the local self-energy as well as the Weiss field will acquire an extra off-diagonal component, so the self consistency equation simply become:

$$\hat{\mathcal{G}}_{o}^{-1}\left(i\omega_n\right) = \hat{G}_{loc}^{-1}\left(i\omega_n\right) + \hat{\Sigma}\left(i\omega_n\right) \tag{3.31}$$

From the technical point of view, the superconducting phase can be introduced in the AIM in two ways: allowing for a pairing term between an electron on the impurity and one electron in the bath, or, alternatively including a pairing field between the electrons belonging to the bath. We chose to use this second approach since it corresponds to a Weiss field in which a single Anderson parameter controls the SC phase owing a better accuracy in the minimization procedure. The Hamiltonian pairing term to be added to Eq.[3.19] is:

$$\mathcal{H}_{SC} = \sum_{k}^{N_b} \Delta_k \left(\hat{c}_{\uparrow k}^{\dagger}\hat{c}_{\downarrow k}^{\dagger} + \hat{c}_{\downarrow k}\hat{c}_{\uparrow k}\right) \tag{3.32}$$

Due to this coupling term, the Anderson Hamiltonian do not commute anymore with $\hat{N}_{\uparrow}$ and $\hat{N}_{\downarrow}$. Now the conserved quantity is the total z-projection of the spin operator $\hat{S}_z = \hat{N}_{\uparrow} - \hat{N}_{\downarrow}$, resulting in a bigger dimension of the Hamiltonian blocks. The last equation needed to close again the DMFT loop is the matrix formulation of the Weiss field:

$$\hat{\mathcal{G}}_o^{-1}\left(i\omega_n\right) = \mathbf{1}\left(i\omega_n + \mu\right) - \frac{V_k^2}{\left(i\omega_n - \varepsilon_k\right)\left(i\omega_n + \varepsilon_k\right) - \Delta_k^2}\begin{pmatrix} i\omega_n + \varepsilon_k & -\Delta_k \\ -\Delta_k & i\omega_n - \varepsilon_k \end{pmatrix} \tag{3.33}$$

3.6 Spin Orbit Coupling in DMFT

In the present thesis we address the effect of Spin-Orbit Coupling (SOC) in strongly correlated electron systems, focusing on three-fold degenerate t_{2g} orbitals. As mentioned above, spin and orbital degrees of freedom are known to be coupled in heavy d compounds because of the large atomic number. In this work we have mainly focused on the effect of an atomic spin-orbit coupling in a simple-model framework, but we also presented some results for a bulk solid of Sr_2IrO_4. In this section we briefly described our implementation of the SOC within DMFT. Clearly the multi-orbital nature of the system cannot be neglected, but the diagonal bath representation used so far is not correct anymore. In order to properly study the local SOC hamiltonian of Eq.[2.41] we are going to use a different approach that goes under the name of *impurity replica*. The underlying idea is to reproduce in the bath hamiltonian $\mathcal{H}^{bath}_{\alpha\beta\sigma\bar{\sigma}kk'}$ the full spin and orbital structure of the local Hamiltonian $\mathcal{H}^{loc}_{\alpha\beta\sigma\bar{\sigma}}$. With this purpose the Anderson impurity Hamiltonian is very similar to the one of Eq. 3.17 with a diagonal representation of the hopping term between the impurity and the replica.

$$\hat{V}_{\alpha\beta\sigma\bar{\sigma}kk'} = V_k \delta_{\alpha\beta} \delta_{\sigma\bar{\sigma}} \tag{3.34}$$

Upon the integration of the non local fermionic degrees of freedom one gets the following hybridization matrix:

$$\Gamma_{\alpha\beta\sigma\bar{\sigma}} \left(i\omega_n \right) = \sum_k \left| V_k \right|^2 \left[i\omega_n - \mathcal{H}^{bath}_{\alpha\beta\sigma\bar{\sigma}kk'} \right]^{-1} \tag{3.35}$$

The only other extension of the DMFT method with respect to what we described in the previous sections is the computation of the off-diagonal components of the impurity Green's function connecting different orbitals and spins$G_{\alpha\beta\sigma\bar{\sigma}} \left(i\omega_n \right)$. This is not completely straightforward because the Lanczos algorithm, used to extract the poles in the Kallen-Lehmann spectral representation, can construct only diagonal spectral representations of Hemitian operators of the form:

$$\sum_j \frac{\langle \Psi | \hat{O}^\dagger | j \rangle \langle j | \hat{O} | \Psi \rangle}{i\omega_n - \Delta E_j} \tag{3.36}$$

This allows to obtain directly any diagonal Green's function, but for the off-diagonal components we had to engineer the all the possible linear combination in the spin-orbital indexes and build the Green's functions $\tilde{G}$ generated by the following operators so as to have the following auxiliary:

$$
\begin{aligned}
\tilde{G}_1 &\Rightarrow \hat{O} = \hat{c}^{\dagger}_{\alpha\sigma o} + \hat{c}^{\dagger}_{\beta\bar{\sigma}o} \\
\tilde{G}_2 &\Rightarrow \hat{O} = \hat{c}_{\alpha\sigma o} - \hat{c}_{\beta\bar{\sigma}o} \\
\tilde{G}_3 &\Rightarrow \hat{O} = \hat{c}^{\dagger}_{\alpha\sigma o} + i\hat{c}^{\dagger}_{\beta\bar{\sigma}o} \\
\tilde{G}_4 &\Rightarrow \hat{O} = \hat{c}^{\dagger}_{\alpha\sigma o} - i\hat{c}_{\beta\bar{\sigma}o}
\end{aligned}
$$

then the off-diagonal Green's function will be given by:

$$G_{\alpha\beta\sigma\bar{\sigma}} = \frac{1}{2}\left[\left(\tilde{G}_1 + \tilde{G}_2\right) + i\left(\tilde{G}_3 + \tilde{G}_4\right) - (1+i)\left(G_{\alpha\sigma} + G_{\beta\bar{\sigma}}\right)\right] \tag{3.37}$$

With this method, one can take into account any kind local Hamiltonian, given as input, including those containing the local projection of the SOC.

CHAPTER

4

INHOMOGENEOUS DYNAMICAL MEAN FIELD THEORY

In this Chapter we present a general approach to treat layered materials and superconductors within the framework of Dynamical Mean-Field Theory. In order to allow for different physical properties in different layers, a necessary condition to study the effect of interfaces and heterostructures, we have to abandon one of the assumption of DMFT, namely the equivalence between all the lattice sites. A general strategy to extend the DMFT approach to inhomogenous systems has been introduced independently by several authors [40, 78, 82] and it has been given different names. The fundamental idea is to map a lattice model with geometrically or electronically inequivalent sites in a *collection* of correlated impurities connected through a self-consistency condition. As will be described in the following, non-local self-energies are still assumed to vanish, but different local self-energies can be obtained corresponding to different spatial position of the system. Depending whether the translational symmetry is fully broken or partially preserved along some direction, different real-space distribution of the effective impurity problem can be designed. These kinds of non-uniform DMFT schemes allow to study broken-symmetry states with a given spatial arrangement of charge and/or spin.

4.1 Derivation of the Inhomogeneous DMFT Equations

For the specific target of this thesis, namely the investigation of correlated layered materials, the translational symmetry is broken only in the direction longitudinal to the heterostructure. Hence we will define one impurity model for every inequivalent layer, while translational invariance is enforced within each layer. For systems with fully broken translational symmetry, such as lattices in optical traps, the method can be pushed even further allowing for an impurity problem for each lattice site.

We will briefly describe the key steps to obtain inhomogeneous DMFT equations following Ref.[58, 57]. First we note that the effective local action has the same form of Eq.[3.11] as it does not depend on the lattice structure besides the information hidden in the Weiss field

$$\begin{aligned}\mathcal{S}_{i,eff} &= -\int_0^\beta d\tau d\tau' \sum_\sigma \hat{c}^\dagger_{i\sigma}(\tau)\,\mathcal{G}^{-1}_{i\sigma}(\tau-\tau')\,\hat{c}_{i\sigma}(\tau') + \int_0^\beta d\tau U_i \hat{n}_{i\uparrow}(\tau)\,\hat{n}_{i\downarrow}(\tau) \\ \mathcal{G}^{-1}_{i\sigma}(\tau-\tau') &= \delta(\tau-\tau')(-\partial_\tau+\mu) - \Gamma_{i\sigma}(\tau)\end{aligned}$$

with $\Gamma_{i\sigma}(\tau) = \sum_{jk} t_{ik} t_{ji} G^{(o)}_{jk\sigma}(\tau-\tau')$. However the self-consistency equation has to be generalized to account for a non-uniform local self-energy.

Motivated by the symmetry of the specific problem we are dealing with, we choose to work in a mixed representation where the longitudinal dependency is made clear. The 3D simple cubic lattice (sc) is considered to be built up by two-dimensional layers along the (001) direction. Accordingly, the position vector to a particular site is written as $\mathbf{R}_i = m\mathbf{d} + \mathbf{R}_{i_m}$. Here $\mathbf{R}_{i_m}$ stands for the coordinate within in the layer while m is the layer index, so that[1]:

$$|\mathbf{R}_i\rangle = \hat{c}^\dagger_i\,|0\rangle = \hat{c}^\dagger_m \hat{c}^\dagger_{i_m}\,|0\rangle = |m, \mathbf{R}_{i_m}\rangle \tag{4.1}$$

We shift in a diagonal formulation with respect of the planar wavevector $\mathbf{k}_\parallel$ through the unitary rotation:

$$\hat{c}^\dagger_{m,\mathbf{k}_\parallel} = \frac{1}{\sqrt{N_\parallel}} \sum_{i_m} \hat{c}^\dagger_{i_m} e^{i\mathbf{k}_\parallel \mathbf{R}_{i_m}}$$

Note that the fully translational invariant representation is recovered consider-

---

[1] From now on we will drop the spin index, and use only the letter "m" to explicitly indicate the plane index in a layer geometry

ing:

$$\hat{c}_{\mathbf{k}}^{\dagger} = \frac{1}{\sqrt{N_{\perp}}}\sum_{m}\hat{c}_{m,\mathbf{k}_{\|}}^{\dagger}e^{i\mathbf{k}_{\perp}m\mathbf{d}}$$

Under these considerations the single band inhomogeneous Hubbard Hamiltonian becomes:

$$\mathcal{H} = \sum_{m\mathbf{k}_{\|}}\varepsilon_{m,\mathbf{k}_{\|}}\hat{c}_{m,\mathbf{k}_{\|}}^{\dagger}\hat{c}_{m,\mathbf{k}_{\|}} - \sum_{ml\sigma}t_{ml}\left(\hat{c}_{m\sigma}^{\dagger}\hat{c}_{l\sigma}+h.c.\right) + \sum_{m\sigma}\left(\mu-\epsilon_{m}\right)\hat{n}_{l\sigma} + \sum_{m\sigma}U_{m}\hat{n}_{m\uparrow}\hat{n}_{m\downarrow} \tag{4.2}$$

to which corresponds the following local interacting Green's function:

$$\hat{G}^{loc}\left(i\omega_{n}\right) = \sum_{\mathbf{k}_{\|}}\left[\left(i\omega_{n}+\mu-\hat{\varepsilon}_{\mathbf{k}_{\|}}\right)\mathbf{1}-\hat{T}-\hat{V}-\hat{\Sigma}\left(i\omega_{n}\right)\right]^{-1} \tag{4.3}$$

where we defined:

- the fully off-diagonal matrix $\hat{T}$ representing the hopping between the planes so that: $\langle m|\,\hat{T}\,|l\rangle = -t_{ml}^{z} = -t_{ml}^{\perp}$
- the fully diagonal matrix $\hat{V}$ representing the local energy of each plane so that: $\langle m|\,\hat{V}\,|l\rangle = \epsilon_{m}\delta_{ml}$
- the fully diagonal matrix $\hat{\varepsilon}_{\mathbf{k}_{\|}}$ representing the bidimensional dispersion relation of each later. For a square lattice this reads: $\langle m|\,\hat{\varepsilon}_{\mathbf{k}_{\|}}\,|l\rangle = -2\left(t_{m}^{x}\cos k_{x}+t_{m}^{y}\cos k_{y}\right)\delta_{ml}$
- the fully diagonal self-energy operator: $\langle m|\,\hat{\Sigma}\left(i\omega_{n}\right)|l\rangle = \Sigma_{m}\left(i\omega_{n}\right)\delta_{ml}$

With these additional contribution the matrix local Green's function will acquire a non-diagonal term due to $\hat{T}$:

$$\begin{aligned} G_m^{-1} = \langle m| \hat{G}^{-1} |m\rangle &= i\omega_n + \mu - \epsilon_m - \Sigma_m (i\omega_n) \\ G_{ml}^{-1} = \langle m| \hat{G}^{-1} |l\rangle &= -t_{ml} \end{aligned}$$

Following the derivation of the homogeneous case, the missing step is the relation between the lattice self-energy and the impurity one. With this purpose, we will now elucidate the missing connection between the impurity hybridization function Γ_i and the lattice matrix Green's function. The latter can be written in a compact fashion defining the diagonal operator:

$$\hat{\zeta} = (i\omega_n + \mu) \mathbf{1} - \hat{V} - \hat{\Sigma} (i\omega_n) \tag{4.4}$$

so as to have:

$$\hat{G}^{-1} (i\omega_n) = \hat{\zeta} - \hat{T} \tag{4.5}$$

While the site-dependent hybridization function Γ_i can be written with:

$$G_i (i\omega_n) \Gamma_i (i\omega_n) = \sum_{jk} t_{ij} t_{ki} \left[G_i (i\omega_n) G_{jk\sigma} (i\omega_n) - G_{ji} (i\omega_n) G_{ki} (i\omega_n) \right] \tag{4.6}$$

Is important to underline that, at this level, all the indexes of this equation have nothing to do with the system partition into layers, but have to be regarded, in a general way, as the indexes of the two-point connected Green's function. From

Eq.[4.6] follows:

$$\begin{aligned}
G_i\Gamma_i &= G_i \sum_{jk} \langle i|\, \hat{T}\, |k\rangle \langle k|\, \hat{G}\, |j\rangle \langle j|\, \hat{T}\, |i\rangle - \sum_{j} \langle i|\, \hat{T}\, |j\rangle \langle j|\, \hat{G}\, |i\rangle \sum_{k} \langle i|\, \hat{G}\, |k\rangle \langle k|\, \hat{T}\, |i\rangle \\
&= G_i \langle i|\, \hat{T}\hat{G}\hat{T}\, |i\rangle - \langle i|\, \hat{T}\hat{G}\, |i\rangle \langle i|\, \hat{G}\hat{T}\, |i\rangle
\end{aligned}$$

Now, recalling that $\hat{T} = \hat{\zeta} - \hat{G}^{-1}$, one has:

$$\begin{aligned}
G_i\Gamma_i &= G_i \left(\langle i|\, \hat{\zeta}\hat{G}\hat{\zeta}\, |i\rangle - \langle i|\, \hat{\zeta}\, |i\rangle \right) - \left(\langle i|\, \hat{\zeta}\hat{G}\, |i\rangle - 1 \right) \left(\langle i|\, \hat{G}\hat{\zeta}\, |i\rangle - 1 \right) \\
&= G_i^2\zeta_i^2 - G_i\zeta_i - \left(G_i^2\zeta_i^2 - 2G_i\zeta_i + 1 \right) \\
&= G_i\zeta_i - 1
\end{aligned}$$

Where the fact that the $\hat{\zeta}$ operator is fully diagonal, while $\hat{T}$ is not, has been extensively used. Reshaping the last equality one gets:

$$G_i = \frac{1}{\zeta_i - \Gamma_i} = \frac{1}{i\omega_n + \mu - \epsilon_i - \Sigma_i\left(i\omega_n\right) - \Gamma_i\left(i\omega_n\right)} \tag{4.7}$$

This equation relates the diagonal parts of the lattice local Green's function and lattice self-energy to the Weiss functions:

$$\mathcal{G}_i^{-1}\left(i\omega_n\right) = i\omega_n + \mu - \epsilon_i - \Gamma_i\left(i\omega_n\right) \tag{4.8}$$

Through the self-consistency equation:

$$\mathcal{G}_i^{-1}\left(i\omega_n\right) = G_i\left(i\omega_n\right) + \Sigma_i\left(i\omega_n\right) \tag{4.9}$$

This last expression closes the set of DMFT equations suited to describe an inhomogeneous lattice system. Operatively one has to:

- solve a set of N impurity problems with an initial guess on $\hat{\mathcal{G}}_o^{-1}(i\omega_n)$, in order to get the N-dimensional self-energy matrix $\hat{\Sigma}(i\omega_n)$;
- build the matrix

  $$\hat{A}\left(\mathbf{k}_{\|}, i\omega_n\right) = (i\omega_n + \mu)\,\mathbf{1} - \hat{\varepsilon}_{\mathbf{k}_{\|}} - \hat{T} - \hat{V} - \hat{\Sigma}(i\omega_n) \tag{4.10}$$

  which satisfies the condition $\hat{A}\left(\mathbf{k}_{\|}, i\omega_n\right)\hat{G}\left(\mathbf{k}_{\|}, i\omega_n\right) = \mathbf{1}$, and compute the layer-resolved local Green's function matrix

  $$\hat{G}^{loc}(i\omega_n) = \sum_{\mathbf{k}_{\|}} \hat{A}\left(\mathbf{k}_{\|}, i\omega_n\right)^{-1} \tag{4.11}$$

- exploit the self-consistency condition to extract a new Weiss field from the *diagonal* part of the local Green's function matrix:

  $$\left(\mathcal{G}_i^{new}\right)^{-1}(i\omega_n) = \Sigma_i(i\omega_n) + \left(G_i^{loc}\right)^{-1}(i\omega_n) \tag{4.12}$$

The loop is repeated until convergence of two subsequent solutions. The computational effort of the R-DMFT scheme roughly scales linearly with the number of impurity models, i.e. with the number of inequivalent sites in the original system.

4.2 Embedding Scheme for layered superconductors

As mentioned above, the proper way to treat problems related to layered geometries is to adopt a mixed representation. Indeed, the in-plane translational invariance is preserved, by means of a diagonal $\mathbf{k}_{\|}$, while a off diagonal hopping connects different planes. To the inverse of the system Green's function $\hat{A}\left(\mathbf{k}_{\|}, i\omega_n\right)$, will contribute all the diagonal single particle operators plus the self-energy matrix, while all inter-plane operator will contribute as off-diagonal terms. Thus, trying to deal with a 3D system in this notation, would give a infinite dimensional matrix, as a consequence, in order to exploit some sort of computational advantage, a truncation must be performed. In this framework, the existing embrional theory of the embedded medium has been extended and improved in the present thesis. We start defining how we are going to truncate the infinite number of planes needed to get the 3D systems and how the finite size side-effects of this truncation has been taken care of. In the case of N layer interposed between two semi-infinite leads the Green's function matrix can be defined as:

$$\begin{pmatrix} A_{B_1} & A_{B_1 L} & A_{B_1 B_2} \\ A_{LB_1} & \hat{A}_L & A_{B_2 L} \\ A_{B_2 B_1} & A_{LB_2} & A_{B_2} \end{pmatrix} \begin{pmatrix} \hat{G}_{B_1} & \hat{G}_{B_1 L} & \hat{G}_{B_1 B_2} \\ \hat{G}_{LB_1} & \hat{G}_L & \hat{G}_{B_2 L} \\ \hat{G}_{B_2 B_1} & \hat{G}_{LB_2} & \hat{G}_{B_2} \end{pmatrix} = \mathbf{1} \tag{4.13}$$

where:

- $\hat{A}_{LL}$ is the N-dimensional operator of the N layers that make the heterostructure, it takes the form of Eq.[4.10];

- A_B are the scalar operators referred to the semi-infinite bulk enclosing the heterostructured slab;

- A_{LB} are the scalar terms that connect the layers to the leads. Depending on the hopping range they can acquire extra dimension. In the single band repulsive Hubbard model one has $A_{LB} = \varepsilon_\perp = t^z$, while for the superconducting extension of this method $\hat{A}_{LB} = \hat{\varepsilon}_\perp = t^z \hat{\sigma}_z$;

- A_{BB} is the scalar term referred to the connection between the semi-infinite leads. In the following we will consider only nearest neighbor hopping, i.e. the leads are assumed far enough to consider negligible any mutual influence, then $A_{BB} = 0$.

From Eq.[4.13] we can extract the explicit expression for the layer resolved Green's function and understand how it is modified by the presence of the leads:

$$\begin{aligned}\hat{G}_L &= \left[\hat{A}_L - A_{LB_1} A_{B_1}^{-1} A_{B_1 L} - A_{LB_2} A_{B_2}^{-1} A_{B_2 L}\right]^{-1} \\ &= \left[(i\omega_n + \mu)\,\mathbf{1} - \hat{\varepsilon}_{\mathbf{k}_\parallel} - \hat{\Sigma}\left(i\omega_n\right) - \hat{S}_1\left(\mathbf{k}_\parallel, i\omega_n\right) - \hat{S}_N\left(\mathbf{k}_\parallel, i\omega_n\right)\right]^{-1}\end{aligned}$$

where we defined the energy dependent *embedding potentials* S:

$$\hat{S}_\alpha\left(\mathbf{k}_\parallel, i\omega_n\right) = \hat{\varepsilon}_\perp G_{B_\alpha}\left(\mathbf{k}_\parallel, i\omega_n\right)\hat{\varepsilon}_\perp \mathbf{1}\delta_{L\alpha} \tag{4.14}$$

The index α run from 1to N depending how deep into the slab the effect of the bulk goes, as we stated before, considering only nearest neighbor hopping one would get only $\alpha = 1$ and $\alpha = N$ scalar potentials. The present derivation can be straightforwardly extended to the superconducting case simply adding the extra anomalous component to the Green's function of each layer and considering $\hat{\varepsilon}_\perp = t^z \hat{\sigma}_z$ as inter-layer hopping.

The last step is to derive the correct expression for the semi-infinite bulk Green's function G_B, following the derivation of the foremost paper [42] in which the embedding method has been formulated for non-interacting systems. A standard tight-binding hamiltonian for a infinite piristine 3D lattice is:

$$\mathcal{H}_o = -t \sum_{\langle ij \rangle \in 3D} \left(\hat{c}_i^\dagger \hat{c}_j + h.c. \right) - \mu \sum_i \hat{n}_i \tag{4.15}$$

With the purpose to address systems with layered structure, this hamiltonian can be firstly partitioned into planes:

$$\begin{aligned}
\mathcal{H}_o &= -t \sum_{\langle i_m j_m \rangle \in 2D} \left(\hat{c}_{i_m}^\dagger \hat{c}_{j_m} + h.c. \right) - \mu \sum_{i_m} \hat{n}_{i_m} - t \sum_{\langle mn \rangle \in 1D} \left(\hat{c}_m^\dagger \hat{c}_n + h.c. \right) \\
&= \sum_m \mathcal{H}_m + \sum_{\langle mn \rangle \in 1D} \hat{T}_{nm}
\end{aligned}$$

then rewritten using the mixed $\{|m, \mathbf{R}_{i_m}\rangle\}$ representation defined above:

$$\mathcal{H}_o = \sum_{m\mathbf{k}_\parallel} \left(\varepsilon_{m,\mathbf{k}_\parallel} - \mu \right) \hat{n}_{m,\mathbf{k}_\parallel} + \sum_{\langle mn \rangle \in 1D} \hat{T}_{nm} \tag{4.16}$$

We now consider the semi-infinite crystal by starting from a piristine 3D crystal, described by $\mathcal{H}_o$, and inserting an imaginary plane in a given, say $[100]$, crystallographic direction. In the following we will refer to the system made by two semi-infinite crystal with the term *cleaved crystal*, while for surface we indicate the planes of atoms immediately adjacent to the cleavage plane, which is just a mathematical tool aimed to separate the system in a left and right side. In the following we will refer to a geometry where $m < 0$ indicates the left portion systems, while $m \geq 0$ the right portion.

The Hamiltonians of the perfect and cleaved crystals are then:

$$\begin{aligned}\mathcal{H}_o &= \sum_{L,R}\left(\mathcal{H}_{m_L}+\hat{T}_{m_L n_L}\right)+\hat{T}_{m_R m_L}+\left(\mathcal{H}_{m_R}+\hat{T}_{m_R n_R}\right)\\ \mathcal{H} &= \sum_{L,R}\left(\mathcal{H}_{m_L}+\hat{T}_{m_L n_L}+\hat{U}_{m_L}\right)+\left(\mathcal{H}_{m_R}+\hat{T}_{m_R n_R}+\hat{U}_{m_R}\right)\end{aligned}$$

Where we used the $m_L\,(m_R)$ notation to indicate planed on the left(right) side of the cleavage plane. $\mathcal{H}$ is the hamiltonian perturbed by the plane and by definition the hoppings connecting the left and right side are missing. One can consider an additional perturbation $\hat{U}$ arising, e.g., due to a change in the electronic distribution near the surface, that cannot be written in a general way. We will introduce later this perturbation in a self-consistent way. The overall perturbation is:

$$\begin{aligned}\hat{V} &= \mathcal{H}-\mathcal{H}_o\\ &= -\hat{T}_{m_R m_L}+\hat{U}_{m_R}+\hat{U}_{m_R}\end{aligned}$$

With the following matrix elements:

$$\begin{aligned}\left\langle m_\alpha \mathbf{k}_\parallel\right|\hat{V}\left|m_\beta \mathbf{k}_\parallel\right\rangle &= V_{m_\alpha m_\beta}\left(\mathbf{k}_\parallel\right)\\ &= V_{0-1}+V_{-10}+U_0+U_{-1}\end{aligned}$$

where, in the last equality, we condidered nearest neighbor hopping. As usual, the connection between the perturbed Green's function $\hat{G}$ and the unperturbed one $\hat{G}^{(o)}$ is:

$$G_{mn}\left(\mathbf{k}_{\|}\right)=G_{mn}^{(o)}\left(\mathbf{k}_{\|}\right)+\sum_{pq}G_{mp}^{(o)}\left(\mathbf{k}_{\|}\right)V_{pq}\left(\mathbf{k}_{\|}\right)G_{qn}\left(\mathbf{k}_{\|}\right) \tag{4.17}$$

in this equation the Green's function indexes runs over all the planes. The required symmetry conditions, yet to be demonstrated, are:

$$\begin{aligned} \left\langle m,\mathbf{k}'_{\|}\right|\hat{G}^{(o)}\left|n,\mathbf{k}_{\|}\right\rangle &= G_{mn}^{(o)}\left(\mathbf{k}_{\|},m-n\right)\delta\left(\mathbf{k}'_{\|}-\mathbf{k}_{\|}\right) \\ \left\langle m,\mathbf{k}'_{\|}\right|\hat{G}\left|n,\mathbf{k}_{\|}\right\rangle &= G_{mn}\left(\mathbf{k}_{\|},m,n\right)\delta\left(\mathbf{k}'_{\|}-\mathbf{k}_{\|}\right) \\ \left\langle m,\mathbf{k}'_{\|}\right|\hat{V}\left|n,\mathbf{k}_{\|}\right\rangle &= V_{mn}\left(\mathbf{k}_{\|},m,n\right)\delta\left(\mathbf{k}'_{\|}-\mathbf{k}_{\|}\right) \end{aligned} \tag{4.18}$$

here $\hat{G}^{(o)}$ depends only on the difference $(m-n)$ since is the Green's function of the perfect infinite crystal. Now we start from a general definition of $G^{(o)}\left(\mathbf{k},\omega\right)$ and derive an expression for $G_{mn}^{(o)}\left(\mathbf{k}_{\|},m-n\right)$ that fulfill the symmetry conditions of Eq.[4.18]. The Green's function of the unperturbed lattice is:

$$\left\langle\mathbf{k}'\right|\hat{G}^{(o)}\left|\mathbf{k}\right\rangle=\frac{\delta\left(\mathbf{k}-\mathbf{k}'\right)}{\omega+i\eta-\varepsilon\left(\mathbf{k}\right)}=G^{(o)}\left(\mathbf{k},\varepsilon\right) \tag{4.19}$$

Our mixed representation can be obtained from a partial Fourier transform of the fully translational invariance k space:

$$\left|m,\mathbf{k}_{\|}\right\rangle=\frac{1}{\sqrt{N_{\perp}}}\sum_{\mathbf{k}_{\perp}}\left|\mathbf{k}\right\rangle e^{-i\mathbf{k}_{\perp}m\mathbf{d}} \tag{4.20}$$

so that:

$$\begin{aligned}
\left\langle m,\mathbf{k}'_{\|}\right|\hat{G}^{(o)}\left|n,\mathbf{k}_{\|}\right\rangle &= \frac{1}{N_{\perp}}\sum_{\mathbf{k}_{\perp}\mathbf{k}'_{\perp}}\left\langle \mathbf{k}'\right|\hat{G}^{(o)}\left|\mathbf{k}\right\rangle e^{-i\mathbf{k}_{\perp}n\mathbf{d}+i\mathbf{k}'_{\perp}m\mathbf{d}} \\
&= \frac{1}{N_{\perp}}\sum_{\mathbf{k}_{\perp}\mathbf{k}'_{\perp}}\frac{\delta\left(\mathbf{k}-\mathbf{k}'\right)}{\omega+i\eta-\varepsilon\left(\mathbf{k}\right)}e^{-i\mathbf{k}_{\perp}n\mathbf{d}+i\mathbf{k}'_{\perp}m\mathbf{d}} \\
&= \frac{1}{N_{\perp}}\sum_{\mathbf{k}_{\perp}\mathbf{k}'_{\perp}}\frac{\delta\left(\mathbf{k}_{\|}-\mathbf{k}'_{\|}\right)\delta\left(\mathbf{k}_{\perp}-\mathbf{k}'_{\perp}\right)}{\omega+i\eta-\varepsilon\left(\mathbf{k}\right)}e^{-i\mathbf{k}_{\perp}n\mathbf{d}+i\mathbf{k}'_{\perp}m\mathbf{d}} \\
&= \frac{1}{N_{\perp}}\sum_{\mathbf{k}_{\perp}}\frac{e^{i\mathbf{k}_{\perp}(m-n)\mathbf{d}}}{\omega+i\eta-\varepsilon\left(\mathbf{k}\right)}\delta\left(\mathbf{k}_{\|}-\mathbf{k}'_{\|}\right) \\
&= G^{(o)}_{mn}\left(\mathbf{k}_{\|},m-n\right)\delta\left(\mathbf{k}'_{\|}-\mathbf{k}_{\|}\right)
\end{aligned}$$

only considering the obvious orthogonality between $\mathbf{k}_{\|}$ and $\mathbf{k}_{\perp}$ vectors, the solution with the right translational symmetry has been achieved. Now, considering only the perturbed Green's function of the $m=0$ surface, on the right of the cleveage plane, one has:

$$\begin{aligned}
G_0 &= G^{(o)}_0+\left[G^{(o)}_0U_0+G^{(o)}_{0-1}V_{-10}\right]G_0 \\
&= \frac{G^{(o)}_0}{1-\left[G^{(o)}_0U_0+G^{(o)}_{0-1}V_{-10}\right]}
\end{aligned} \tag{4.21}$$

Hence, the needed unperturbed Green'function $G^{(o)}_{mn}$, in order to write down the formal expression for the Green's function of the topmost surface of the semiinfinte right bulk are:

$$\begin{aligned} G_0^{(o)}\left(\mathbf{k}_{\|},\omega\right) &= \frac{1}{N_\perp}\sum_{\mathbf{k}_\perp}\frac{1}{\omega - i\eta - \varepsilon\left(\mathbf{k}\right)} \\ G_{0-1}^{(o)}\left(\mathbf{k}_{\|},\omega\right) &= \frac{1}{N_\perp}\sum_{\mathbf{k}_\perp}\frac{e^{-i\mathbf{k}_\perp\mathbf{d}}}{\omega - i\eta - \varepsilon\left(\mathbf{k}\right)} \end{aligned} \tag{4.22}$$

Clearly, since we are dealing with correlated systems, to these Green's function will correspond a bulk self-energy. Operatively, in the non-uniform DMFT procedure, one has to:

- include the calculation of two additional impurities, one for each lead and compute the correlated version of Eq.[4.22] in the DMFT language:

  $$G_a^{(o)}\left(\mathbf{k}_{\|},i\omega_n\right) = \frac{1}{N_\perp}\sum_{\mathbf{k}_\perp}\frac{e^{-i\mathbf{k}_\perp\mathbf{d}a}}{i\omega_n + \mu - \varepsilon_{\mathbf{k}_{\|}} - 2t^z\cos\mathbf{k}_\perp - \Sigma_B\left(i\omega_n\right)} \tag{4.23}$$

  for $a = 0$ and $a = -1$.

- build the Green's function of the surface of the semi-infinite bulk $G_B\left(\mathbf{k}_{\|},i\omega_n\right) = G_0\left(\mathbf{k}_{\|},i\omega_n\right)$ with Eq.[4.23], and the corresponding embedding potential $S\left(\mathbf{k}_{\|},i\omega_n\right)$;

- build the inverse of the slab Green's function matrix $\hat{A}\left(\mathbf{k}_{\|},i\omega_n\right)$ inserting the potentials in the extremals components, i.e., those connected to the leads, and proceed with the DMFT loop previously described.

It is important to underline how S is not a static quantity: it is updated each loop since the sum over $\mathbf{k}_{\|}$ of Eq.[4.23] provides a local Green's function for the semi-infinite bulks $G_B^{loc}\left(i\omega_n\right) = \sum_{\mathbf{k}_{\|}} G_B\left(\mathbf{k}_{\|},i\omega_n\right)$ through wich we define the Weiss fields (and the related Anderson parameters) via the self-consistency condition:

$$\left(\mathcal{G}_B^{new}\right)^{-1}(i\omega_n) = \Sigma_B(i\omega_n) + \left(G_B^{loc}\right)^{-1}(i\omega_n) \tag{4.24}$$

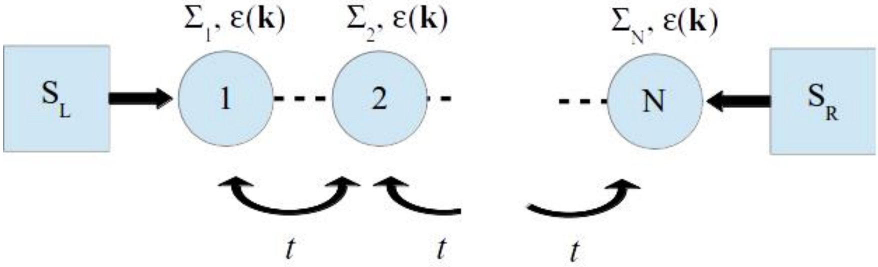

Figure 4.1: Sketch of inhomogeneous DMFT + Emedding operational scheme.

Fig.[4.2] presents results for a ten-layer slab for uniform parameters $U/t = -9$ and half-filling. In the absence of any embedding potential, the slab breaks translational symmetry and the order parameter Δ becomes larger at the edges. Introducing the embedding potential according to the described scheme, we obtain the results shown as a dotted green line with large dots in Fig.. Here we consider completely uniform parameters, and the embedding potential strongly reduces the inhomogeneity, even if a minor enhancement of the order parameter is clear at the edges of the slab. In order to further reduce the effects of the finiteness of the slab, in this thesis we propose a simple strategy to improve the scheme, introducing a feedback of the slab on the semi-infinite bulks. The idea is simply to define a potential created by the slab onto the semi-infinite bulks on the two edges. As a matter of fact G_B calculated this way is insensitive to the presence of the slab: the embedding potentials, in which the effects of the bulks are enclosed, acts only from the leads to the extremals layers Green function. Assuming that an embedding potential is a general way to consider, within the Green function of a layer, the effect of an adjacent system, whose details resides in the structure of the potential itself, this approach has been used to include a *feedback* potential S_S from the $m = 1$ and $m = N$ layers to the bulks. Namely, from the second iteration $S_S\left(\mathbf{k}_{\|}, i\omega_n\right) = \varepsilon_{\perp} G_m\left(\mathbf{k}_{\|}, i\omega_n\right)\varepsilon_{\perp}$ is computed and inserted in Eq.[4.21] so as to have:

$$G_0 = \frac{G_0^{(o)}}{1 - \left[G_0^{(o)} U_0 + G_{0-1}^{(o)} V_{-10} - S_S\right]} \tag{4.25}$$

The data in Fig.[4.2] demonstrate that the feedback further reduces the inhomogeneity and it allows to essentially reproduce the uniform bulk even with a very limited number of layers.

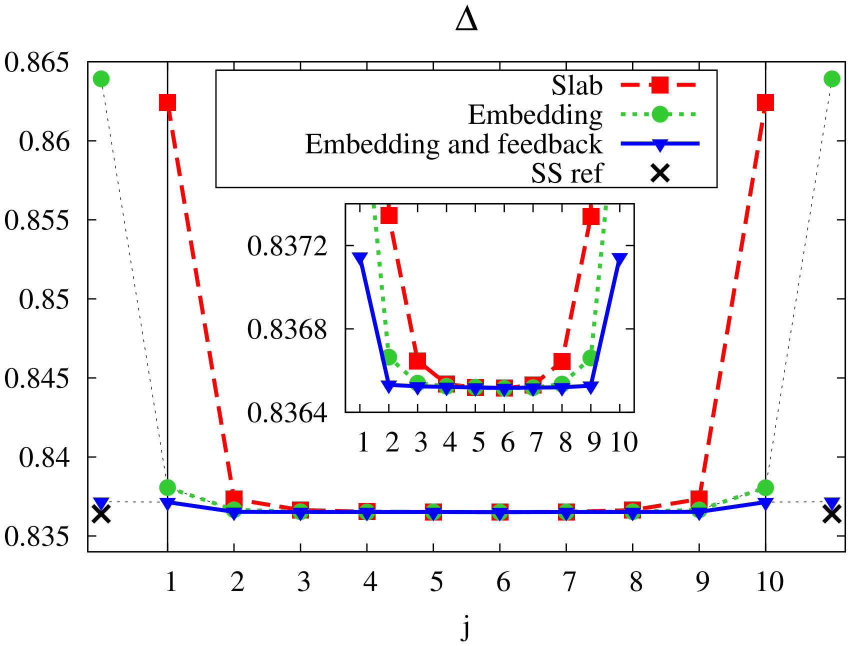

Figure 4.2: Order parameter Δ vs layer index of a 10 layer system with uniform Hubbard parameter $U/t = -9$ at half-filling. Red line: Δ enhancement in the external layers of a slab. Green line: Δ profile of the same system connected with the leads, the dots refers to the order parameter calculated with $\hat{G}_B$. A considerable disagreement with the bulk reference (crosses) is found. Blue line: the inclusion of the feedback potential turns into a reduction of both leads and external layers order parameters to a value much closer to the bulk reference. The inset shows a magnification of the mentioned effects

4.3 Layered DMFT for the Attractive Hubbard model

In this section we present the first results using the embedding+feedback procedure for an attractive Hubbard model. In this section we limit ourselves to this extremely simplified situation in order to test the performance of our approach in a well-controlled model and to single-out the effects which arise from the strength of the pairing interaction from the many other effects which are expected to take place in a real system.

Furthermore, in this section we fix the local density to one electron per site on each layer by imposing particle-hole symmetry. This chouce obviously freezes charge redistribution across the interface. We chose to start with this situation to single out the intrinsic effects due to the proximity from the effects due to charge transfer across the interface, which would obviously affect the results. Interestingly, we find important proximity effect even in this case.

4.3.1 Observables

To characterize the superconducting states of our layered superconductor and its spatial dependence we focused on few relevant observables. The most direct evidence of the superconducting state and its strength is the layer-resolved zero-temperature pairing amplitude, simply obtained as the integral of the anomalous part of the α-th layer Green's function:

$$\Delta_\alpha = T \sum_n F_\alpha \left(i\omega_n \right) = \langle \hat{c}_{\alpha\sigma} \hat{c}_{\alpha\bar{\sigma}} \rangle \tag{4.26}$$

while the kinetic energy reads:

$$\langle E_k^\alpha \rangle = T \sum_n \int d\epsilon \rho \left(\epsilon \right) Tr \left\{ \epsilon \hat{\sigma}_3 \hat{G}_\alpha \left(\epsilon, i\omega_n \right) \right\} \tag{4.27}$$

Notice that while the global order parameter and potential energy are simply obtained by summing the contributions from the different layers, the bulk kinetic energy also includes the contributions from the interlayer hoppings, which do not contribute to the above $\langle E_k^\alpha \rangle$. Finally we can compute the quasiparticle weight, namely:

$$z_\alpha = \left(1 - \partial\Sigma_\alpha^{11}\left(i\omega_n\right)/\partial\left(i\omega_n\right)\right)^{-1} \tag{4.28}$$

Where $\Sigma_\alpha^{11}\left(i\omega_n\right)$ is the normal component of the α-th layer self-energy. We use z_α as a measure of the coherence of the low-lying excitations at the gap edge. In a BCS superconductor these excitations are completely coherent and we recover $z = 1$, while increasing the coupling it decreases even if slightly.

4.3.2 Benchmark with the homogeneous reference

In Fig. we demonstrate that our feedback performs accurately for different observables and for any value of the parameters. We consider again homogeneous parameters and we vary the value of the interaction U. Here we plot the average over the slab of Δ, z and of the double occupancy D as a function of U and we compare with a bulk cubic lattice (which should be reproduced when the finite-slab effect are canceled) and, for reference, with a two-dimensional calculation corresponding to a single layer. To illustrate the general validity of our approach we consider both a negative U , for which we find superconductivity, and a positive U model, in which s-wave superconductivity can not establish and therefore representing the normal state. The three panels of Fig.[4.3.2] clearly show that for every value of U the three observables coincide with their bulk counterparts.

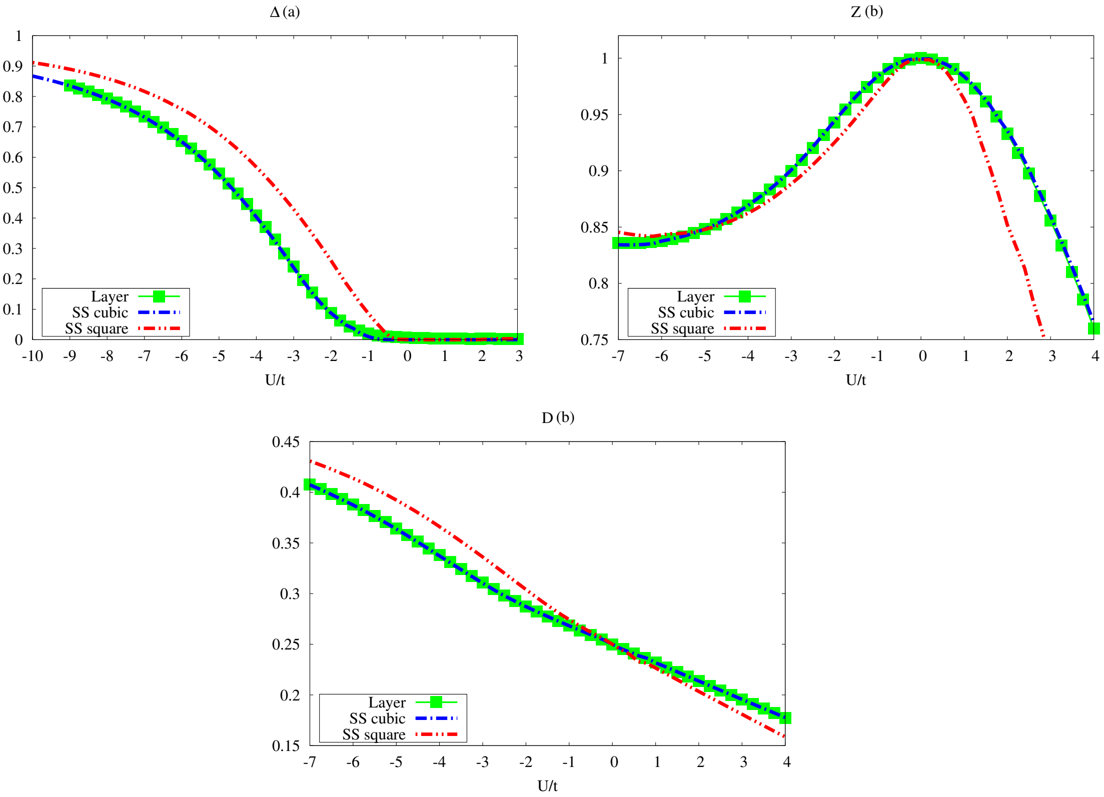

Figure 4.3: (a) Order parameter Δ, (b) quasiparticle weight z, (c) double occupations expectation value $D = \langle \hat{n}_{o\uparrow}\hat{n}_{o\downarrow} \rangle$ vs interaction strength U at half-filling. Red and blue lines refers respectively to the square and cubic lattice, single site DMFT calculations. Green dots represents the results for the central plane of an homogeneous system made of 7 layers, similar to the blue one in Fig.

4.3.3 Interface between weak- and strong-coupling superconductors

As a first example we consider the interface between two semi-infinite systems with different values of the attractive interaction, considering ten active layers for both systems. In Fig.[4.3.3] we present results in which we fix the interaction at a relatively small interaction $U/t = -3$ on the left side, while on the right side we tune the interaction from $U/t = -3$ to a much larger attraction $U/t = -7.5$. We present layer-resolved pairing amplitude Δ_α , quasiparticle weight z_α, double occupancy D_α and in-plane kinetic energy $\langle E_{k\alpha} \rangle$ as a function of the layer index α. On the right side of the figure the bulk values are shown for reference. We first observe that also in this case our embedding+feedback scheme provides an essentially continuous connection between the leads (corrected by the feedback) and the first layers which we explicitly treat with layered DMFT. The evolution across the slab is rather smooth, especially for the order parameter, shown in panel (a), for which a significant proximity effect leads to an enhancement of the order parameter on the left side which penetrates for almost ten layers. The effect is quantitatively significant. For example the order parameter in the first layer of the weak-coupling superconductor can be increased by 50% when the pairing amplitude of the right system is $U = -7t$. Also the right-side is substantially affected by the presence of the weakly-coupled superconductor. The reverse effect on the strong-coupling superconductor is however smaller in absolute and relative terms with an order parameter which is reduced at most of 10%. Interestingly the spatial extent over which the order parameter is affected is not strongly dependent on the value of the interaction in the right half. The double occupancy, which is also related to the potential energy has a similar evolution, but the proximity effects are limited to a thinner slice of the slab of around three layers and the relative change induced by proximity is much smaller. A similar behavior is shown by the layer kinetic energy, which is negative and larger in amplitude on the left (weak-coupling side). Interestingly, the presence of the stronger-coupling superconductors leads to a slight increase of the modulus of the kinetic energy in the first layers of the weak-coupling side.

Finally, the quasiparticle weight, which can be used to measure the coherence of the electronic excitations, is slightly increased in the weak coupling side, and it de- creases in the strong-coupling region, even if all these variations are relatively small.

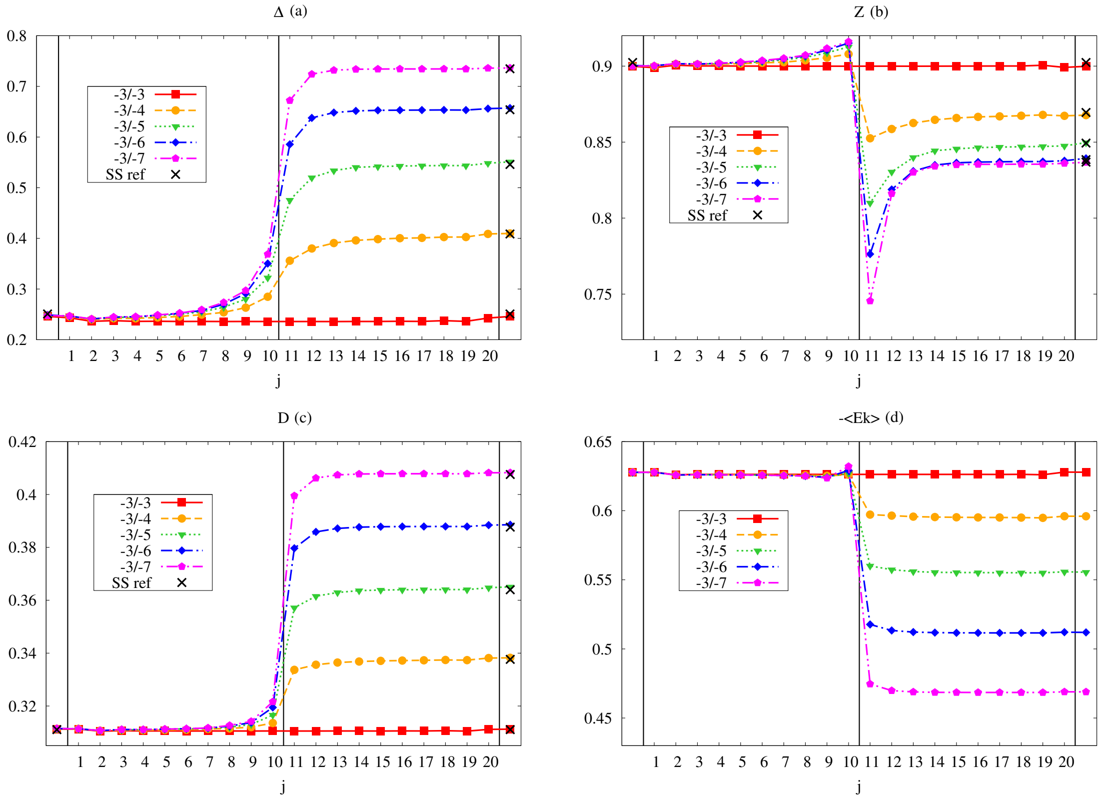

Figure 4.4: Δ_α, z_α, D_α and $-\langle E_k \rangle$ in a 20 layer thick heterostructure. The calculation starts from the omogeneous case in which both left (index ≤ 10) and right sides (index ≥ 11) have the same $U/t = -3$, and proceed decreasing U in the right side. The points outside the heterostructure are those computed starting from the leads Green's functions used to compute the embedding potential $\hat{G}_B$. The crosses are the results for a bulk DMFT calculation for the cubic lattice.

In Fig.[4.3.3] we present an analogous analysis in which the left side has a constant $U/t = -10$ while on the right side the interaction goes from $-10t$ to

$-3t$. The qualitative results are similar to the previous even if the proximity effects are reduced both in their spatial extension and it the strength of the effect because of the stronger coupling on the left side, which leads to a short coherence length and the physics becomes more local. Still, a clear intermediate region, where the physical quantities smoothly connect, appears. Also in this case, the effect is quantitatively stronger for the superconducting order parameter, which is again increased up to a factor 2 on the weaker- coupling side (now the right half)

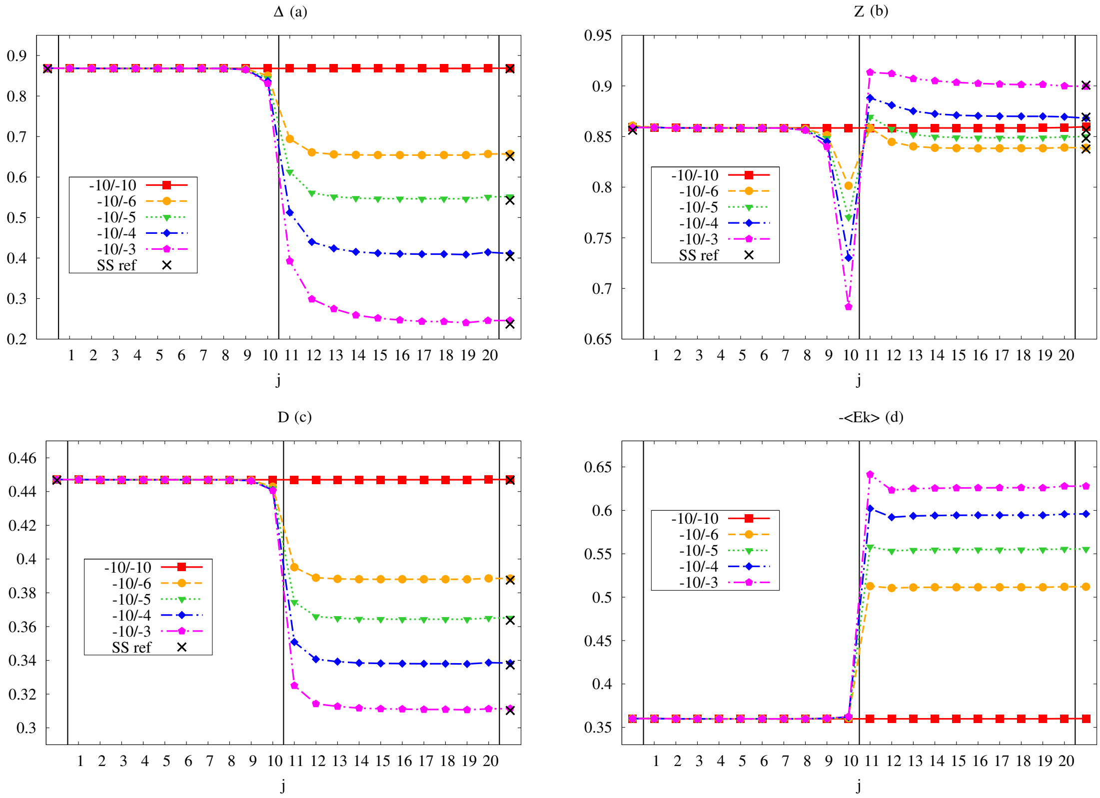

Figure 4.5: Δ_α, z_α, D_α and $-\langle E_k \rangle$ in a 20 layer thick heterostructure. The left half (index ≤ 10) is kept at $U/t = -10$, while for the right half (index ≥ 11) we used smaller or equal values of the attraction strength.

4.3.4 Interface between correlated metal and superconductor

We now move to a different situation where one of the two halves of the system would not be superconducting by itself. On the left side we consider a metal with a finite repulsion U/t = 4, which would lead to a moderately correlated metal in a bulk system, while on the right we tune the attractive interaction from 0 to $U = -6t$. The results, plotted in Fig.[4.3.4], show that despite the repulsive interaction superconductivity can penetrate for a few lay- ers of the metal, and that important effects are observed on the superconducting side. This is a clear qualitative violation of the local-density approximation even in the absence of charge redistribution across the interface. The effect on the order parameter is small but clearly visible (one obtains an order parameter which is around 0.05 the bulk value on the superconducting side), while the double occupancy is essentially unaffected by the connection between the two semi-infinite systems. The kinetic energy presents an interesting increase (in modulus) in the first layers of the metallic system, the same region where superconductivity is able to penetrate in the repulsive metal. These results clearly demonstrate that the approach we have devised is able on one hand to reproduce the bulk results when we are sufficiently far from the interface and on the other hand to display non-trivial and interaction dependent proximity effects, which can lead to important effects in real systems. The effect is generally strongerfor the order parameter than for the other observables we considered.

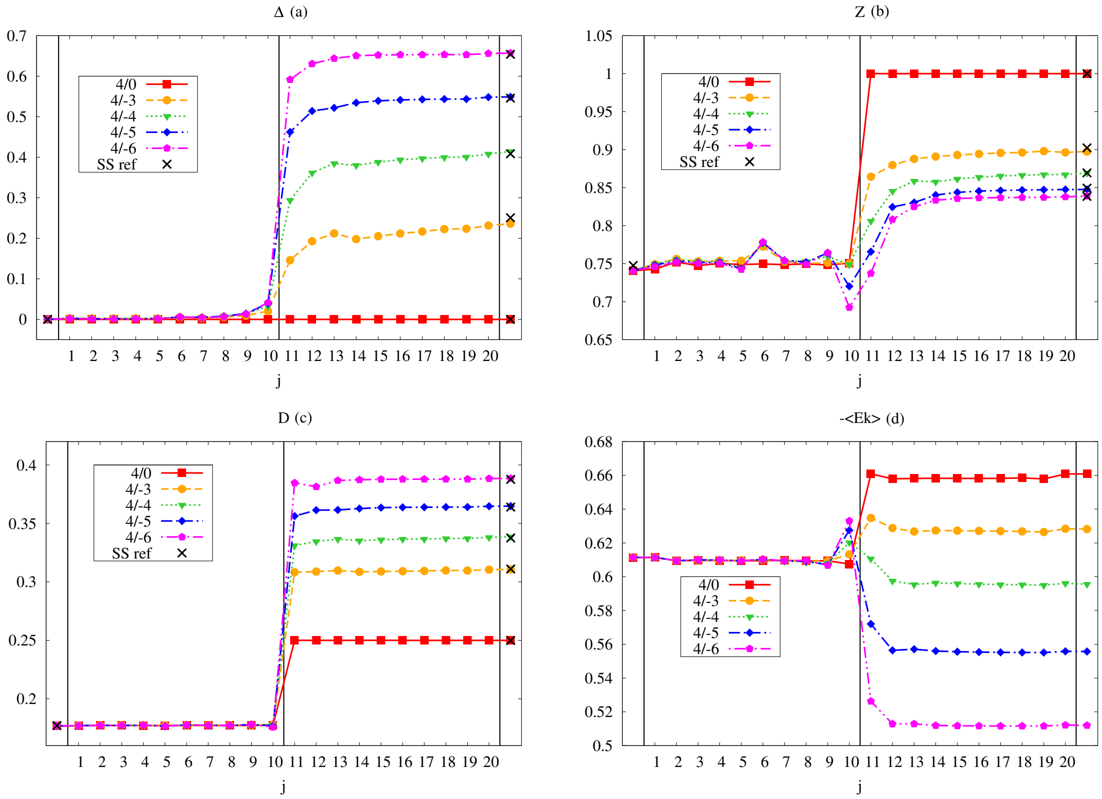

Figure 4.6: Δ_α, z_α, D_α and $-\langle E_k \rangle$ in a 20 layer thick heterostructure. Here on the left side we have a correlate metal with a repulsive $U/t = 4$, while on the right side we tune an attractive interaction.. The wiggles in the quasiparticle weight are a numerical artifact due to the small energy scales involved in the calculation of the derivative.

4.3.5 Conclusions

In the present section we have introduced an effective extension of the embedding approach which allows to study heterostructure of interacting systems by means of a small number of active layers. Our extension is twofold. For the first time we extend the formalism to the superconducting state, and we also introduce a "feedback" of the slab onto the embedding potential which reduces the finite-size effects introduced by the finiteness of the slab. We have demonstrated that the feedback correction indeed dramatically reduces the effects of a finite slab and it produces essentially exact results for all the relevant layer-resolved observables when treating homogeneous bulk systems. After having established the accuracy of the refined embedding approach, we have also presented two applications of the method to paradigmatic situations where a heterostructure is formed out of two semi-infinite systems separated by a two-dimensional interface. In particular we consider a superconductor with different values of the attractive strength connected with either a superconductor or a metal with intermediate repulsive interactions. We find that in the first case important proximity effects take place and stronger superconductor increases the superconducting order parameter for around ten layers for a wide range of parameters. In the second case superconductivity penetrates in the repulsive system for around two layers, qualitatively changing the physics of the system. In both cases the strongest effects are seen on the order parameters, while the kinetic and potential energies remain closer to the results for two disconnected systems. It is worth mentioning that, imposing particle-hole symmetry and fixing every layer to be half-filled, we freeze the charge redistribution which would naturally enhance the effects we describe. In this paper we limited to the simple attractive Hubbard model at half-filling in order to benchmark our method and, more importantly, to single out the effects associated with the strength of the coupling from the vaiety of effects happening at a real interface. Indeed our results demonstrate that this approach can be used to study interface or heterostructures involving two superconductors with different coupling strength, which can be seen as a greatly simplified version of heterostructures involving copper oxides with different doping, or heterostructures involving Mott insulators and s-wave superconductors. However, our method can be extended to include several realistic features. For example the ap- proach can be applied to the paradigmatic LTO/STO system, where the STO can be modeled as a Mott insulator with positive U , while LTO can be described as a band insulator with a weak electron-phonon interaction. The latter can be either approximated with an at-tractive Hubbard interaction or with an actual coupling between the electrons and phononic degrees of freedom. Indeed our approach can be straightforwardly extended to models in which the s-wave superconductivity arises from electron-phonon coupling of the Holstein type. In this case one could study if the presence of STO can turn LTO into a superconductor by providing carriers to the band insulator, thereby activating the BCS pairing as in doped bulk LTO. Furthermore, the present approach can also be combined with density-functional theory to introduce the realistic electronic structure and close the gap with actual materials.

CHAPTER

5

ELECTRON-PHONON COUPLING IN CORRELATED SYSTEMS: FROM BULK TO HETEROSTRUCTURES

In this section we present our new results on the Holstein-Hubbard model using DMFT to study homogeneous systems, and its layered extension to study heterostructures connecting a Mott insulator with a band insulator mimicking the LTO/STO system. The main focus of this Chapter is the study of the effects on superconductivity of the competition between the instantaneous Hubbard repulsion and the retarded attractive interaction driven by dispersionless phonons. In Chapter 2 we have discussed previous results on the non-superconducting phase and we have shown that in the half-filled system the only way to observe phonon fingerprints is to assume that the electron-phonon coupling exceeds the Coulomb interaction. In this Chapter we focus on the effect of doping on this competition with a particular interest on the possible onset of a phonon-driven s-wave superconducting phase in a system dominated by the Hubbard repulsion.

5.1 Half-filled Hubbard-Holstein model

In most of the present Chapter we will therefore study the DMFT solution of the Holstein-Hubbard model on the Bethe lattice with semi-elliptic density of states given by $D\left(\varepsilon\right) = \frac{2}{\pi D^2}\sqrt{D^2 - \varepsilon^2}$, semibandwidth $D = 1$ and adiabatic ratio $\gamma = 0.2$ for various Hubbard interaction U/D and electron-phonon coupling λ. In Chapter 2 we have already reported in Fig.[2.5] the phase diagram in the U-λ plane of the model obtained neglecting any long range ordered phase. A correlated metallic phase extends in a region surrounded by a Mott Insulator and a bipolaronic insulator. The transition line between the metal and the MHI is only weakly dependent of the $e - ph$ interaction strength and the transition is always of second order. The transition between M and BPI instead is second-order for small coupling and it turns into a first-order line when the interactions are intermediate or strong. Here we focus on the metallic region surrounded by the insulating phases, which is the most likely ground from which superconductivity can originate. To better characterize the competition between the two interactions and to understand to what extent this metallic state can support s-wave superconductivity, we first focus on the quasiparticle weight and the efffective mass (which are simply inversely proportional within DMFT).

As it has been pointed out before [75], the competition between the two interactions leads to non-monotonous behavior of these quantities as a function of the control parameters. Indeed both the $e-e$ and $e-ph$ interaction would lead to a reduction of quasiparticle weight and an increase of the effective mass in the absence of the competing interaction. This is showm, for example in the data of the two panels of Fig.[5.1] and Fig.[5.2], which show the two quantities. In the left panels we show results as a function of λ for different value of U while the right panels show them as a function of U for different values of λ. This corresponds respectively to vertical and horizontal cuts in the phase diagram in Fig.[2.5].

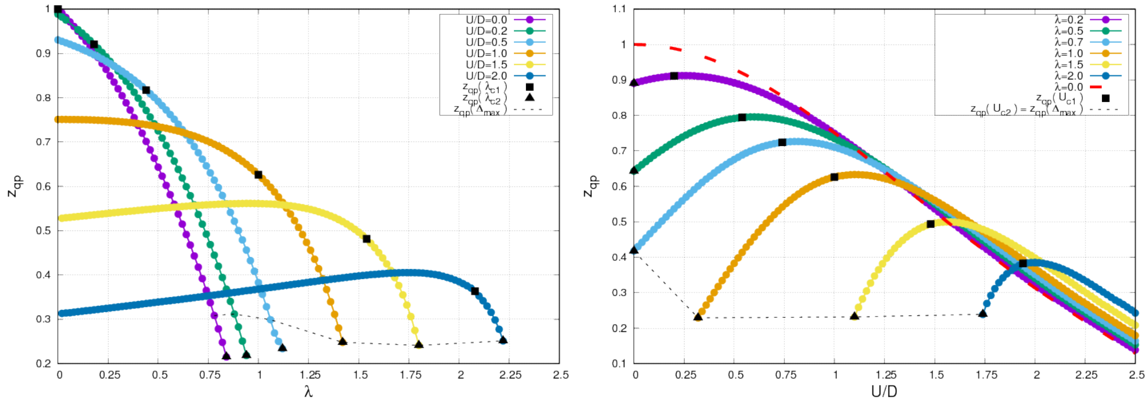

Figure 5.1: (left) Quasiparticle weight z_{qp} for various values of the Hubbard interaction strength as a function of λ, corresponding to vertical cuts to the phasediagram of Fig.[2.5]; (right) Quasiparticle weight z_{qp} for various values of the $e-ph$ interaction strength λ as a function of U, corresponding to horizontal cuts on the same phasediagram. The Red dotted line in the U/D dependent figure and in the following ones represent the result for the repulsive Hubbard model in absence of the phononic bath.

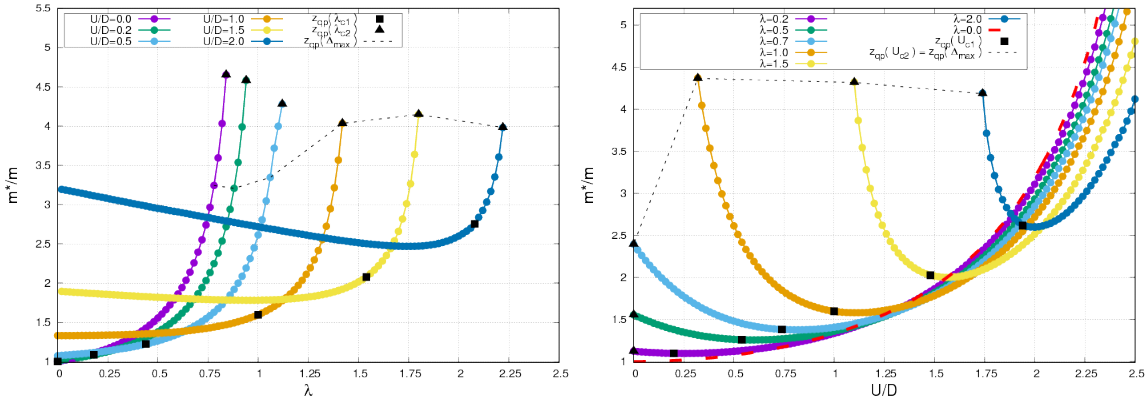

Figure 5.2: Effective mass ratio ${}^{m^*}\!/_{m} \sim {}^{1}\!/_{z_{qp}}$ versus λ at fixed U/D (left) and versus U/D at fixed λ (right)

For small values of $U/D \leq 1$ the effective mass indeed increases with λ reflecting the crossover to polaronic carriers while it shows a non monotonic behaviour at higher U/D. The mononotonic behavior is a direct consequence of the competition between the two interactions. For finite U the system has already some correlations in the absence of λ. Turning the $e-ph$ coupling on, the first effect is to effectively reduce the Coulomb repulsion, thereby reducing the correlations and making the system closer to a non-interacting one. This is the region where Z increases as a function of λ. When the $e-ph$ coupling is of the same order of U, a further increase leads instead to a more standard renormalization due to the phonons, which corresponds to the final decrease before the BPI is reached. Each line, corresponding to a different value of U ends indeed n the BPI transition line, marked with a black triangle at the critical value $\lambda_{c2}(U)$. The transition is definitely first-order for intermediate and large U, while for small U the character of the transition appears more continuous. Indeed it has been shown [17] that the second-order nature of the transition requires an extremely accurate study to be unambiguously detected already in the pure Holstein model. Extending this careful study in the presence of correlations would be an extremely lengthy work which lies beyond the scope of the present work.

A completely analougous effect can be seen considering cuts with fixed λ: for weak $e-ph$ coupling z is substantially unaffected by phonons and reflects a trend driven by U/D only, while for larger λ the non monotonic behavior of z is revealed. As can be seen from the comparison with the $\lambda = 0$ case the value of U_c at which the Mott insulating phase occurs is shifted to higher values increasing the $e-ph$ coupling strength. Obviously this behaviour can be explained through the same effective coupling previously described. Here the system with $U = 0$ is already correlated by the finite λ, and switching on U we first counteract the phonon effects before entering in the regime where U dominates over the $e-ph$ coupling and the Z is reduced as a function of U

before reaching the continuous Mott transition. The main difference between the two plots was already apparent in the phase diagram. The critical λ for the BPI strongly depends on the value of U, while the Mott transition critical point weakly depends on λ.

We now move to the superconducting phase in order to connect the properties of the normal state with the potential for a superconducting phase. Indeed only a few studies addressed the superconducting (SC) properties of this model, and we still lack a sistematic understanding on how s-wave superconductivity occurs in the non-trivial adiabatic regime, where the competition between instantaneous Hubbard interaction and retarded electron-phonon coupling has more subtle features. In this Chapter we investigate what are the chances to develop s-wave superconductivity in the presence of correlations and we focus in particular on the dependence on the carrier density. Naively, one can surmise that the region where phonon-driven superconductivity can establish is that where the $e - ph$ couplling prevails, namely close or beyond the line separating the metallic state from the bipolaronic insulator. This line coincides with the $U/D = \lambda$ line in the strong $e - e$ coupling regime while it deflects toward higher values of λ for intermediate coupling strengths. This line, in the antiadiabatic $\omega_o \to \infty$ limit, separates the region where the effective interaction $U_{eff} = U - \lambda D$, is globally repulsive or attractive. Hence, if there is a chanche for superconductivity in the half-filled model, this is the region to explore. On the other hand, the competition between the two terms is expected to become less extreme as we introduce doping, which will give the electron-phonon interaction more space to be active. Therefore, in the rest of the chapter we will focus on the doping dependence to look for the ideal conditions to establish superconductivity.

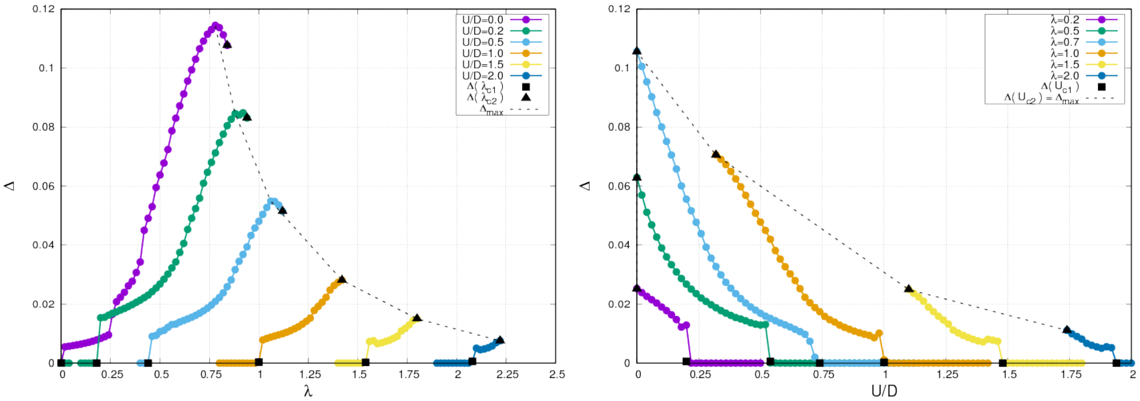

Figure 5.3: Superconducting order parameter Δ versus λ at fixed U/D (left) and versus U/D at fixed λ (right). Black square points represent the last value of the coupling in the metallic phase in absence of superconductivity. Black triangle points represents the last converged DMFT solution, i.e. right before the bipolaronic insulator phase. The dotted black line indicates the interaction strength that gives the highest value of the order parameter.

In Fig.[5.3] we plot the order parameter defined as the expectation value of the singlet cooper pair $\Delta = \langle \hat{c}_{\downarrow} \hat{c}_{\uparrow} \rangle$ as a function of the $e - ph$ interaction strength (left) and of the Hubbard interaction (right) following the same scheme we used to plot Z and m^*. As expected, for $U/D = 0$ we find superconductivity for every value of λ until the bipolaronic transition takes place ($\lambda < \lambda_{c2}\,(U = 0)$). Indeed in this case a superconducting solution exists also for $\lambda > \lambda_{c2}\,(U = 0)$, but it is degenerate with the charge-density wave. As a matter of fact, it is extremely hard to follow the superconducting solution in the regime where the charge-ordered bipolaronic state establishes because of a numerical tendency to break the spatial symmetry. We did not perform the very demanding numerical calculation necessary to follow the superconducting solution until very large values of λ because these values are not interesting for the systems we would like to study. A similar behavior is found for small values of U, where however there is a minimal value of λ, that we call λ_{c1}, for superconductivity to establish. Clearly this testifies that some value of λ is always necessary to overcome the repulsive interaction. The value of λ_{c1} correspond to the one at which the effective interaction becomes attractive only for intermediate Hubbard interaction, while it deviates to even higher values at stronger $e-e$ coupling. Finally, we find that retardation effects that allows to stabilize a superconducting solution even in the $\lambda < U/D$ case are found below $U/D = 1$. We can expect en enhancement of this interesting effect pushing the adiabatic ratio to lower values, which have not been explored so far.

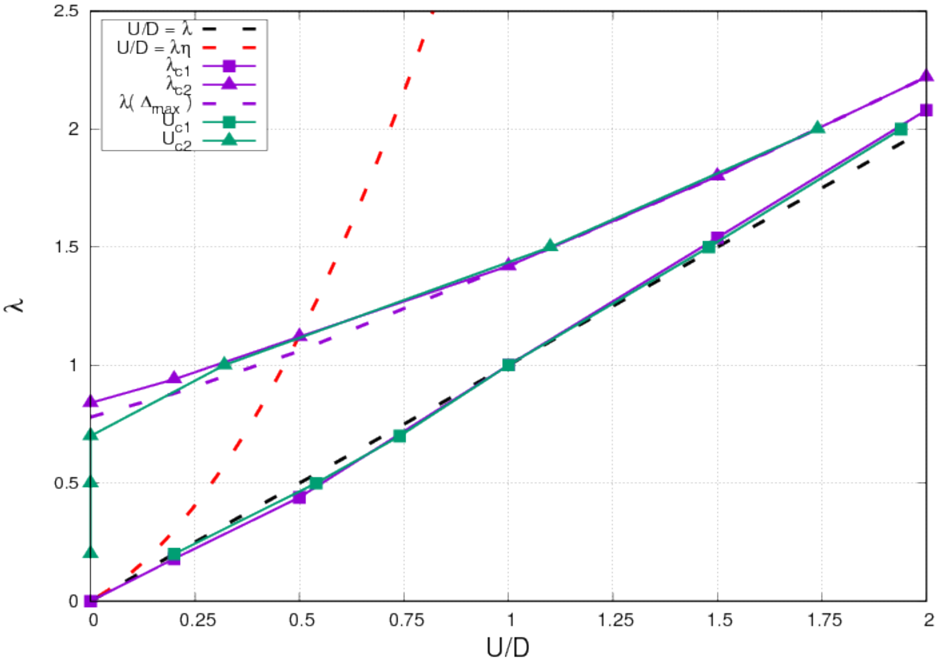

Figure 5.4: Superconducting boundary in the phase diagram of Fig.[2.5]. Here U_{c1} and U_{c2} are the equivalent of λ_{c1} and λ_{c2} in the case of horizontal cuts. The red dotted line indicates the value of λ that would give an effective attraction in the Kondo coupling expansion of Eq.[2.34].

The results for the critical values of λ that encloses the SC region of the phase diagram are summarized in Fig.[5.4] and they mostly follow the normal-state diagram of Fig.[2.5]. The transition to the SC state is found to be always first order in our numerical implementation and, comparing with Fig.[5.1], it is found to occur when $z_{qp}\left(\lambda, U\right)$ has almost its maximum value on the fixed λ cut. This is indeed the value of λ for which the carriers are closer to non-interacting as a result of the cancellation between the two interaction terms. As we mentioned above, in the region of moderate repulsion, this value is significantly reduced with respect to $U = \lambda$, signaling that retardation effect play a positive role. Finally we observe that the maximum value of the order parameter does not necessarily correspond to the maximum $e-ph$ coupling available before the bipolaronic instabilities hits, i.e. λ_{c2}. This is a further non-trivial result associated to retardation effects.

We can give a rough and naive argument to rationalize the onset of superconductivity in terms of the region of frequency in which the effective interaction is attractive according to the dynamical effective interaction which is simply given by:

$$\omega_o\sqrt{1-\frac{\lambda D}{U}} < \omega < \omega_o \tag{5.1}$$

This frequency region shrinks towards zero when $\lambda D/U \rightarrow 0$ and it achieves its maximum extension, reaching zero frequency $\omega \in [0, \omega_o]$ at $\lambda D = U$. For this reason superconductivity is essentially guaranteed to establish at $\lambda = U$, while more subtle retardation effects can reveal it in a wider region of parameters.

To gain further insight on how the $e-ph$ interaction effects can survive the strong correlations, we now focus on another quantity directly related to the

$e-ph$ interaction, namely the phonon displacement distribution. As we mentioned in the section describing the implementation of DMFT for the Holstein-Hubbard model, this is a groundstate observable and is given by the quantum average of the projection operator $\left|\hat{x}\right\rangle\left\langle\hat{x}\right|$ on the subspace where the ion displacement operator $\hat{x}$ has the eigenvalue x:

$$P\left(x\right)=\left\langle\Psi|\hat{x}\right\rangle\left\langle\hat{x}|\Psi\right\rangle \tag{5.2}$$

This quantity can be used to measure the magnitude of the local distortion, being:

$$\left\langle\hat{x}\right\rangle=\int xP\left(x\right)dx \tag{5.3}$$

as well as their fluctuation:

$$\left\langle\hat{x}^2\right\rangle=\int x^2P\left(x\right)dx \tag{5.4}$$

At weak coupling $P\left(x\right)$ is centered around a single value (unimodal) with a peak that broadens upon increasing λ. In the strong $e-ph$ coupling regime, $P\left(x\right)$ eventually develops a multi peaked structure which indicates different possible distortions, each associated to one of the charge states. This is another, more quantitative, description of a polaronic state, in which the charge state and the phonon displacement are deeply entangled.

Physically, this means that a certain fraction of lattice sites are polarized by the presence of electrons so as to have an average polarization greater than its own fluctuations. In Fig.[5.5] we report the phonon displacement distribution, for all the values of the Hubbard interaction considered, in the close proximity of the two critical values of the $e - ph$ coupling λ_{c1} and λ_{c2} relevant for the SC.

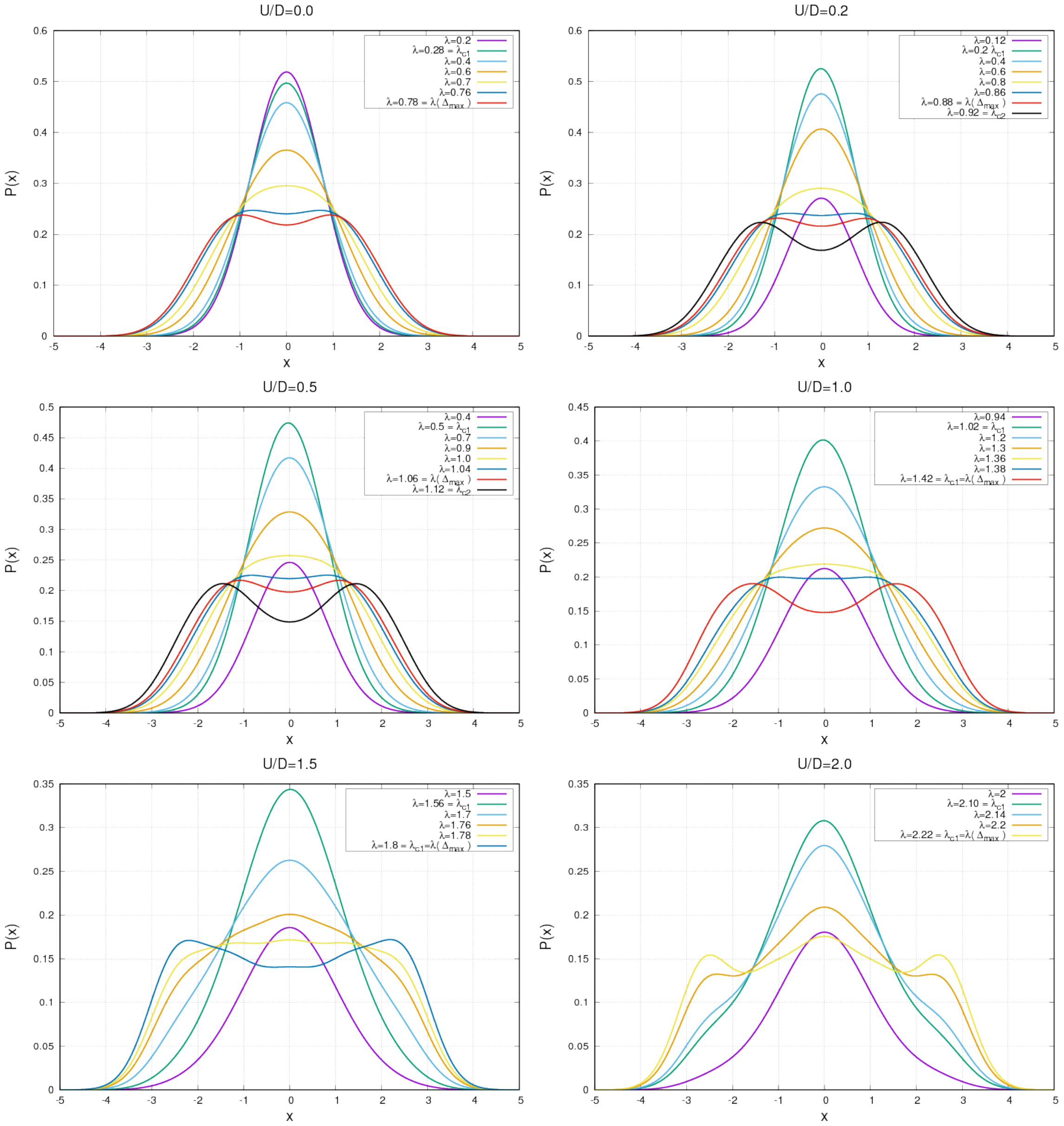

Figure 5.5: Phonon displacement distributions $P(x)$ for the coupling strength for which SC has been found

The first thing that we notice is the quench on the unimodal distribution at the onset of SC: we found this increase systematically for each value of U/D. Increasing λ the distribution lowers its central peak and, at λ_{c2}, the system reach the BPI phase as the distribution becomes bimodal. A closer inspection to the values of the $e-ph$ strength reveals that the maximum value of the superconducting order parameter is found when the system has the most pronounced displacement fluctuations right before entering the BPI as shown in Fig.[5.6], while the development of a finite distortion is detrimental to superconductivity. This is also the reason why we did not push further the calculations to stabilize the superconducting phase in the region beyond λ_{c2}.

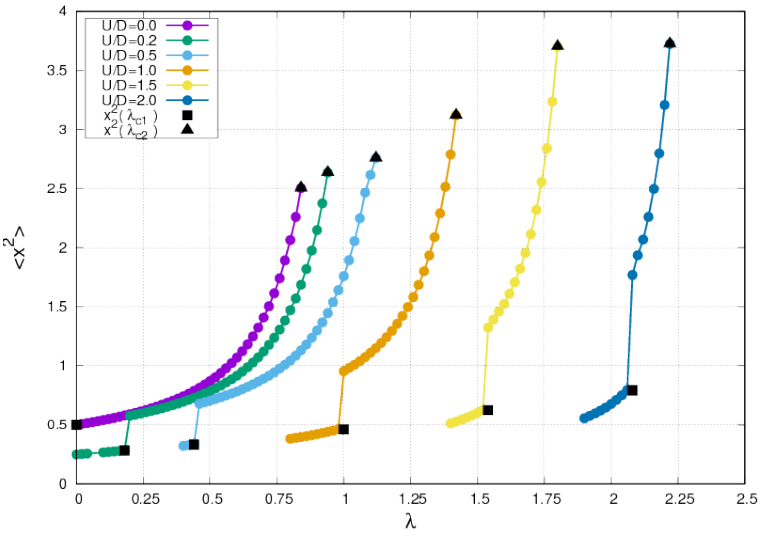

Figure 5.6: Average distortion fluctuation compute as $\left\langle \hat{x}^2 - \langle \hat{x} \rangle^2 \right\rangle$

The role of position fluctuation and phonon softening as a precursor of the BPI metal-insulator transition have been already pointed out, as we discussed in Chapter 2, but its relevance in the context of superconductivity has never been discussed so far. Our result reveals that the ideal conditions for an electron-phonon superconductor in the presence of correlations are not given by the largest value of the effective coupling, which may drive a finite distortion thereby favoring a charge-ordered state, but they are associated to a maximum of the charge fluctuations, which are indeed the key condition to have electron-phonon driven superconductivity.

5.2 Finite doping case

As we described in the previous section, the reduced effectiveness of the $e - ph$ coupling in the presence of strong $e{-}e$ correlation, can be explained considering that the Hubbard interaction freezes the charge fluctuation, to whom phonons are coupled. This charge-freezing phenomenon is particularly extreme at half-filling, where an actual Mott-Hubbard transition can take place, and it becomes less and less pronounced as we dope the system away. On the other hand, the electron-phonon interaction is expected to remain active also for significant doping, at least as far as the ability to drive superconducting pairing is concerned.

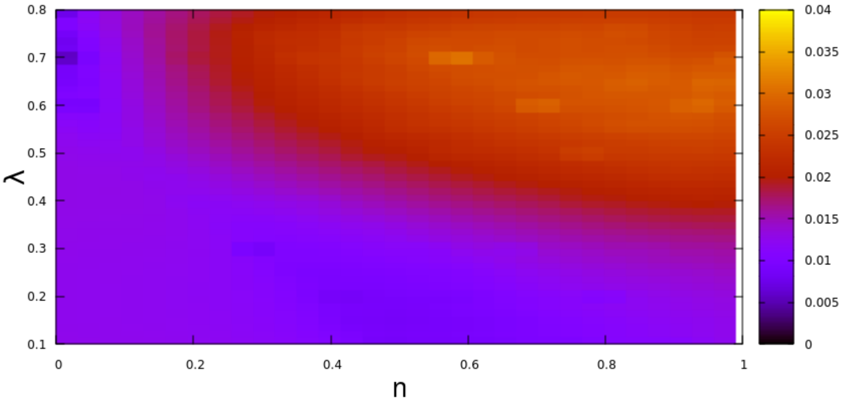

Figure 5.7: Superconducting order parameter for the Holstein model ($U = 0$) as a function of λ and n Notice that the color scale is different with respect to Fig. 5.2.1

For this reason we have performed extensive calculations for the superconducting phase of the Hubbard-Holstein model as a function of the density n, the electron-phonon coupling λ and the Hubbard repulsion U.

We start by presenting the results for a pure Holstein model, which we report in Fig.[5.2],which we compare with those for an intermediate interaction strength $U/D = 1$ in Fig.[5.2].

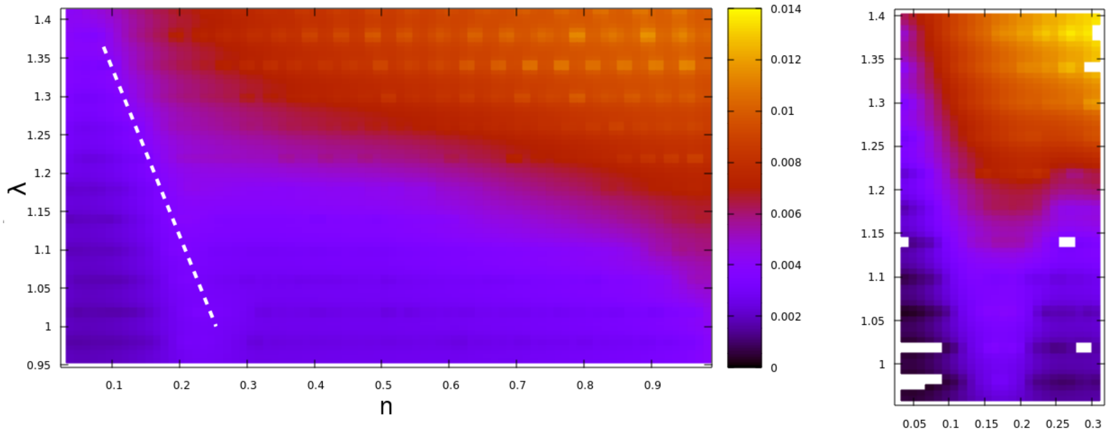

Figure 5.8: (left)λ, n Superconducting order parameter of the Hubbard-Holstein model at intermediate interaction strength $U/D = 1$ with emphasized the position of the emergent SC dome at high doping. (right) magnification of the emergent SC dome at intermediate densities. Notice that the color scale is different with respect to Fig. 5.2.1

The system without $e - e$ correlation displays a superconducting groundstate for every value of λ and n (identical results would be obtained for $n > 1$ because of particle-hole symmetry). and the superconducting order parameter is maximum around half-filling and it decreases as a function of doping due to the reduced density of states. Obviously Δ increases as a function of λ for any density.

A much richer phenomenology is revealed in the presence of correlations.

Notice that, for graphical purposes, the two diagrams have a different color scale and the same color corresponds to a reduction by a factor 3 of the order parameter. For $n = 1$ we start from the results shown in Fig.[5.3], while decreasing n the order parameter is first reduced but, at low densities, it starts to increase before finally vanishing for the completely empty band $n = 0$. This is particularly clear in the intermediate λ region. In the right panel we show a magnification of the low-density region where the revival of superconductivity is observed, which shows a clear dome-shaped behavior around a small density $n \simeq 0.2$. We have thus identified a region where strong correlations lead to a revival of superconductivity far from the region where the superconducting order parameter is maximum for the purely phononic system. We emphasize the behavior in this region in the middle panel of the right colum of Fig.[5.9], where we plot cuts at different λ. This shows how the low-density dome appears at $n \sim 0.2$ and λ_{c1} and eventually merges with the main SC structure that persists up to the same density when $\lambda_{c1} < \lambda < \lambda_{c2}$.

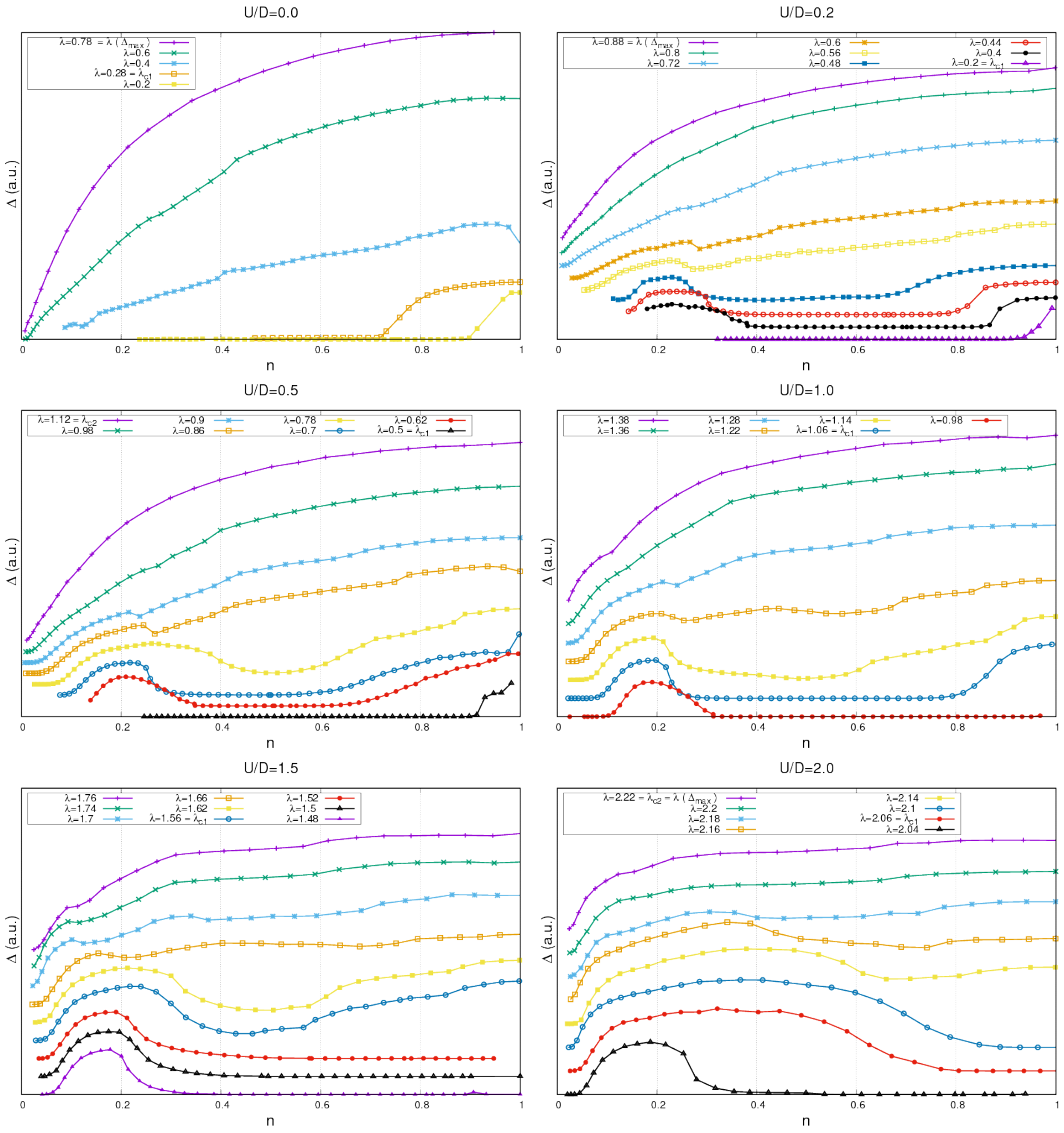

Figure 5.9: Horizontal cuts to the λ, n phase diagram for various U/D. The lines have been shifted upwards for graphical purposes.

In the other panels of Fig.[5.9] we plot the same information for different values of U/D. It is apparent that the low-density region is ubiquitously present as long as the interaction strength is not vanishing, and it always merges with the $n = 1$ dome when the coupling is increased. In the case of large U, which is the most relevant for transition-metal oxides (bottom-right panel), indeed one finds that the low-density region expands to intermediate and relatively large densities for intermediate electron-phonon interaction strength. In this regime one would conclude that the main superconducting phase is indeed the finite-density dome which then extends to half-filling.

As we described in the previous section, the onset of superconductivity by enhancing λ in the Holstein-Hubbard model for U/D has a first-order character at half filling. Instead in the hole-doped system the same SC transition is found to be of second order, as shown in Fig.[5.10]. Once again the $n = 1$ order parameter profile is the same of Fig.[5.3] displaying a coexistence between the metallic and SC solution at $\lambda = \lambda_{c1}$ and the line corresponding to the lowest plotted density roughly coincides with the emerging dome of Fig.[5.2]. At the smallest densities we have some artifical jumps in the plot due to the numerical difficulties to converge DMFT results in the low-density region.

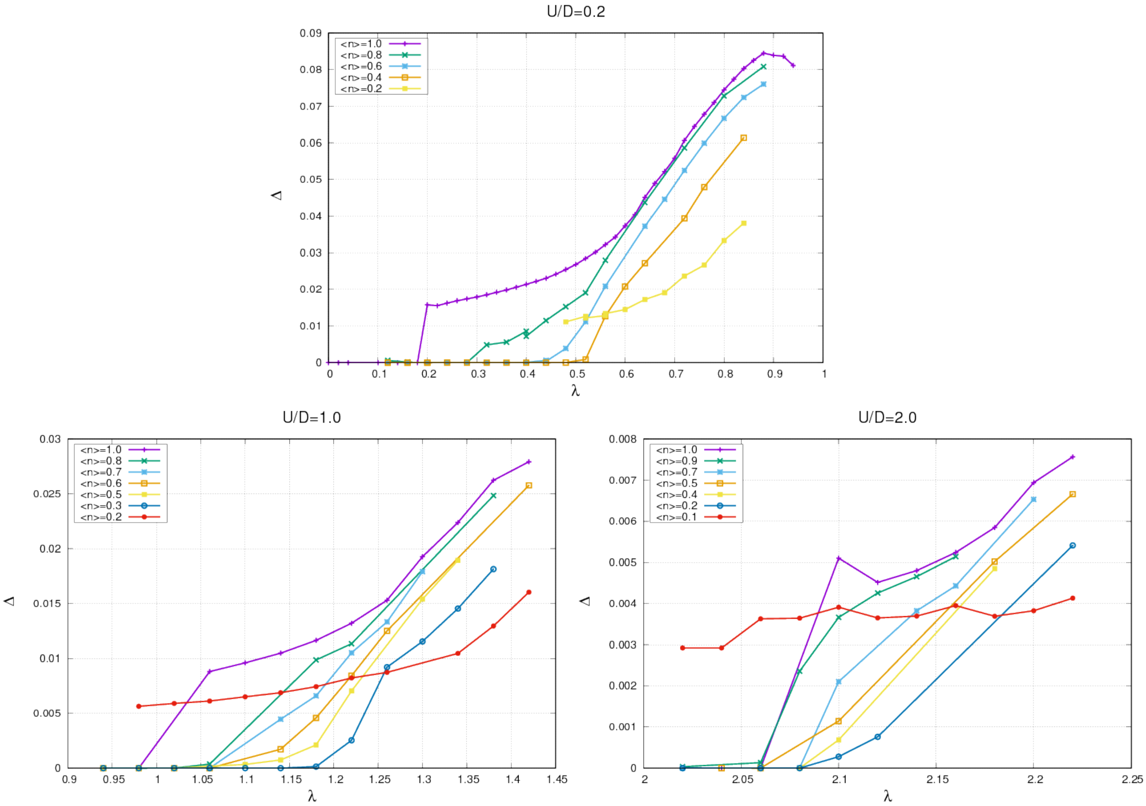

Figure 5.10: Superconducting order parameter as a function of λ for three values of U and different densities.

The last effect we analyze in this system is the dependence of the quasiparticle properties on the $e-ph$ coupling. It has been shown that in the strong $e-e$ correlation regime the $e-ph$ coupling has a little effect on mass renormalization for a wide range of densities. In Fig.[5.11] we plot the effective mass renormalization as a function of λ for different doping levels and for different degrees of $e-e$ correlation following the same graphical representation we used for the superconducting order parameter in Fig. [5.10]. While in the half-filled case of the weakly interacting system $m*/m$ rapidly increases towards the polaronic regime, for lower densities this exponential enhancement softens. Upon further increasing the Hubbard interaction, the mass renormalization become almost insensitive to the $e-ph$ coupling strength at low densities, where the value of $m*/m$ is completely determined by U/D. Interestingly, the latter is the region of parameters where we found the broadest superconducting region as a function of doping.

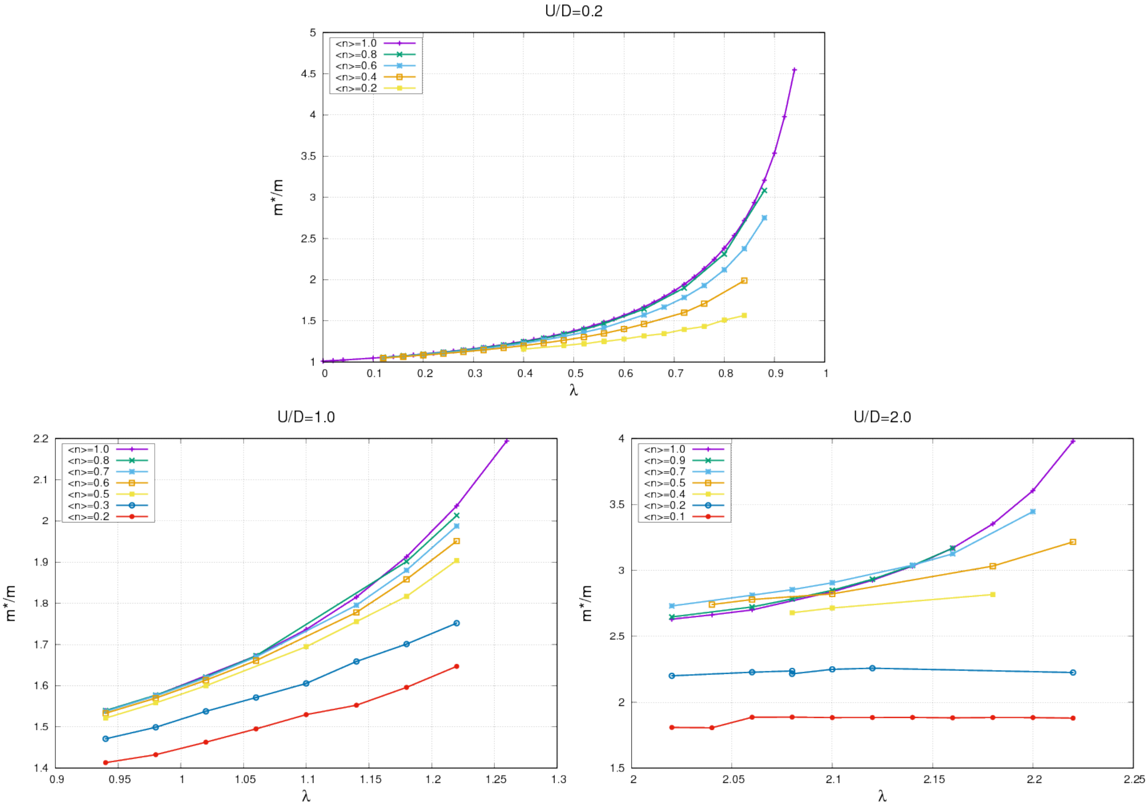

Figure 5.11: Effective-mass renormalization as a function of λ for three values of U and different densities.

Finally, to show in a comprehensive fashion the effect of doping on the mass renormalization due to the $e-ph$ coupling, for different values of the Hubbard interaction, in Fig.[5.12] we plot m^{*}/m as a function of λ for different U/D and fillings. Remarkably, the results for all the values of U/D considered in this section collapse on the same line when the carrier density is $n \sim 0.2$. This result is twofold: firstly it demonstrate that, under a certain doping level, the $e-e$

does not affect the quasiparticle properties of the system. On the other hand, in this strongly-correlated region the polaronic exponential mass enhancement is completely overwhelmed by the repulsion. This forbids the formation of polarons and the occurrence of a finite displacement which, as we discussed in the previous section, is detrimental for superconductivity.

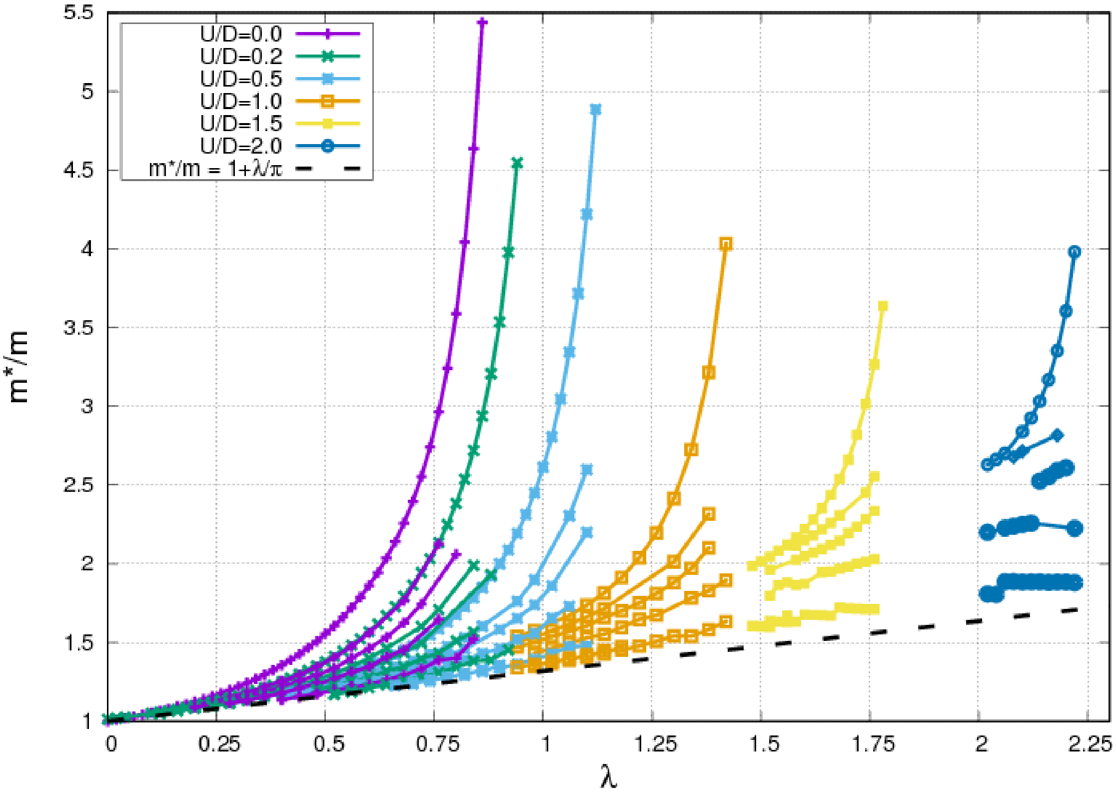

Figure 5.12:

The line onto which all the results seems to collapse can be understood through a simple Hartree-Fock analysis of the self-energy [1]. The Hubbard interaction involves only electrons with opposite spin while the effective retarded $e-ph$ coupling is insensitive to the spin and is coupled to the total density.

Therefore the total Hartree contribution to the self-energy is:

$$\Sigma^{H}\left(0\right)=\left(U-\lambda D\right)\frac{n}{2}-\lambda D\frac{n}{2}=\left(U-2\lambda D\right)\frac{n}{2} \tag{5.5}$$

where the first term comes from processes involving opposite spins, while the second is due to interactions between parallel spins. This term in the limit of low density vanishes. The Fock contribution to the self-energy in a system coupled to bosons is given by:

$$\Sigma^{F}\left(i\omega_{n}\right)=-\frac{\lambda D}{2}\omega_{o}\int d\epsilon N\left(\epsilon\right)\left[\frac{f^{e}\left(\epsilon\right)+f^{b}\left(-\omega_{o}\right)}{i\omega_{n}-\left(\epsilon+\omega_{o}\right)}-\frac{f^{e}\left(\epsilon\right)+f^{b}\left(\omega_{o}\right)}{i\omega_{n}-\left(\epsilon-\omega_{o}\right)}\right] \tag{5.6}$$

where $N\left(\epsilon\right)$ is the non interacting density of states and f^{e} and f^{b} are the electronic and bosonic statistical distibutions respectively. The integral can be solved in the two relevant limits of the adiabatic ratio:

$$\Sigma^{F}\left(i\omega_{n}\right)=\begin{cases}\xrightarrow[\omega_{o}\to\infty]{} & -\frac{\lambda D}{2}\left(n-1\right)\\ \xrightarrow[\omega_{o}\to 0]{} & -\frac{\lambda D}{2}i\omega_{n}N\left(\epsilon_{F}\right)\end{cases} \tag{5.7}$$

where $N\left(\epsilon_{F}\right)$ is the density of states at the Fermi level. In the case under investigation and reported in Fig.[5.12] the Hartree-Fock contribution to the self-energy is then given by:

$$\Sigma^{HF}\left(i\omega_{n}\right)=-\frac{\lambda D}{2}i\omega_{n}\left(\frac{2}{\pi D}\right) \tag{5.8}$$

and the effective mass ratio becomes:

$$\frac{m^*}{m} \sim \frac{1}{z_{qp}} = 1 - \left.\frac{\partial \Im\left[\Sigma\left(i\omega_n\right)\right]}{\partial i\omega_n}\right|_{i\omega_n=0} = 1 + \frac{\lambda}{\pi} \tag{5.9}$$

This result holds only in the low density limit, in which the Hartree contribution can be neglected, and for intermediate values of the Hubbard interaction. Setting, as a matter of fact a lower bound to m^*/m. Also this feature is captured by Fig.[5.12] where the agreement between the Hartree-Fock limit and the line where the data collapse lowers with increasing U/D. As a matter of fact, in this region of parameters, the $e-e$ interaction almost completely quenches the effects of the $e-ph$ interaction allowing only for a Hartree-Fock-like shift which corresponds to a perturbative results. This condition however is sufficient to drive superconductivity in this low-density region.

5.3 The case study of LTO/STO

Artificial heterostructures based on correlated insulating TMOs display remarkable changes in the electronic properties by changing the thickness of the constituent layers. As we described, among the most studied heterostructures are those hosting a metallic bidimensional layer at the interface between two insulators. The case of the LTO/STO junction between a Mott and a band insulator is the ideal playground for the study of an electronic reconstruction which is not influenced by structural distortion. In this interface the 2DEG has been demonstrated to be confined mainly on the STO side, where the charge depleted from the LTO coating is accumulated within a few unit cells, essentially doping an empty d-band. Remarkably this interface, the popular LAO/STO system, becomes superconducting under $300mK$. A possible source of pairing which seems to be supported by the experimental evidence is the electron-phonon coupling. A strong coupling between a longitudinal optical phonon and the electrons has been indeed found and polaronic features have been proposed. This raises the question as to whether the electron-phonon superconductivity of a simple Hiolstein model can be responsible for this phenomenon once we factor in all the many factors which should result in the fragile balance stabliizing this low-temperature superconductors. As we discussed, low carriers density, Coulomb repulsion and phononic retarded attraction, reduced dimensionality and electrostatic stability of the 2DEG should all play a role. In this section we tried to merge our knowledge, acquired studying these problems separately, with the purpose to demonstrate the stability of a superconducting phase in a model system as close as possible to the real one. Thus we considered a substrate of 10 layers of a band insulator (which models STO) with a 5-layer thick coating of Mott insulator representing LTO. The difference between STO sites and LTO sites is given by the fact that the LTO layers host a a positive $+1$ point charges that represents La interstitial ions. For the sake of simplicity we consider a single-band description for the titanium atoms of both oxides. In the absence of the interface, this band would be empty for STO sites and half-filled for LTO sites due to the positive charge of the La ions.

The minimal electrostatic long-range interaction of an electron belonging to the T_i d band, is then given by the interplay of mutual repulsion, between electrons on neighboring sites at $\mathbf{R}_i$, and attraction, produced by the La ions at $\mathbf{R}_{j_{La}}$ as in Fig.[5.13].

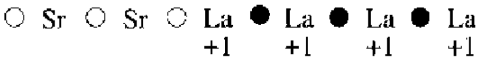

Figure 5.13: Sketch of the minimal unidimensional modellization of the LTO/STO junction

To capture all the main features of the LTO/STO junction within an inhomogeneous DMFT scheme, we considered our system of 15 layers, each with its own self-energy arising from a specific impurity model as described in Chapter 3. For every layer we assume the same Hubbard repulsion $U/D = 2.5$ and a coupling with a local Holstein phonon. The choice of a uniform Hubbard U does not take into account the fact that Ti atoms in STO are expected to have a smaller screened Coulomb repulsion then those in LTO, but we preferred to avoid to introduce one extra free parameter (the difference between the two Hubbard interactions). While the local correlations are treated dynamically by means od DMFT, the non-local correlations which are necessary to describe the charge redistribution through the interface are treated via a Hartree approximation to include, at the self-consistency level, all the long range electrostatic interactions via the site-dependent potential:

$$V_H(i) = \sum_{j\neq i}^{N} \frac{1}{2}\frac{e^2\langle n_j\rangle}{\varepsilon\,|\mathbf{R}_i-\mathbf{R}_j|} - \sum_{j_{La}}^{N_{La}} \frac{e^2}{\varepsilon\,|\mathbf{R}_i-\mathbf{R}_{j_{La}}|} \tag{5.10}$$

Where i is the index of the lattice site considered, ε is the dielectric constant, and $\langle n_j\rangle$ the electronic density computed within layered DMFT. V_i is self-consistently determined at each DMFT iteration and it controls the charge profile along the heterostructure. With this approach we obtain the charge profile and the site-resolved spectral function, reported in Fig.[5.14], in good agreement with previous results, where only electron-electron interactions were considered within a similar approach [43, 62, 61].

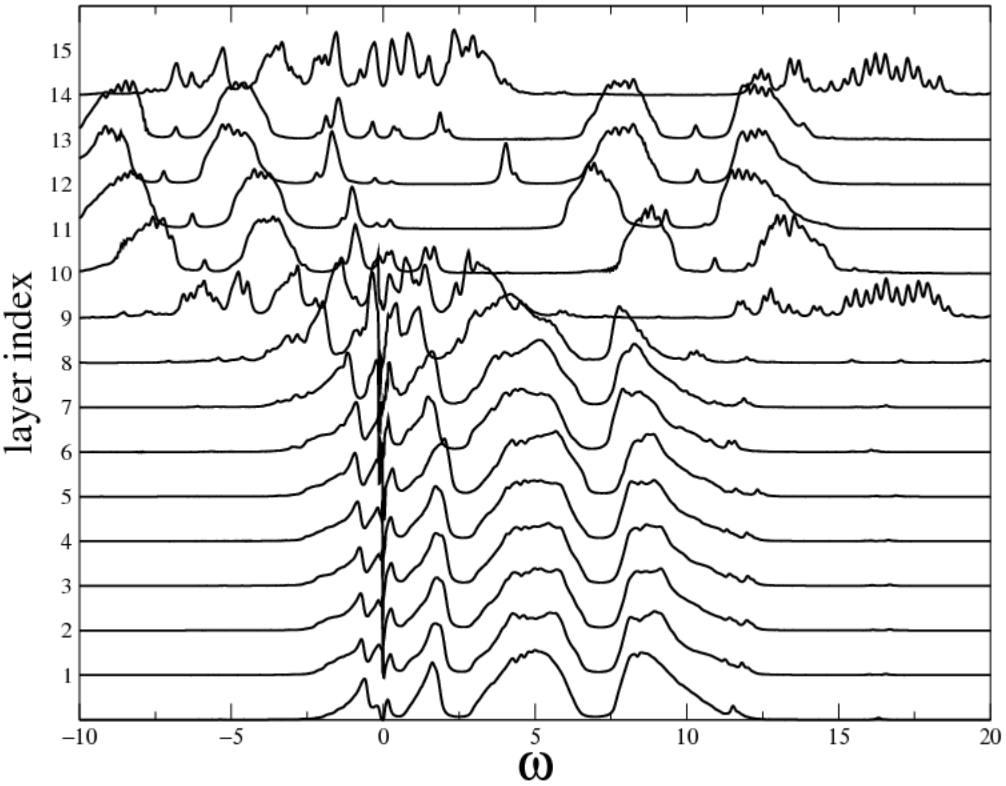

Figure 5.14: Layer-resolved spectral function calculated for 15-layer heterostructure for $U = 3D$, $\varepsilon = 20$

As other studies focused on the same phenomenology, but in a different geometry, we found that the long range potential drives the region that contains the La ions into the Mott insulating state, and leaves unaltered the system in the deep band insulator side. This result in a stable and well reproducible charge reconstruction thickness of about 3 u.c. that extends within the band insulator. In this border region the solution is a correlated low-density metal, while for sites far from the interface the spectral function is very similar in to the one obtained from a non interacting tight-binding model in a cubic lattice. On the LTO side the high Coulomb correlations results in a Mott insulating state with a charge density pinned to approximately one per site. In Fig.[5.15] we report a representative density profile where the charge depletion is evident.

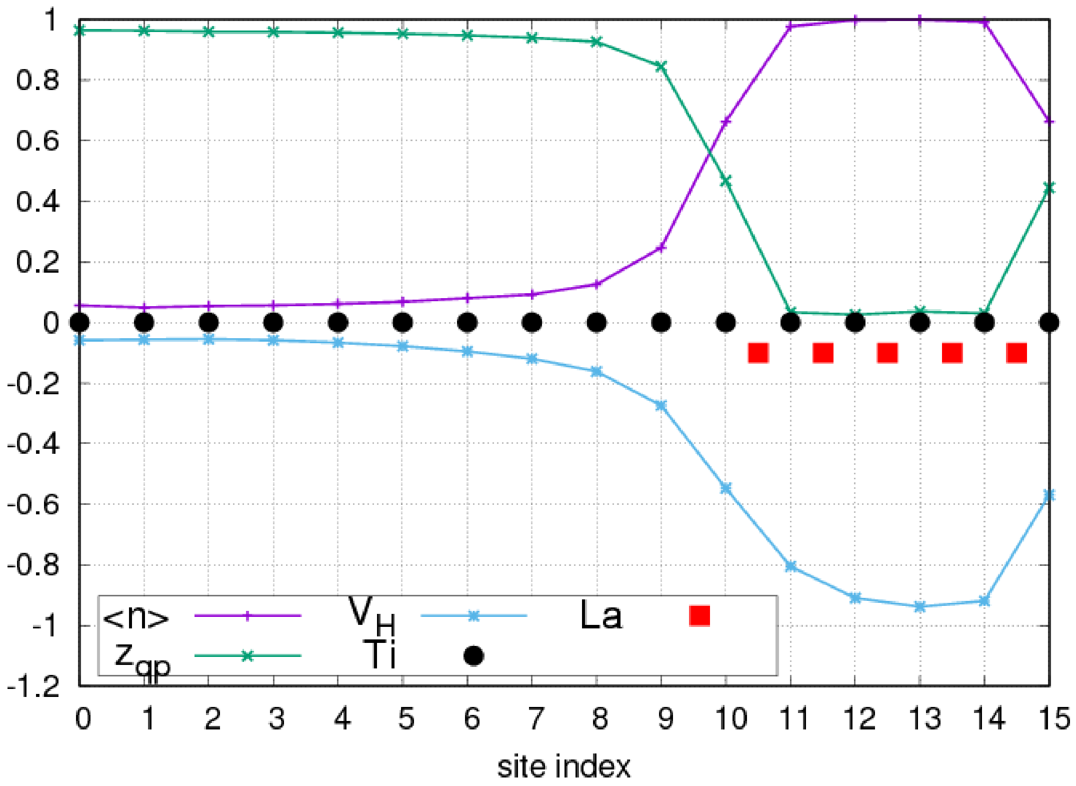

Figure 5.15: Density profile, quasiparticle weight and Hartree potential along the model heterostructure.

To include the effect of phonons we selected, as a starting point, a previously converged heterostructure, with a stable metallic region of three layers, then we adiabatically switched on the electron-phonon coupling λ in order to simplify the convergence. Upon changing λ, the density slightly rearranges so as to have a $< 10\%$ different dielectric constant in the stable configuration arising from the long-range potential. Given that in all our homogeneous calculations described in the previous sections the superconducting phase has been rarely found at $\lambda < U/D$, we considered in this first stage high values of λ.

Unfortunately, all our calculations in this direction converged with a total suppression of the superconducting order parameter for any value of λ considered. Even starting from a stable homogeneous superconductor and switching on the long-range Coulomb interaction did not provide positive results as far as superconductivity is concerned, and a purely metallic solution is found. Our results suggest that the heterostructure and its long-range interactions are actually detrimental to superconductivity with respect to the homogeneous system, in contrast with what we found for the attractive Hubbard model. However, as we mentioned above, our calculations used a particularly "severe" choice of parameters, where the same Hubbard repulsion has been used on the LTO and STO sides of the junction. Despite both oxides share a titanium atoms, it is certainly expected that the effective Coulomb interaction will be smaller on the STO side, therefore favoring superconductivity, and it might also be layered-dependent. The evaluation of this effect will be investigated in the next months.

CHAPTER

6

SPIN ORBIT COUPLING IN DOPED PEROVSKITES

In this section we will report our study of the interplay between Spin-Orbit Coupling (SOC) and $e-e$ interaction, including the Hund's coupling, in a multi-orbital model. We focus on three-fold degenerate t_{2g} orbitals in a bulk with perfect cubic symmetry as a starting point for more realistic configurations. In the case of TMO heterostructures, this is of course an oversimplified picture since, for example, it does not include the broken translational symmetry that occurs at the LAO/STO interface. The latter would manifest itself through a splitting between orbitals with a density probability distribution perpendicular to the interface (d_{zx} and d_{yz}) and the one that lies parallel to the surface (d_{xy}). For a non-interacting system with this kind of broken translational symmetry the effect of SOC is to open a gap at the $\mathbf{k}$ points where different sub-bands intersect.

Despite of this details, a general picture of the effects of $e-e$ correlation in systems with SOC at different fillings is still lacking also in the relatively simple bulk case, that, on the other hand, can be appropriate for the LTO/STO junction. Indeed, the majority of the theoretical approach to $4d$ and $5d$ compounds are focused on material-specific models at a given electronic density. The main result of this chapter is a discussion and classification of the paramagnetic solutions of the t_{2g} model with SOC for all the possible densities as a function of the Hubbard U, the ratio J_h/U and the SOC strength. In the absence of the Hund's coupling, the local SOC is responsible for a new diagonal band representation where the total angular momentum is the new conserved number. This picture has recently attracted great interest [45, 5, 50, 92]in the context of 5d systems, where the large spin-orbit coupling is expected to form local eigenstates of the total angular momentum which, in the presence of strong correlations, can order giving rise to new kind of magnetic states where the spin and orbital angular momenta are entangled. This is the case of the iridate compound Sr_2IrO_4, where, owing to the five electrons in the t_{2g} levels, one expects a half-filled $J_{eff} = 1/2$ state which can in turn be Mott localized for moderate values of the Hubbard repulsion [45].

6.1 DMFT extension to paramagnetic Spin-Orbit coupled models

As we described in Sec.(2.3) an octahedral lattice environment leads to a crystal-field splitting that separates the five d orbitals into high energy e_g and low energy t_{2g}. If the number of electrons to populate the d levels is smaller or equal to 6 only the t_{2g} levels will be occupied and we can safely neglect the high-energy e_g orbitals. The effect of SOC is to further reduce the orbital degeneracy splitting the t_{2g} manifold according to the eigenvalues of the total angular momentum $J = L + S$. This implies a low-energy quadruplet with $J = 3/2$, and an high-energy doublet with $J = 1/2$. The energy splitting is given by $\Delta_{SOC} = 3\lambda_{SOC}/2$.

We consider a simple cubic lattice with the three t_{2g} orbitals, so that the single-particle Hamiltonian reads

$$\begin{aligned} \hat{\mathcal{H}} &= \mathcal{H}(\mathbf{k}) + \mathcal{H}_{SOC} \qquad (6.1) \\ &= -2t\left[\cos(k_x) + \cos(k_y) + \cos(k_z)\right]\delta_{\alpha\beta}\delta_{\sigma\sigma'} + \lambda_{SOC}\hat{\mathbf{l}}(t_{2g}) \otimes \hat{\mathbf{S}} \end{aligned}$$

The hamiltonian of Eq.[6.1] has the following local projection:

$$\begin{aligned} \mathcal{H}^{loc} &= \sum_{\mathbf{k}} \hat{\mathcal{H}} = \lambda_{SOC}\hat{\mathbf{l}}(t_{2g}) \otimes \hat{\mathbf{S}} \\ &= \lambda_{SOC}\widehat{LS} \end{aligned}$$

the formulation of the SOC operator that we adopted is the one we discussed in Chapter 2 as written in Eq.[2.41] where we have introduced the operator Θ that diagonalizes it. Obviously, in the non interacting case, computing the spectral function starting from the diagonal Hamiltonian or diagonalize with Θ the Green's function in the spin-orbital basis would have given the same result, that we report in FIg.[6.1].

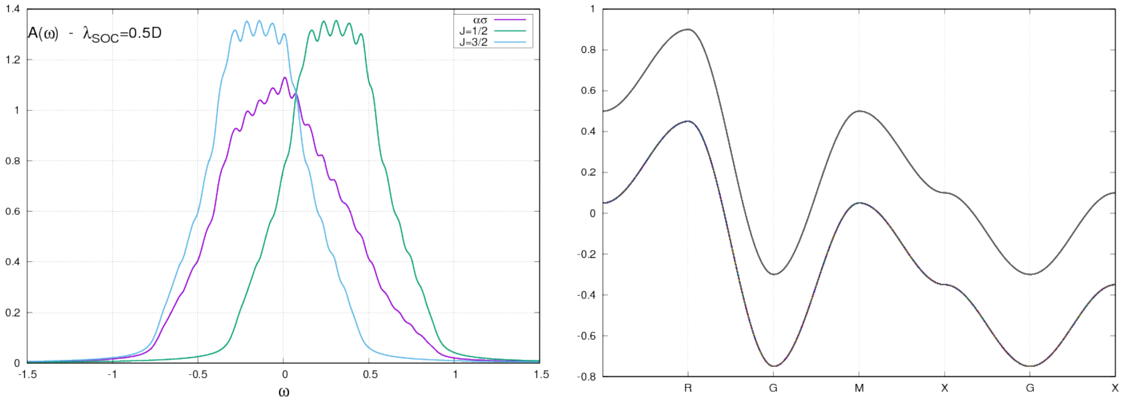

Figure 6.1: Non interacting spectral function and band dispersion of the degenerate three orbital model with SOC

In the presence of a fully rotationally invariant Hubbard interaction which controls the charge fluctuations, as it happens in the Hubbard Hamiltonian with Kanamori interaction of Eq.[2.6] when we put $J_h = 0$ and the interaction is essentially $U/2n_i^2$, where n_i is the total charge on every site, we can perform the same rotation, which leaves the interaction invariant. Therefore it is natural and straightforward to work in the basis of J and J_z, where the spin-orbit coupling acts like a crystal-field splitting.

The situation becomes much more involved when a more realistic interaction is consider, either in the full Kanamori form or in another alternative forms. In all these cases the full interaction is not invariant under the rotation Θ, which implies that the interaction has a complicated form in the basis which diagonalizes the spin-orbit. In particular, since the Hund's contribution does not commute with J, the eigenvalues of the full Hamiltonian are no longer eigenstates of J and J_z. We remind that the full Kanamori interaction is invariant with respect to the $U_C(1) \otimes SU_S(2) \otimes SO_O(3)$, i.e., under transformation that rotate independently the spin and orbital sectors. The SOC breaks this invariance since it mixes the spin and orbital indices.

This situation creates some technical difficulties to the solution of impurity models with both SOC and a non-trivial interaction. If we remain in the original orbital basis the interaction remains the familiar Kanamori term, but the single-particle Hamiltonian contains off-diagonal terms connecting different spins and orbitals. These hopping terms naturally generate off-diagonal Green's function with the same indices, which can create some problem in Continuous-Time Quantum Monte Carlo solutions of the impurity model. For this reason, most previous studies of SOC in the presence of strong correlations have used the basis which diagonalizes the non-interacting part of the Hamiltonian (J, J_z basis), but, for technical reasons have preferred to use only a density-density interaction and/or eliminated the off-diagonal interaction terms generated rotating the interaction in the new basis [5, 50]. The exact diagonalization solver does not suffer from the same limitations of the CTQMC as far as the non-diagonal Green's functions are concerned. For this reason, in our calculations we worked in the original t_{2g} orbital basis, adding an explicit non-diagonal SOC term and the familiar Kanamori interaction. As we will show in the following, we used the J, J_z basis to discuss our results, but the change of basis has been performed only at the end of the calculations.

As it has been discussed in several previous chapters, it is particularly useful in the DMFT context to consider paramagnetic solutions, in which the broken-symmetries characteristic of the problem at hand are inhibited. These solutions help us in identifying the nature of the metallic state from which the broken-symmetry solution develops and to identify the degree of correlation of the system, which is somewhat hidden in the broken-symmetry state. In the standard cases we discussed so far, implementing the paramagnetic constraint is practically very simple. In the case of antiferromagnetism, one can simply impose a single Green's function and a single Weiss field for each spin species in a way that completely forbids any spontaneous symmetry breaking. For the case of superconductivity this is even simpler as it just requires to set the anomalous Green's functions to zero. In the case of a spin-orbit coupled system, this choice can be trickier because the constraint has to be imposed in a basis different from the one where the calculations are performed and, in the presence of a finite J_h, in a basis which is not known analytically.

Let us focus, for the sake of definiteness, on the popular case of $n = 5$, where, at least in the absence of Hund's coupling, the $J = 3/2$ are completely filled and the $J = 1/2$ is half-filled. Therefore one expects a simple antiferromagnetic solution very similar to a $S = 1/2$ system, where the ordered moment is given by J, and the symmetry is broken in some direction, that we can take as the z direction. Thus, one would have an alternating pattern of states with $j_z = \pm{}^1\!/_2$ conceptually equivalent to the $S_z = \pm{}^1\!/_2$ antiferromagnet of the single band Hubbard model. For the standard $S = 1/2$ case, the method in order to avoid the antiferromagnetic solution is simply to solve the Anderson impurity model for a single spin and impose that the same behavior holds for the other spin. This condition is not so easy to enforce in the present case, however one can easily show that the two solutions with $J_z = \pm 1/2$ correspond to an impurity

Green's function with the structure

$$\hat{G}=\begin{pmatrix} G_1 & i\phi_1 & 0 & 0 & 0 & -\phi_1 \\ -i\phi_1 & G_1 & 0 & 0 & 0 & +i\phi_1 \\ 0 & 0 & G_2 & \phi_2 & -i\phi_2 & 0 \\ 0 & 0 & \phi_2 & G_2 & -i\phi_2 & 0 \\ 0 & 0 & i\phi_2 & i\phi_2 & G_2 & 0 \\ -\phi_1 & -i\phi_1 & 0 & 0 & 0 & G_1 \end{pmatrix} \tag{6.2}$$

where only four different functions fully characterize the state and to another (degenerate) solution where the indices 1 and 2 are exchanged. Then a paramagnetic solution is obtained symmetrizing the two solutions with opposite J projection, which means simply to use a single Green's function where G_1, G_2, ϕ_1 and ϕ_2 are replaced by averages

$$\begin{aligned} G\left(i\omega_n\right) &= \frac{G_1+G_2}{2} \\ \phi\left(i\omega_n\right) &= \frac{\phi_1+\phi_2}{2}. \end{aligned} \tag{6.3}$$

Leading to the paramagnetic impurity Green's function:

$$\hat{G}\left(i\omega_n\right)=\mathbf{1}G\left(i\omega_n\right)+2\phi\left(i\omega_n\right)\widehat{LS} \tag{6.4}$$

Once that the right symmetry is imposed on $\hat{G}$, all the other quantities (self-energy and Weiss field) naturally preserve the same structure, that consists of a diagonal function that represent the orbital renormalization and an off diagonal function related to the renormalization of the SOC. The self-energy is finally used to compute the local Green's function matrix:

$$\hat{G}\left(i\omega_n\right)=\frac{1}{L}\sum_{\mathbf{k}}\frac{1}{i\omega_n+\mu-\mathcal{H}\left(\mathbf{k}\right)-\mathcal{H}_{SOC}-\hat{\Sigma}\left(i\omega_n\right)} \tag{6.5}$$

the latter will be then diagonalized by the rotatation Θ leading to the diagonal spectral representation in the J basis as well as all the other relevant quantities on which our analysis is based.

6.2 Spin-Orbit Coupling and Electron Correlations in degenerate t_{2g} bands

Motivated by the fact that the majority of the studies focused on the $e-e$ correlation effects in this model have been carried out in the basis of J and J_z, we started our analysis in the case where SOC is reasonably strong, i.e. $\lambda_{SOC}=0.5D$ and $\lambda_{SOC}>J_h$, so that the above basis is at least a good starting point. This will allow us to better benchmark our results with previous literature. Before entering the discussion regarding the whole phase diagram as a function of the density and the interaction parameters, we will now briefly describe how we characterized our solutions taking, as a reference, the results for the case $J_h=0$ for each density. The calculations are done using ED as the impurity solver with $N_s=9$ total orbitals, which corresponds to a three-orbital impurity plus two replicas in the bath, which is parameterized as discussed in Sec.(3.3).

Fermi Liquid Solutions For moderate interactions, the solutions of DMFT are expected to be metalic with Fermi liquid behavior. This is signaled by a finite spectral weight at the Fermi-level accompanied by a vanishing self-energy. The Fermi-liquid behavior within DMFT can also be accessed from the imaginary-frequency Green's functions, which have to converge in the zero-frequency limit, to the same value of the non-interacting systems. In Fig.[6.2] we report our results for the case $n = 1$, which clearly show a Fermi-liquid behavior, which is expected because for this density, all the interactions besides the Hubbard U are essentially irrelevant.

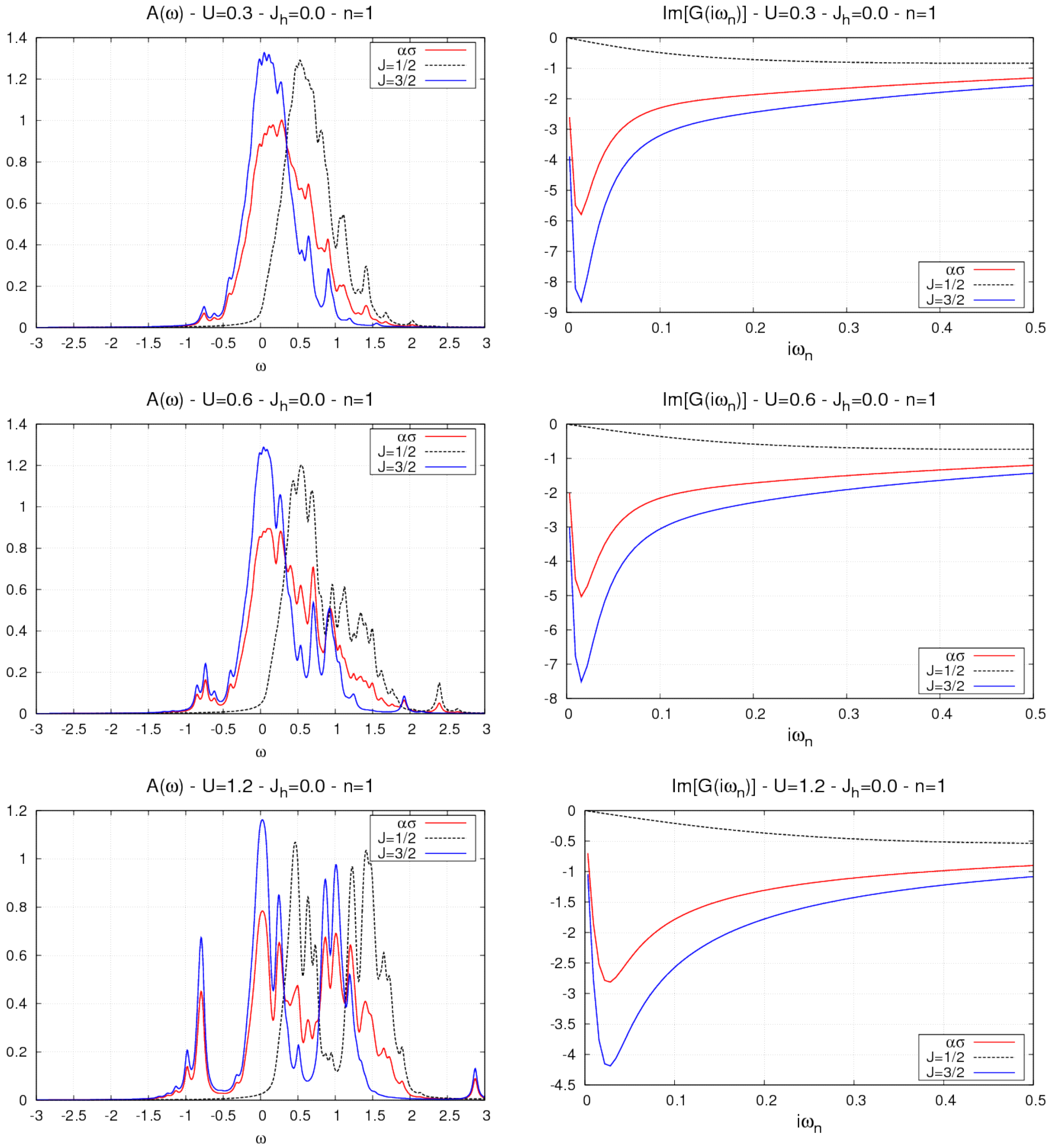

Figure 6.2: Solution for the $n = 1$ case as a function of U/D

Non Fermi-Liquid Solutions In principle, in the presence of competing interactions, the solution of the DMFT equations may depart from the Fermi-liquid prediction, giving rise to a Non-Fermi-liquid (NFL) phase. This phase is a metal with incoherent spectral weight at low energy. This is signalled by a finite value of the imaginary part of the self-energy and a deviation from the Luttinger theorem prediction of the Green's function, despite the finite value of the spectral function. We need to stress however that the present study is limited to two 9 energy levels, which means that we only have two replicas of the cluster in the bath. This might limit our ability to describe the detailed features of our solutions and it can induce spurious deviations from the FL behavior. Therefore all the reported NFL behavior we discuss in the following must be taken with a grain of salt and will be confirmed or disproved by more accurate calculations with more bath levels. With all the above caveats in mind, we mention that we found NFL behavior for both the $n = 2$ and $n = 5$ case, reported in Fig.[6.3] and Fig.[6.5].

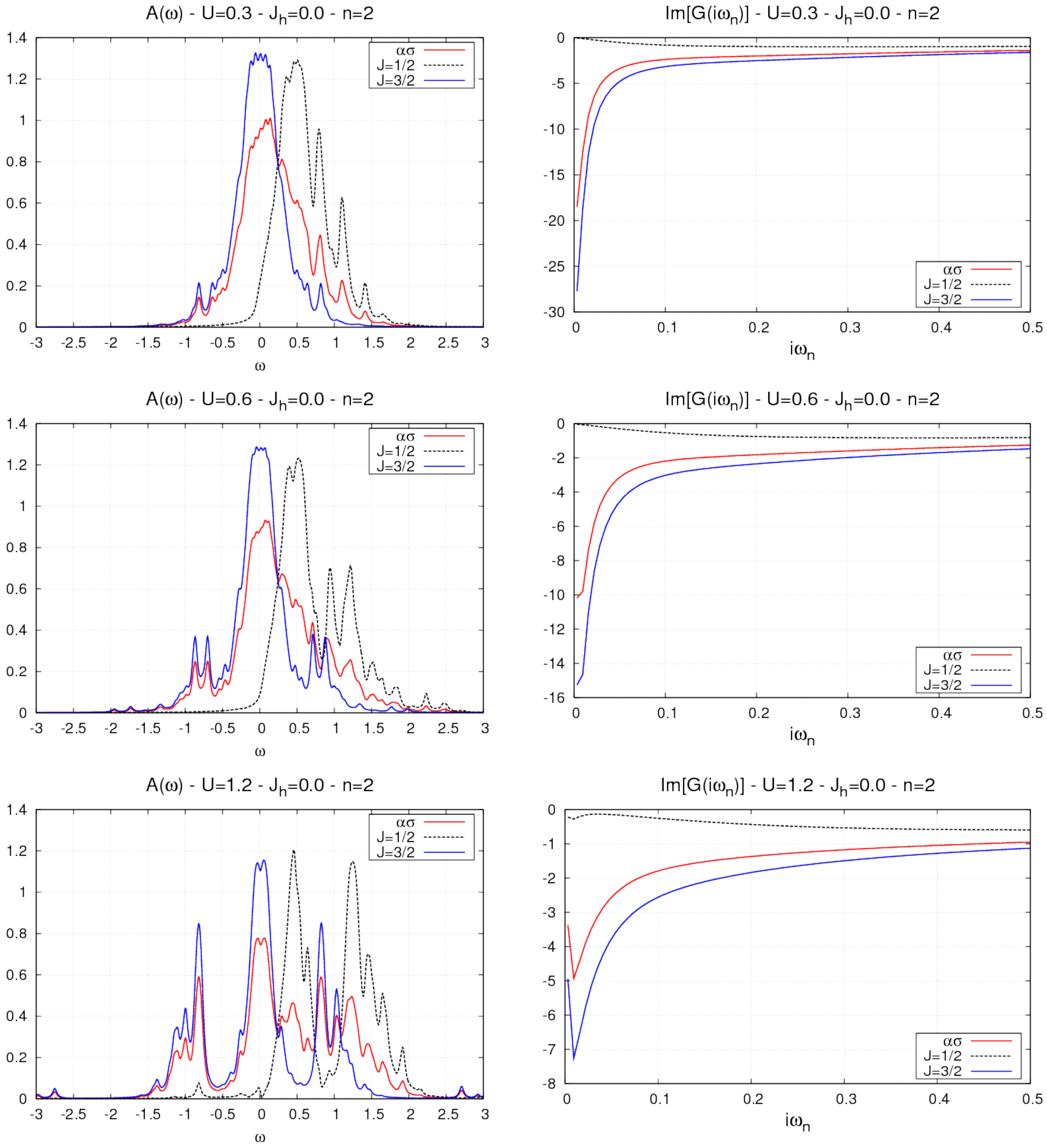

Figure 6.3: Solution for the $n = 2$ case as a function of U/D

Band insulator This is the simplest phase that can be found in the model and it correspond to the situation where the Fermi level lies within the gap induced by SOC, namely when $n = 4$. This is the only case in which we found the bands being completely non interacting but just further separated by an additional splitting of the order of U.

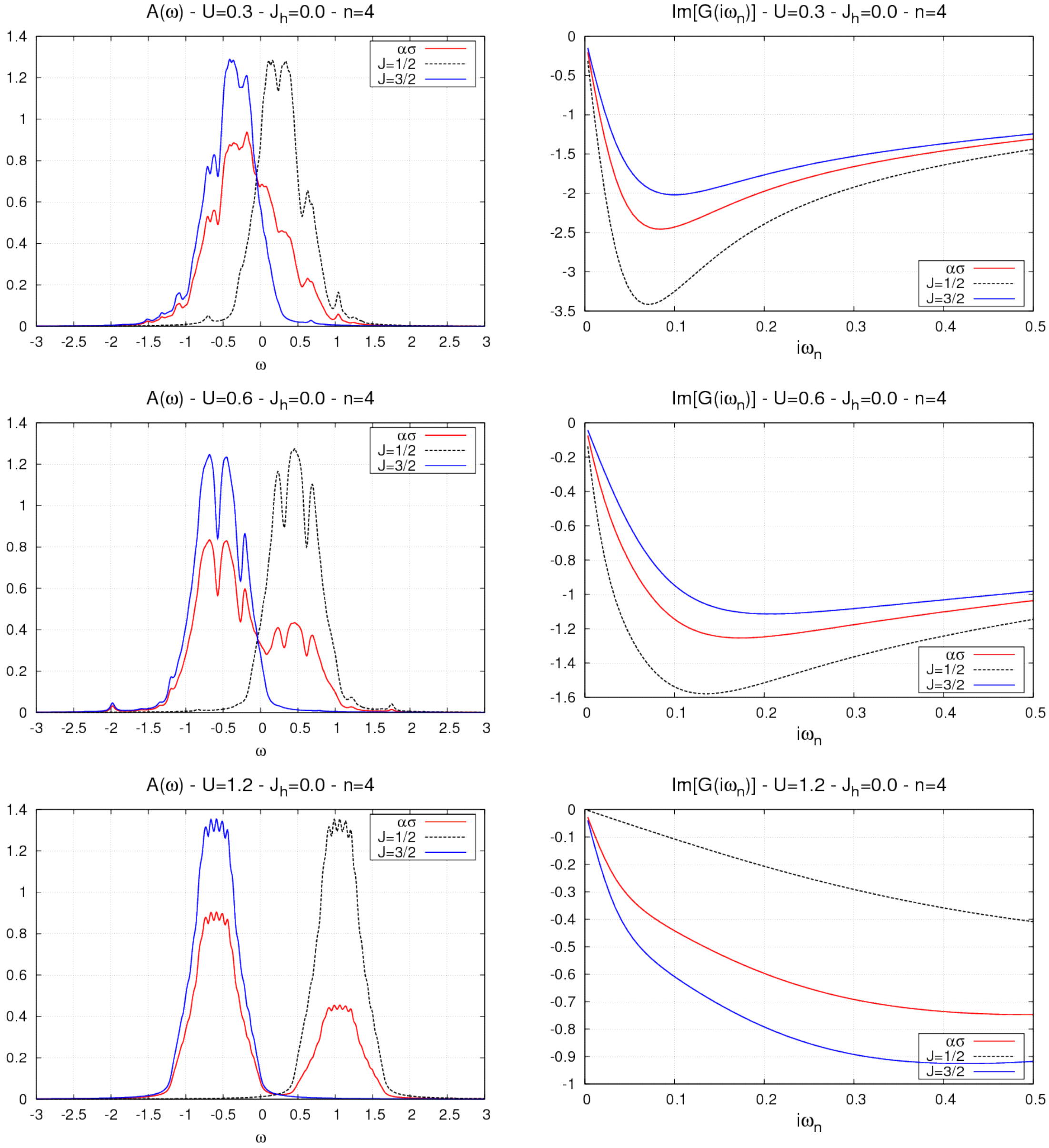

Figure 6.4: Solution for the $n = 4$ case as a function of U/D

Mott Insulator Upon increasing the Hubbard interaction the system eventually undergoes a Mott transition at a critical value of the interaction that strongly depends, at least in the $J_h = 0$ case, on the filling condition. This correspond to the absence of a quasiparticle peak and, at half filling, to a divergence of the self-energy. In Fig. [6.5] this evolution towards the Mott insulator is reported for the $n = 5$ case with an half-filled $J_{eff} = 1/2$ band being in the paramagnetic superposition of the $j_z = \pm 1/2$ solutions. The spectral function vanishes at the Fermi energy and the two high-energy structures centered around $\omega\pm = U/2$ are clearly visible thus reproducing a similar picture as that of the single-band Hubbard model.

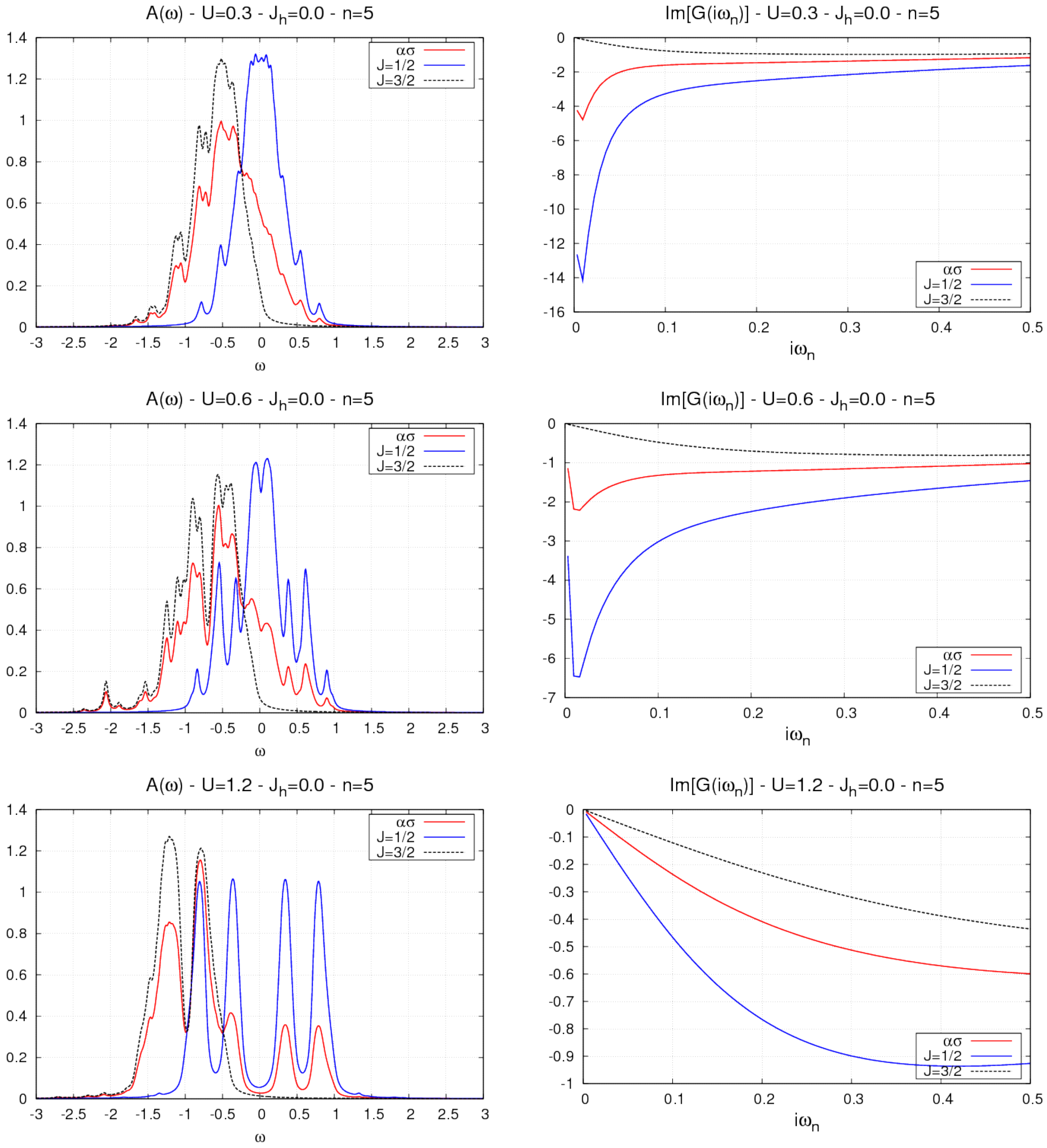

Figure 6.5: Solution for the $n = 5$ case as a function of U/D

Phase diagram for vanishing Hund's coupling We now discuss the phase diagrams obtained as a function of U for different integer densities and for fixed values of the SOC. We start from the case $J_h = 0$. In this case we expect to reproduce the results of a three-band Hubbard model with a crystal-field splitting which shifts one of the three levels above the two others, which remain degenerate. In Fig.[6.6] we report the phase diagram for integer densities with a SOC given by $\lambda_{SOC} = 0.5D$, as a function of the Hubbard interaction U/D.

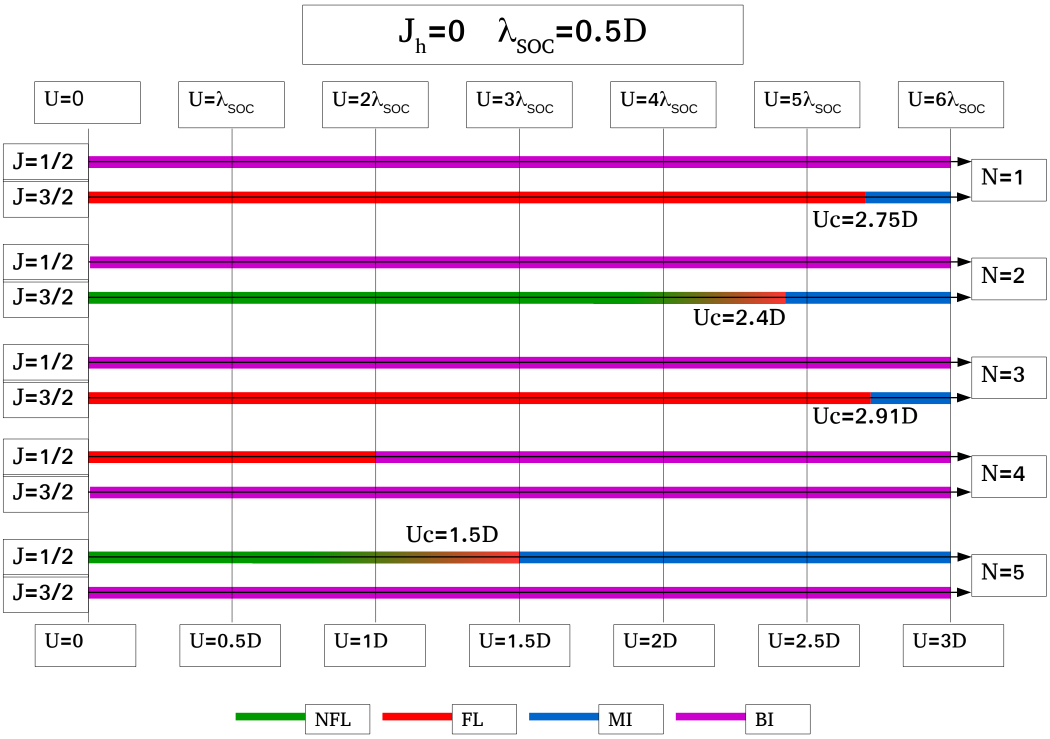

Figure 6.6: Phase diagram of the three orbital model in the $J_h = 0$ case as a function of the Hubbard interaction and electron density in the diagonal basis.

The first thing that we notice in this rich phase diagram is the sharp distinction between the $n = 1, 2, 3$ and 4, which correspond to a partial (or total) filling of the $J_{eff} = 3/2$ band and $n = 5$ case, corresponding to the half-filling condition in the $J_{eff} = 1/2$ band. This distinction is however rigorous only in the limit of very large spin-orbit coupling. Here we use a rather large value, such that the full splitting is $3/4$ of the bare bandwidth. This leads however to some interesting features. The critical value of $U_c = 2.4D$ for the $n = 2$ case is quite close to the estimates for a half-filled two fold degenerate Hubbard model. This is of course not surprising and we can attribute the deviations to the finite value of the SOC-driven splitting. The results for the $n = 1$ and $n = 3$ give rise to two Mott transitions which would be completely identical for a single two-fold degenerate band exotic and essentially consists in a doped $J_{eff} = 3/2$ band, hence with a metallic solution stable up to higher value of U_c. The discrepancy between the two value might be ascribed to a mixing of the $J_{eff} = 3/2$ electrons with the upper empty band in the $n = 3$ case. The value of the critical interaction is also compatible with estimates for two-orbital models. While in the case $n = 4$ we have a simple evolution from a metal for small U, when the two bands are partially filled because the crystal-field splitting is not sufficient to completely populate the $J_{eff} = 3/2$ band, to a band insulator at larger U, where the effective crystal-field splitting is sufficient to completely polarize the occupation. On the other hand, we find a relatively small value of the critical U in the case $n = 5$ with respect to the single-band model estimate. We can not exclude that part of the discrepancy is due to our numerical method, but we stress again that in principle the $J_{eff} = 1/2$ picture is only approximate if the splitting induced by the SOC does not clearly exceed the bandwidth. With these preliminary results we would suggest that the general tendency to enhance the effect of correlation is a direct consequence of the SOC rather than associated to a reduced bandwidth. In this sense, the usual picture in which the small U_c of the $n = 5$ strontium iridate is ascribed only to the reduced bandwidth of the $J_{eff} = 1/2$ band might not be completely correct.

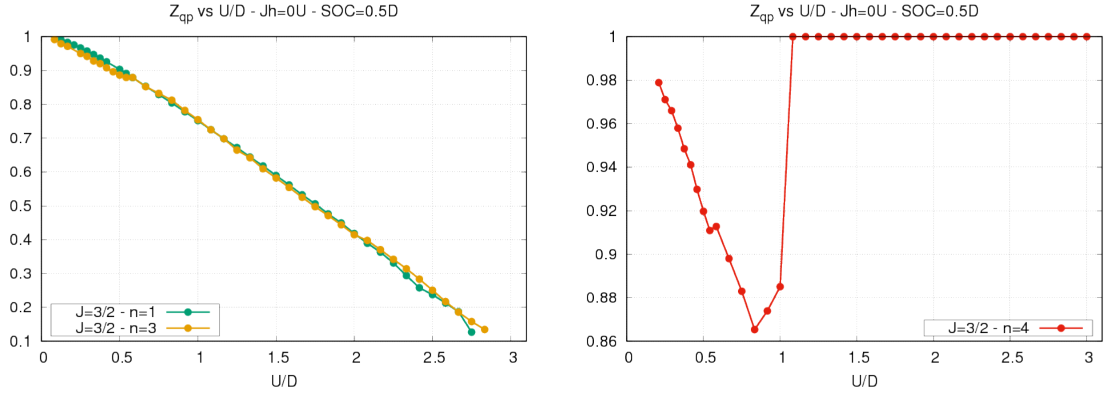

Figure 6.7: Quasiparticle weight as a function of the Hubbard interaction in the FL phases found.

In Fig.[6.7] the quasiparticle weight for the metallic solutions in the different cases. We find clearly a FL solution before the Mott transition only for $n = 1$ and $n = 3$ where the only populated band is that with $J_{eff} = 3/2$ band. The z_{qp} behavior confirms that $n = 1$ and $n = 3$ are almost symmetric around $n = 2$, with a small difference which is ascribed to the fact that in the case $n = 3$ we expect to have a little larger admixture with the $J_{eff} = 1/2$ band because of the larger occupation of the $J_{eff} = 3/2$ manifold. In the right panel we show the results for $n = 4$, where z_{qp} is one in the band insulator and very close to it in the metallic region.

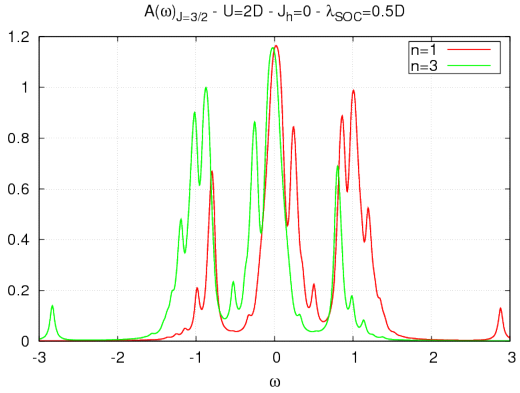

Figure 6.8: Particle-hole symmetry between the $n = 1$ and $n = 3$ densities of the $J_{eff} = 3/2$ band

Fig.[6.8] shows, as a further support to be above picture for the $n = 1$ and $n = 3$ cases, that the $J_{eff} = 3/2$ spectrals weight of the $n = 1$ and $n = 3$ cases are essentially equal under a particle-hole transofrmation.

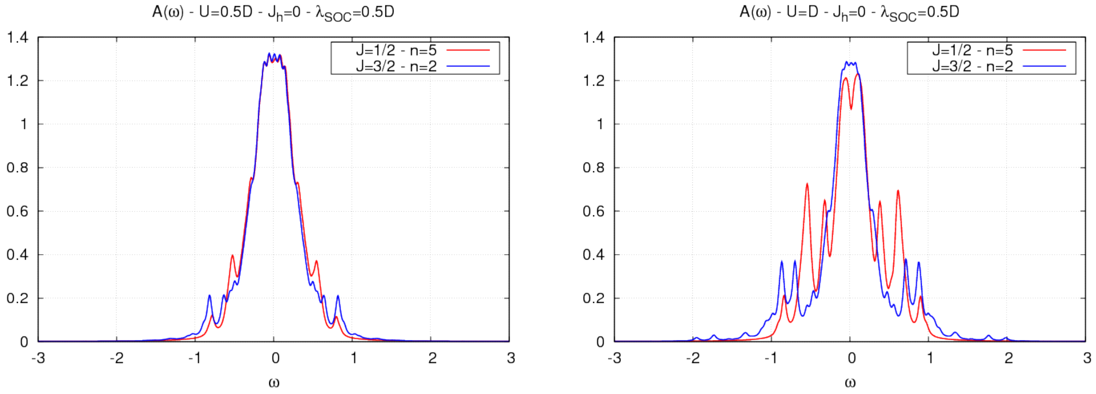

Figure 6.9: Effect of correlation in the half-filled active bands.

In Fig.[6.9] we show that the low energy spectral function of the the half-filled active bands, i.e. $n = 2$ for $J_{eff} = 3/2$ and $n = 5$ for $J_{eff} = 1/2$, is essentially the same for moderate values of U, while they evolve differently upon increasing U/D. This probably supports the general idea that the enhanced correlations, accountable for the lowering of U_c in the $J_{eff} = 1/2$ band, are due to the specific presence of SOC rather than to a reduced bandwidth.

6.2.1 Phase diagram for finite Hund's coupling

We now move to the fate of the phase transitions we discussed when a finite Hund's coupling is considered. In recent papers [25] it has been pointed out that Hund's coupling deeply influences the Mott transition strongly modifying the critical value of the Mott transition in a way which depends critically on the number of electrons. The key point is the reduced groundstate degeneracy induced by the fact that J_h favors high-spin configurations. In degenerate t_{2g} orbital without SOC J_h strongly favors the Mott insulating state in the half-filled configuration reducing the critical U, while in the other integer fillings the critical U is shifted to larger values of the interaction revealing the region which is usually called a Hund's metal. For all the densities, the metallic coherence is reduced by the Hund's coupling.

The interplay between this physics, which is based on the energetic advantage of high-spin configurations, and the SOC coupling, which favors the formation of eigenstates of J has not been discussed with the same detail. In Fig.[6.10] and Fig.[6.11] the phase diagram for $J_h = 0.15U$ and $J_h = 0.25U$ is reported using the same format we used for the previous case.

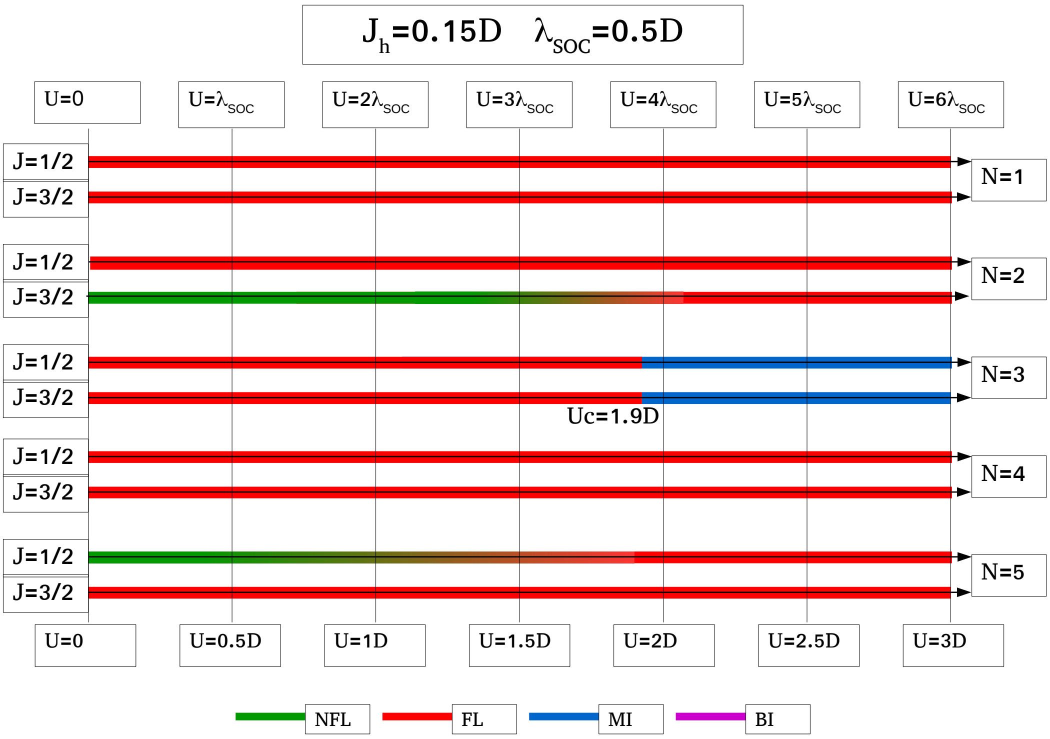

Figure 6.10: Phase diagram of the three orbital model in the $J_h = 0.15D$ case as a function of the Hubbard interaction and electron density in the diagonal basis.

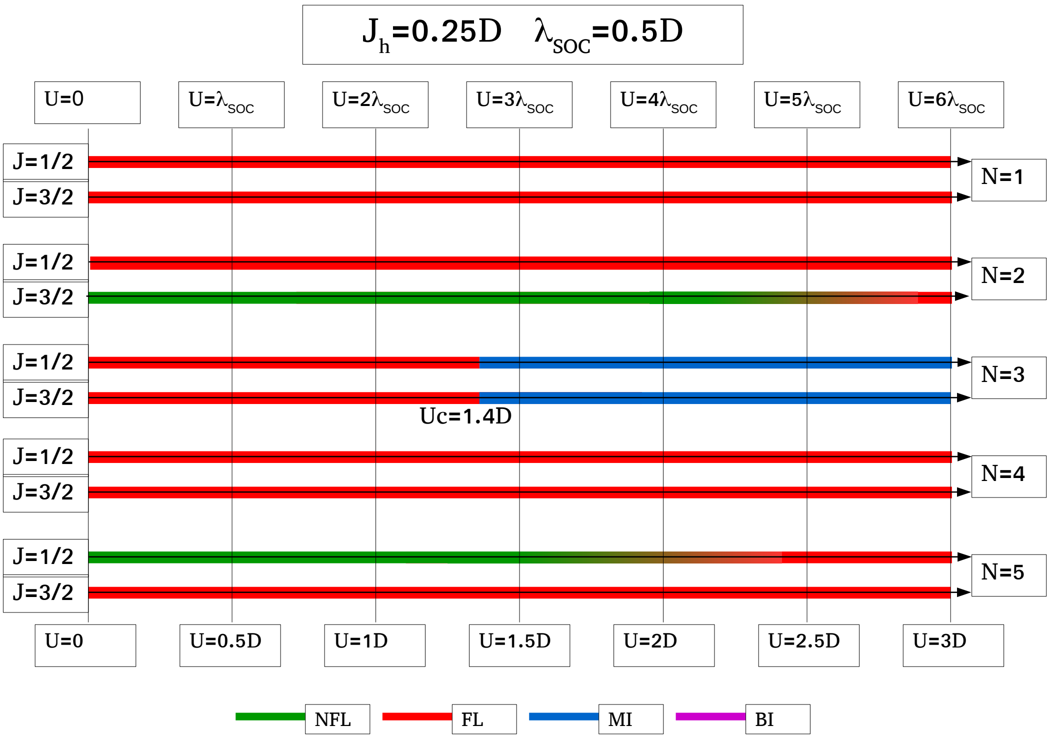

Figure 6.11: Phase diagram of the three orbital model in the $J_h = 0.25D$ case as a function of the Hubbard interaction and electron density in the diagonal basis.

It is clear at a first sight that the effect of the Hund's coupling changes substantially the picture, even when its value is smaller than the spin-orbit coupling strength. We observe in fact that the NFL phase extends in a wider region and the Mott insulator is shifted to values larger than those we considered for all the densities different from $n = 3$. Moreover the critical U_c in the *global* half-filling case decreases with J_h , in agreement with the results in the absence of SOC that we just reviewed.

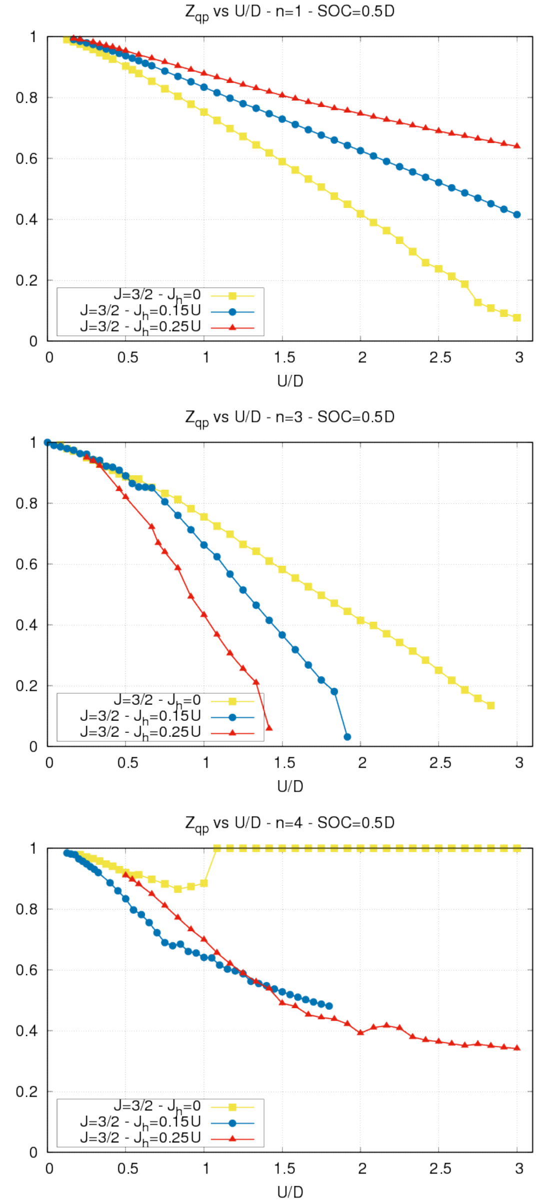

Figure 6.12: Quasiparticle peaks in the FL bands for various values of the Hund's coupling.

In order to check the limits and validity of this parallelism we plot in Fig.[6.12] the spectral weight as a function of U for all the available densities. We see that, in the $n = 1$ case, the result on the $J_{eff} = 3/2$ is to progressively become more screened with respect of the $e-e$ interaction, resulting in a greater U_c. When the system contains $n = 3$ electrons even a small J_h is able to counteract the splitting between the bands with different value of J_{eff} and mix them. As a result the critical U_c for the Mott transition is further reduced. For $n = 4$, the Hund's coupling has the the opposite effect with the onset of a long tail in z_{qp} which is associated to the fact that the Hund's coupling inhibits the polarization between the two bands. Therefore we have two partially filled bands which experience some correlation effects, instead of the band insulator we find for $J_h = 0$. We do not show data for the quasiparticle weight for the $n = 2$ and $n = 5$ densities since in the NFL phase it is not possible to define an equivalent of z_{qp}.

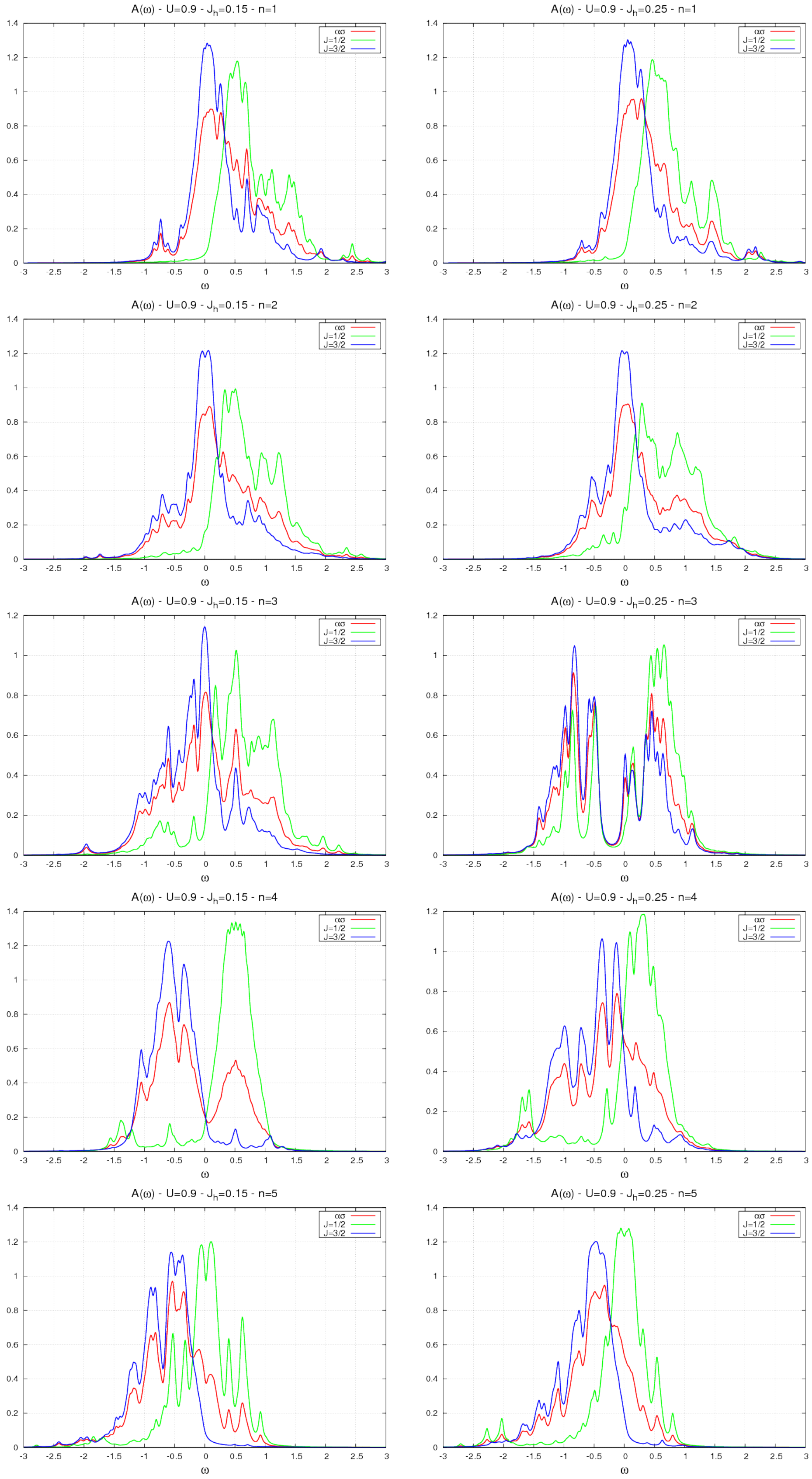

Figure 6.13: Effect of Hund's coupling for all the avalable densities at $U/D = 1.5$

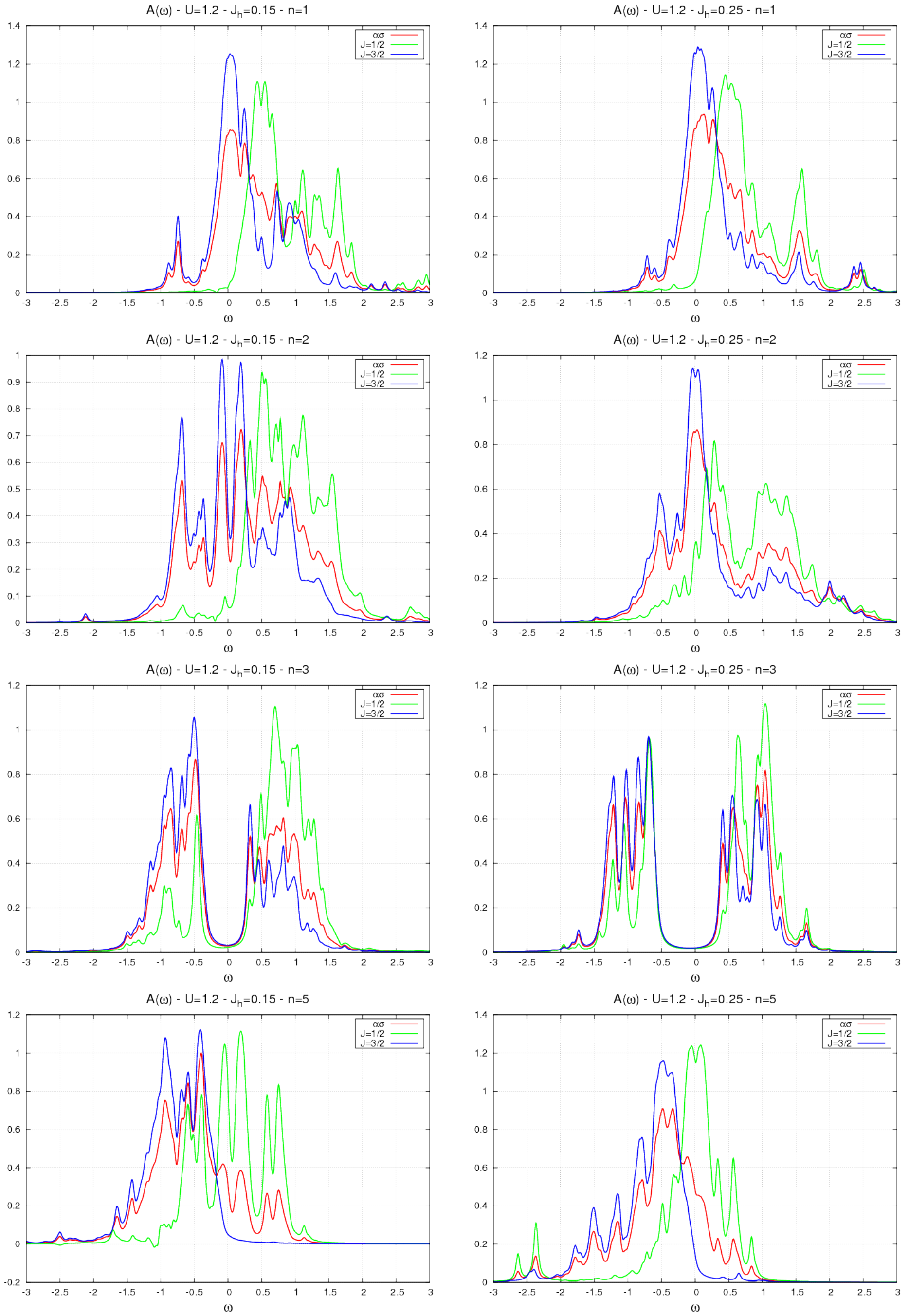

Figure 6.14: Effect of Hund's coupling for all the avalable densities at $U/D = 2$

Finally in Fig.[6.13] and Fig.[6.14] we plot the spectral functions for two representative values of the interactions comparing, for every integer filling, the results for two different values of J_h. Upon increasing J_h the diagonal bands which are formed without the Hund's coupling progressively merge one into the other. The effect appears to be quantitatively stronger at $n = 3$. This proves that, for $J_h > 0$, the interacting system is not diagonal in the J_{eff} basis. Therefore implying that, in principle, we cannot describe the system as a effective $J = 1/2$ system. We also notice that in this case, our reciept to impose a paramagnetic solution is not as motivated as in the $J_h = 0$ case.

As a matter of fact, the result of our "wrong" rotation is to bring the system in a mixed basis representation, where, for any value of the interaction, all the bands are partially filled. The overall rough picture that we can draw with the available data, remains within the known "Janus-faced" mechanism with an additional apparent NFL phase that persists and even expands for densities reminiscent of the integer fillings for the J_{eff} bands. We can not quantify this statement completely because we are not allowed to estimate z_{qp} in the NFL phase, yet the increasing of U_c at $n = 1$, his decreasing at the global half-filling density $n = 3$ and the intermediate behavior at $n = 4$, are clues that make us confident in the reliability of our picture.

The next steps of this investigation will use a larger number of bath sites in the Ed scheme in order to confirm the presence of the NFL phase. Another rather obvious aspect to explore is to pinpoint the position of the Mott transition for $n = 1$ and $n = 3$, which lies outside the region we explored here. The DMFT results could be compared with estimates based on an atomic picture. We will also focus on the more involved case of $\lambda_{SOC} < J_h$ where the picture of two degenerate bands well separated from the third one does not hold anymore. In this case the third Hund's rule should be obeyed.

6.3 Antiferromagnetic solution for Sr_2IrO_4

In this final section we present some results on an actual material, the celebrated Sr_2IrO_4, which has been proposed as a material realization of a $J_{eff} = 1/2$ Mott insulator [45]. In order to reproduce the low-temperature physics of this compound there is no need to symmetrize the solutions to obtain a paramagnet and we can safely allow the system to relax in the solution that minimizes its energy. In particular we do not assume any particular basis where the magnetic ordering has to appear and we simply work in the original orbital basis keeping all the interaction terms. In this case we abandon a model point of view and we obtain the single-particle Hamiltonian from density-functional theory using the Perdew-Burke-Ernzerhof recipe for the generalized-gradient approximation. The bandstructure includes the spin-orbit coupling. The spin-orbit splitting is estimated around $190meV$. A set of maximally localized Wannier orbitals is obtained from the bandstructure using Wannier90.

This Iridium compound has not a perfect cubic symmetry, but has tilted octahedra within the planes [89] that forced us to include eight sites in the unit cell and, more importantly in the DMFT cell. This means that in principle we have eight different self-energies for the eight inequivalent atoms. All the sites are considered as different multi-orbital impurities coupled through the non local hopping terms coming from the DFT calculations. In practice this is another application of the inhomogeneous DMFT scheme. The interaction strength that we considered are [5] $U = 2.3$ and $J_h = 0.15$.

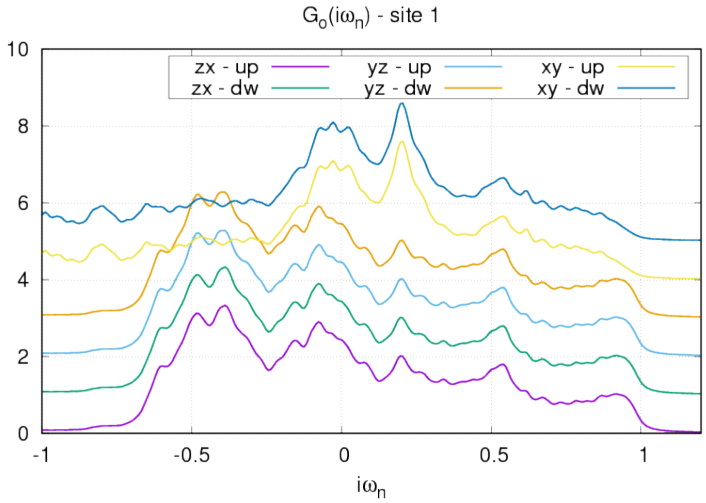

Figure 6.15: Diagonal component of the non interacting Green's function of Sr_2IrO_3

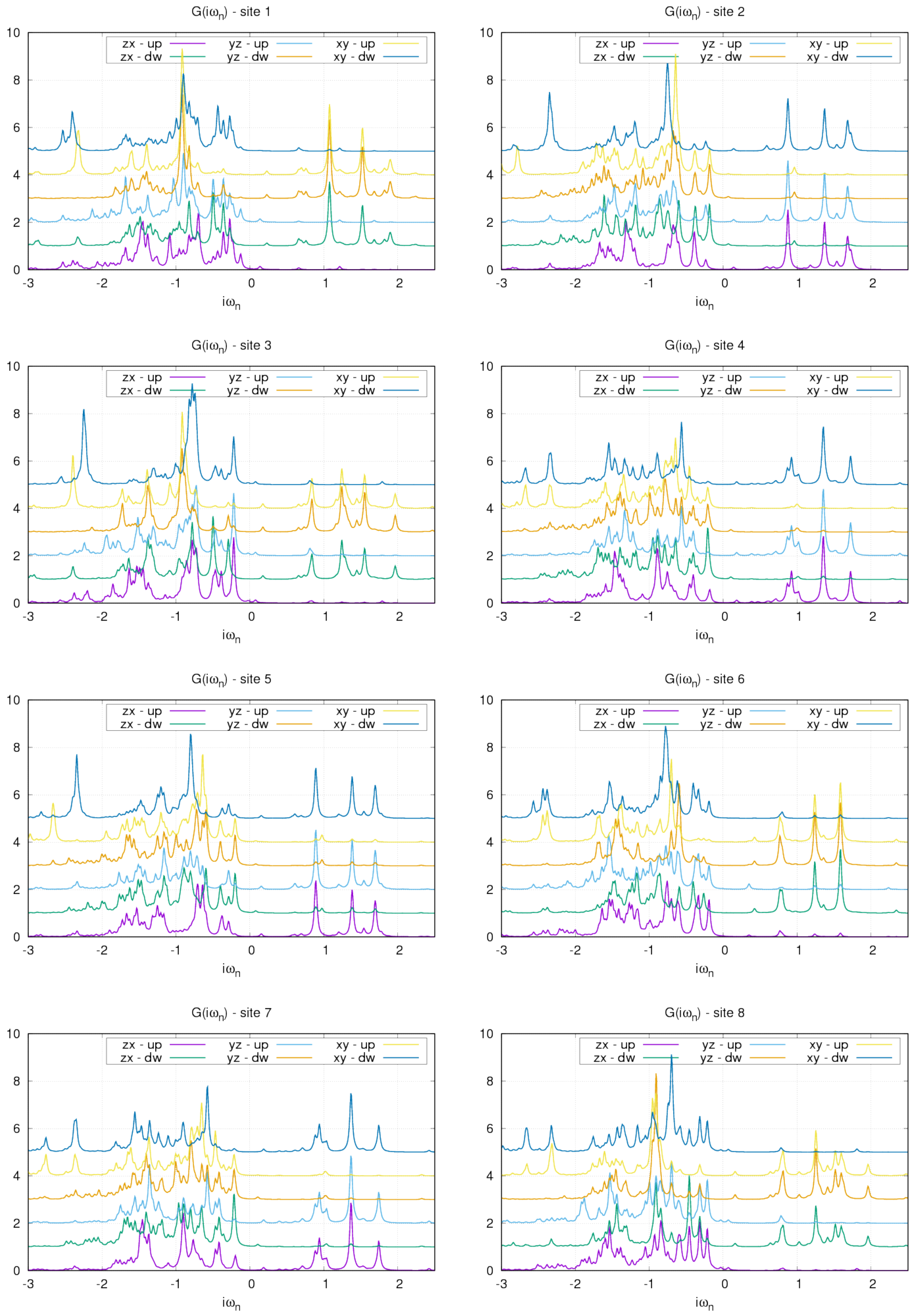
G($i\omega_n$) - site 1

G($i\omega_n$) - site 2

G($i\omega_n$) - site 3

G($i\omega_n$) - site 4

G($i\omega_n$) - site 5

G($i\omega_n$) - site 6

G($i\omega_n$) - site 7

G($i\omega_n$) - site 8

Figure 6.16: Diagonal component of the interacting Green's function of Sr_2IrO_3 for the different sites

In Fig.[6.15] and Fig.[6.16] are reported the diagonal component of the non interacting and interacting Green's function versus the site index. It is interesting to observe that, despite we did not impose any symmetry in the present calculation and the Hund's coupling is not negligible, we have essentially two sets of local Green's functions which nicely follow the structure of Eq.[6.2], which in turn corresponded to $J_z = \pm 1/2$. This strongly suggest that the $J_{eff} = 1/2$ picture seems to be closely realized in this material, at least in the antiferromagnetic phase. Computing the expectation of the operator $\hat{j}_z$ one indeed obtains a values oscillating between ± 0.45 as in Fig.[6.17] in an almost perferct $\hat{j}_z$−antiferromagnetic ordering.

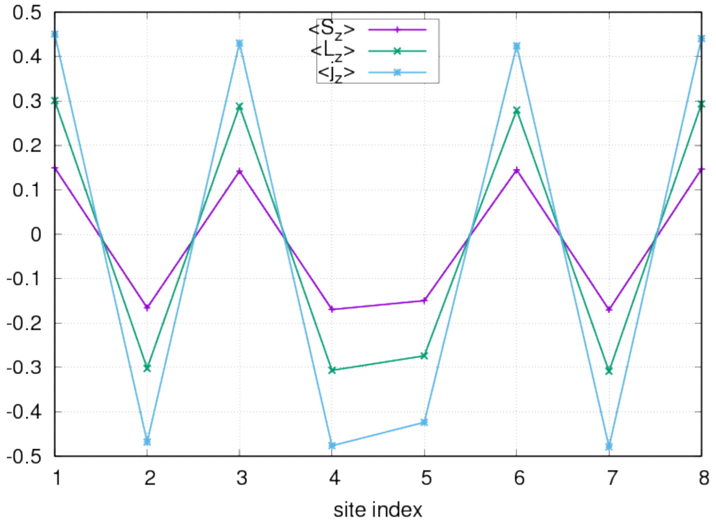

Figure 6.17: Expectation values of the z-component of the spin, angular momentum and total momentum operators.

CHAPTER

7

CONCLUSIONS

This work has been devoted to the study of the combined effects of different interactions in layered heterostuctures composed by correlated transition-metal oxides. Among these, a central role is played by the stabilization of a metallic two-dimensional high-mobility electron gas at the interface between two bulk insulator. The case which attracts more interest is probably LTO/STO, an interface between a band and a Mott insulator where the conducting sheet originates from a charge depletion/accumulation process. A full description of the phenomena occurring at these interfaces is a formidable theoretical problem which requires to include the strong correlation effects characteristic of transition-metal oxides, including the Hund's coupling which immediately plays a role when more than one orbital must be considered and the geometrical structure of the heterostructure, which obviously plays a major role. Moreover, electron-phonon coupling is believed to play a major role in these systems and it is a likely candidate for the microscopic mechanism behind the interface superconductivity. Finally, spin-orbit coupling is active at the interfaces and it give rise to a subtle interplay with the correlation effects and the electron-phonon interaction.

In this thesis we made several steps towards a theoretical description of these systems in the framework of Dynamical Mean-Field Theory. This approach is particularly suited to handle several interactions at the same time without assuming any hierarchy, even if it has the limitation to freeze spatial fluctuation. The limitation can be overcome by using inhomogeneous extension of DMFT as the one we implement in the present work. The main contributions of this present work have been

- We implemented a generalization of DMFT to layered superconductors. The necessity of an inhomogeneous extension arises when the translational symmetry is broken, which is precisely the situations related of heterostructures. The fundamental idea of this inhomogeneous extension is the mapping of the lattice model into a finite minimal number of inequivalent sites connected through a self-consistency condition. However, this implies to use a finite system, in our case a finite number of layers. The effect of the finiteness can be limited using an embedding potential which has been previously proposed and that we extended to superconductors.

Moreover we introduced a novel “feedback” effects of the finite system onto the embedding potential which further reduces the finite-size effect. This makes our approach sufficiently accurate to study tiny superconducting amplitudes as the ones observed in the actual heterostructures.

- We tested the approach for a simple attractive Hubbard model solving for different superconductor/superconductor and superconductor/metal junctions, and we found important proximity effects in both cases. We observed that different observables have different size and extension of proximity effects. To single-out the effect of the coupling strength we froze charge fluctuations.

- We stuedied the conditions for an s-wave superconducting phase to establish in a system subject to a strong Hubbard-like repulsion. Before considering a reasonably realistic description of a Mott/band insulator junction, we considered the Holstein-Hubbard model in a uniform system. In this model a Hubbard repulsion competes with a local electron-phonon coupling and we have found, besides other results that at half-filling or close to it superconductivity can only be realized when the strength on the electron-phonon coupling exceeed the Coulomb repulsion, but at low densities a novel superconducting dome establishes and it becomes quite large in the case of large repulsion.

  Encouraged by model results, we combined our theoretical description of heterostructures with the coupling of the interactions studying a Mott/band insulator heterostructure in the presence of al electrostatic repulsion which accounts for the charge redistribution. Unfortunately the first results do not lead to superconductivity at the interface. A possible reason is that we took the rather extreme view to use the same repulsion on the Mott and band insulating sides, and a more screened Coulomb repulsion on the band-insulating side may definitely revive the superconducting phase.

- We studied the interplay between spin-orbit coupling and electronic correlations in a three-fold degenerate model with Hund's coupling. Using Exact Diagonalization as an impurity solver we can work in the basis of the original orbitals without assuming that the system is diagonalized by the transformation that diagonalizes the spin-orbit coupling. We study the evolution of the electronic properties in the paramagnetic state for a number of parameters discussing the Mott transitions for all the different integer fillings as a function of both the spin-orbit coupling strength and the Hund's coupling.

  Finally we study the magnetic phase of Sr_2IrO_4 using a DMFT in combination with density-functional theory. Our results show an ordering of the global angular moment in agreement with expectations and experiments.

  The results obtained during the thesis lay the foundations of future studies in which we will be able to combine all the above effects briding the gap between the experimental advances and our –still limited– understanding of the exciting phenomena occurring at interfaces. The next step to be taken will include the study of heterostructuring in iridates and a more realistic description of LTO/STO interfaces.

BIBLIOGRAPHY

[1] Lev Gor′kov Aleksej Alekseevic Abrikosov. Methods of quantum field theory in statistical physics.

[2] A. Alexandrov and J. Ranninger. Theory of bipolarons and bipolaronic bands. *Phys. Rev. B*, 23:1796–1801, Feb 1981.

[3] S Altieri, L. H Tjeng, and G. A Sawatzky. Ultrathin oxide films on metals: new physics and new chemistry? 400(1):9–15.

[4] S Altieri, L.H Tjeng, and G.A Sawatzky. Ultrathin oxide films on metals: new physics and new chemistry? *Thin Solid Films*, 400(1 - 2):9 – 15, 2001. Proceedings of Symposium N on Ultrathin Oxides.

[5] R. Arita, J. Kuneš, A. V. Kozhevnikov, A. G. Eguiluz, and M. Imada. *Ab initio* studies on the interplay between spin-orbit interaction and coulomb correlation in $\mathrm{Sr_2IrO_4}$ and $\mathrm{Ba_2IrO_4}$. *Phys. Rev. Lett.*, 108:086403, Feb 2012.

[6] Yu. S. Barash, A. V. Galaktionov, and A. D. Zaikin. Charge transport in junctions between d -wave superconductors. *Phys. Rev. B*, 52:665–682, Jul 1995.

[7] M. Ben Shalom, M. Sachs, D. Rakhmilevitch, A. Palevski, and Y. Dagan. Tuning spin-orbit coupling and superconductivity at the $\mathrm{srtio_3/laalo_3}$ interface: A magnetotransport study. *Phys. Rev. Lett.*, 104:126802, Mar 2010.

[8] Patrizia Benedetti and Roland Zeyher. Holstein model in infinite dimensions at half-filling. *Phys. Rev. B*, 58:14320–14334, Dec 1998.

[9] J. Biscaras, N. Bergeal, S. Hurand, C. Grossetête, A. Rastogi, R. C. Budhani, D. LeBoeuf, C. Proust, and J. Lesueur. Two-dimensional superconducting phase in $\mathrm{latio_3/srtio_3}$ heterostructures induced by high-mobility carrier doping. *Phys. Rev. Lett.*, 108:247004, Jun 2012.

[10] J. Biscaras, N. Bergeal, A. Kushwaha, T. Wolf, A. Rastogi, R.C. Budhani, and J. Lesueur. Two-dimensional superconductivity at a mott insulator/band insulator interface latio$_3$/srtio$_3$. *Nat. Commun.*, 1:89, Oct 2010.

[11] Amlan Biswas, M. Rajeswari, R. C. Srivastava, Y. H. Li, T. Venkatesan, R. L. Greene, and A. J. Millis. Two-phase behavior in strained thin films of hole-doped manganites. 61(14):9665–9668.

[12] Amlan Biswas, M. Rajeswari, R. C. Srivastava, T. Venkatesan, R. L. Greene, Q. Lu, A. L. de Lozanne, and A. J. Millis. Strain-driven charge-ordered state in $\mathrm{La}_{0.67}\mathrm{Ca}_{0.33}\mathrm{MnO}_3$. 63(18):184424.

[13] Hans Boschker, Christoph Richter, Evangelos Fillis-Tsirakis, Christof W. Schneider, and Jochen Mannhart. Electron - phonon coupling and the superconducting phase diagram of the LaAlO3 / SrTiO3 interface. 5:12309.

[14] Michel Caffarel and Werner Krauth. Exact diagonalization approach to correlated fermions in infinite dimensions: Mott transition and superconductivity. *Phys. Rev. Lett.*, 72:1545–1548, Mar 1994.

[15] C. Cancellieri, A. S. Mishchenko, U. Aschauer, A. Filippetti, C. Faber, O. S. Barisic, V. A. Rogalev, T. Schmitt, N. Nagaosa, and V. N. Strocov. Polaronic metal state at the LaAlO3/SrTiO3 interface. 7:10386.

[16] M. Capone, P. Carta, and S. Ciuchi. Dynamical mean field theory of polarons and bipolarons in the half-filled holstein model. *Phys. Rev. B*, 74:045106, Jul 2006.

[17] M. Capone and S. Ciuchi. Polaron crossover and bipolaronic metal-insulator transition in the half-filled holstein model. *Phys. Rev. Lett.*, 91:186405, Oct 2003.

[18] M. Capone, M. Fabrizio, C. Castellani, and E. Tosatti. Strongly correlated superconductivity. 296(5577):2364–2366.

[19] Massimo Capone, Luca de' Medici, and Antoine Georges. Solving the dynamical mean-field theory at very low temperatures using the lanczos exact diagonalization. *Phys. Rev. B*, 76:245116, Dec 2007.

[20] Massimo Capone, Michele Fabrizio, Claudio Castellani, and Erio Tosatti. *Colloquium* : Modeling the unconventional superconducting properties of expanded A_3c_{60} fullerides. *Rev. Mod. Phys.*, 81:943–958, Jun 2009.

[21] A. D. Caviglia, M. Gabay, S. Gariglio, N. Reyren, C. Cancellieri, and J.-M. Triscone. Tunable rashba spin-orbit interaction at oxide interfaces. *Phys. Rev. Lett.*, 104:126803, Mar 2010.

[22] O. Copie, V. Garcia, C. Bödefeld, C. Carrétéro, M. Bibes, G. Herranz, E. Jacquet, J.-L. Maurice, B. Vinter, S. Fusil, K. Bouzehouane, H. Jaffrès, and A. Barthélémy. Towards two-dimensional metallic behavior at $\mathrm{LaAlO_3SrTiO_3}$. *Phys. Rev. Lett.*, 102:216804, May 2009.

[23] Luca de' Medici, Gianluca Giovannetti, and Massimo Capone. Selective mott physics as a key to iron superconductors. *Phys. Rev. Lett.*, 112:177001, Apr 2014.

[24] Luca de' Medici, S. R. Hassan, Massimo Capone, and Xi Dai. Orbital-selective mott transition out of band degeneracy lifting. *Phys. Rev. Lett.*, 102:126401, Mar 2009.

[25] Luca de' Medici, Jernej Mravlje, and Antoine Georges. Janus-faced influence of hund's rule coupling in strongly correlated materials. *Phys. Rev. Lett.*, 107:256401, Dec 2011.

[26] G. Deutscher and K. A. Müller. Origin of superconductive glassy state and extrinsic critical currents in high-t_c oxides. *Phys. Rev. Lett.*, 59:1745–1747, Oct 1987.

[27] G. Deutscher and R. W. Simon. On the proximity effect between normal metals and cuprate superconductors. *Journal of Applied Physics*, 69(7):4137–4139, 1991.

[28] D M Duffy. Grain boundaries in ionic crystals. *Journal of Physics C: Solid State Physics*, 19(23):4393, 1986.

[29] D. M. Duffy and A. M. Stoneham. Conductivity and 'negative u' for ionic grain boundaries. 16(21):4087.

[30] J. K. Freericks, M. Jarrell, and D. J. Scalapino. Holstein model in infinite dimensions. *Phys. Rev. B*, 48:6302–6314, Sep 1993.

[31] Antoine Georges, Gabriel Kotliar, Werner Krauth, and Marcelo J. Rozenberg. Dynamical mean-field theory of strongly correlated fermion systems and the limit of infinite dimensions. *Rev. Mod. Phys.*, 68:13–125, Jan 1996.

[32] Antoine Georges, Luca de' Medici, and Jernej Mravlje. Strong electronic correlations from hund's coupling. 4(1):137–178.

[33] P. Hansmann, R. Arita, A. Toschi, S. Sakai, G. Sangiovanni, and K. Held. Dichotomy between large local and small ordered magnetic moments in iron-based superconductors. *Phys. Rev. Lett.*, 104:197002, May 2010.

[34] H. Hilgenkamp and J. Mannhart. Grain boundaries in high-T_c superconductors. *Rev. Mod. Phys.*, 74:485–549, May 2002.

[35] H Hilgenkamp, C W Schneider, B Goetz, R R Schulz, A Schmehl, H Bielefeldt, and J Mannhart. Grain boundary critical currents - a new perspective. *Superconductor Science and Technology*, 12(12):1043, 1999.

[36] J. E. Hirsch and R. M. Fye. Monte carlo method for magnetic impurities in metals. *Phys. Rev. Lett.*, 56:2521–2524, Jun 1986.

[37] J. E. Hirsch and D. J. Scalapino. Excitonic mechanism for superconductivity in a quasi-one-dimensional system. *Phys. Rev. B*, 32:117–134, Jul 1985.

[38] Chia-Ren Hu. Midgap surface states as a novel signature for d^2_{xa}-x^2_b-wave superconductivity. *Phys. Rev. Lett.*, 72:1526–1529, Mar 1994.

[39] H. Ishida and A. Liebsch. Origin of metallicity of $\mathrm{LaTiO_3SrTiO_3}$ heterostructures. *Phys. Rev. B*, 77:115350, Mar 2008.

[40] H. Ishida and A. Liebsch. Embedding approach for dynamical mean-field theory of strongly correlated heterostructures. *Phys. Rev. B*, 79:045130, Jan 2009.

[41] Gun Sang Jeon, Tae-Ho Park, Jung Hoon Han, Hyun C. Lee, and Han-Yong Choi. Dynamical mean-field theory of the hubbard-holstein model at half filling: Zero temperature metal-insulator and insulator-insulator transitions. *Phys. Rev. B*, 70:125114, Sep 2004.

[42] David Kalkenstein and Paul Soven. A green's function theory of surface states. *Surf. Sci.*, 26:85, Jun 1971.

[43] S. S. Kancharla and E. Dagotto. Metallic interface at the boundary between band and mott insulators. *Phys. Rev. B*, 74:195427, Nov 2006.

[44] M. Keller, W. Metzner, and U. Schollwöck. Dynamical mean-field theory for pairing and spin gap in the attractive hubbard model. *Phys. Rev. Lett.*, 86:4612–4615, May 2001.

[45] B. J. Kim, Hosub Jin, S. J. Moon, J.-Y. Kim, B.-G. Park, C. S. Leem, Jaejun Yu, T. W. Noh, C. Kim, S.-J. Oh, J.-H. Park, V. Durairaj, G. Cao, and E. Rotenberg. Novel $J_{\mathrm{eff}} = 1/2$ mott state induced by relativistic spin-orbit coupling in $\mathrm{Sr_2IrO_4}$. *Phys. Rev. Lett.*, 101:076402, Aug 2008.

[46] T. Koida, M. Lippmaa, T. Fukumura, K. Itaka, Y. Matsumoto, M. Kawasaki, and H. Koinuma. Effect of a-site cation ordering on the magnetoelectric properties in $[(\mathrm{LaMnO_3})_m\,/\,(\mathrm{SrMnO_3})_m]_n$ artificial superlattices. 66(14):144418.

[47] K. Maiti and D. D. Sarma. Spectroscopic investigations of the electronic structure and metal-insulator transitions in a mott-hubbard system $\mathrm{la}_{1-x}\mathrm{ca}_x\mathrm{vo}_3$. *Phys. Rev. B*, 61:2525–2534, Jan 2000.

[48] J. Mannhart and H. Hilgenkamp. Possible influence of band bending on the normal state properties of grain boundaries in high-tc superconductors. *Materials Science and Engineering: B*, 56(2 - 3):77 – 85, 1998.

[49] F. Marsiglio, R. Akis, and J.P. Carbotte. Eliashberg theory in the very strong coupling regime. *Physica C: Superconductivity*, 153:223 – 224, 1988.

[50] Cyril Martins, Markus Aichhorn, Loïg Vaugier, and Silke Biermann. Reduced effective spin-orbital degeneracy and spin-orbital ordering in paramagnetic transition-metal oxides: $\mathrm{Sr_2IrO_4}$ versus $\mathrm{Sr_2RhO_4}$. *Phys. Rev. Lett.*, 107:266404, Dec 2011.

[51] Walter Metzner. Linked-cluster expansion around the atomic limit of the hubbard model. *Phys. Rev. B*, 43:8549–8563, Apr 1991.

[52] Walter Metzner and Dieter Vollhardt. Correlated lattice fermions in $d = \infty$ dimensions. *Phys. Rev. Lett.*, 62:324–327, Jan 1989.

[53] D. Meyer, A. C. Hewson, and R. Bulla. Gap formation and soft phonon mode in the holstein model. *Phys. Rev. Lett.*, 89:196401, Oct 2002.

[54] X Montiel and A I Buzdin. On the theory of the proximity effect in atomic scale superconducting/normal metal multilayered structures. *Superconductor Science and Technology*, 26(8):085011, 2013.

[55] A. Muramatsu and W. Hanke. Electron-phonon coupling and pairing in the 2-d hubbard model: A monte-carlo study. *Physica C: Superconductivity*, 153:229 – 230, 1988.

[56] Naoyuki Nakagawa, Harold Y. Hwang, and David A. Muller. Why some interfaces cannot be sharp. 5(3):204–209.

[57] Reza Nourafkan, Massimo Capone, and Nasser Nafari. Surface polaron formation in the holstein model. *Phys. Rev. B*, 80:155130, Oct 2009.

[58] Reza Nourafkan, Frank Marsiglio, and Massimo Capone. Metallic surface of a bipolaronic insulator. *Phys. Rev. B*, 82:115127, Sep 2010.

[59] A. Ohtomo and H. Y. Hwang. A high-mobility electron gas at the LaAlO3/SrTiO3 heterointerface. 427(6973):423–426.

[60] A. Ohtomo, D. A. Muller, J. L. Grazul, and H.Y. Hwang. Artificial charge-modulation in atomic-scale perovskite titanate superlattices. *Nature*, 419, Oct 2010.

[61] Satoshi Okamoto and Andrew J. Millis. Spatial inhomogeneity and strong correlation physics: A dynamical mean-field study of a model mott-insulator–band-insulator heterostructure. *Phys. Rev. B*, 70:241104, Dec 2004.

[62] Satoshi Okamoto and Andrew J. Millis. Theory of mott insulator–band insulator heterostructures. *Phys. Rev. B*, 70:075101, Aug 2004.

[63] R. Pentcheva and W. E. Pickett. Charge localization or itineracy at $\mathrm{LaAlO_3SrTiO_3}$ interfaces: Hole polarons, oxygen vacancies, and mobile electrons. *Phys. Rev. B*, 74:035112, Jul 2006.

[64] Rossitza Pentcheva and Warren E. Pickett. Ionic relaxation contribution to the electronic reconstruction at the n-type $\mathrm{LaAlO_3SrTiO_3}$ interface. *Phys. Rev. B*, 78:205106, Nov 2008.

[65] Rossitza Pentcheva and Warren E. Pickett. Avoiding the polarization catastrophe in $\mathrm{LaAlO_3}$ overlayers on $\mathrm{SrTiO_3(001)}$ through polar distortion. *Phys. Rev. Lett.*, 102:107602, Mar 2009.

[66] Zoran S. Popović, Sashi Satpathy, and Richard M. Martin. Origin of the two-dimensional electron gas carrier density at the $\mathrm{LaAlO_3}$ on $\mathrm{SrTiO_3}$ interface. *Phys. Rev. Lett.*, 101:256801, Dec 2008.

[67] N. Reyren, S. Thiel, A. D. Caviglia, L. Fitting Kourkoutis, G. Hammerl, C. Richter, C. W. Schneider, T. Kopp, A.-S. RÃŒetschi, D. Jaccard,

M. Gabay, D. A. Muller, J.-M. Triscone, and J. Mannhart. Superconducting interfaces between insulating oxides. *Science*, 317(5842):1196–1199, 2007.

[68] S. Robaszkiewicz, R. Micnas, and K. A. Chao. Thermodynamic properties of the extended hubbard model with strong intra-atomic attraction and an arbitrary electron density. *Phys. Rev. B*, 23:1447–1458, Feb 1981.

[69] S. Robaszkiewicz, R. Micnas, and K. A. Chao. Hartree theory for the negative-u extended hubbard model. ii. finite temperature. *Phys. Rev. B*, 26:3915–3922, Oct 1982.

[70] A. Rubano, D. Paparo, F. Miletto, U. Scotti di Uccio, and L. Marrucci. Recombination kinetics of a dense electron-hole plasma in strontium titanate. *Phys. Rev. B*, 76:125115, Sep 2007.

[71] Y. Tanabe S. Sugano and H. Kamimura. Multiplets of transition-metal ions in crystal.

[72] M. Salluzzo, J. C. Cezar, N. B. Brookes, V. Bisogni, G. M. De Luca, C. Richter, S. Thiel, J. Mannhart, M. Huijben, A. Brinkman, G. Rijnders, and G. Ghiringhelli. Orbital reconstruction and the two-dimensional electron gas at the $\mathrm{LaAlO_3SrTiO_3}$ interface. *Phys. Rev. Lett.*, 102:166804, Apr 2009.

[73] M. Salluzzo, J. C. Cezar, N. B. Brookes, V. Bisogni, G. M. De Luca, C. Richter, S. Thiel, J. Mannhart, M. Huijben, A. Brinkman, G. Rijnders, and G. Ghiringhelli. Orbital reconstruction and the two-dimensional electron gas at the $\mathrm{LaTiO_3SrTiO_3}$ interface. *Phys. Rev. Lett.*, 102:166804, Apr 2009.

[74] G. Sangiovanni, M. Capone, C. Castellani, and M. Grilli. Electron-phonon interaction close to a mott transition. *Phys. Rev. Lett.*, 94:026401, Jan 2005.

[75] Giorgio Sangiovanni, Massimo Capone, and Claudio Castellani. Relevance of phonon dynamics in strongly correlated systems coupled to phonons: Dynamical mean-field theory analysis. *Phys. Rev. B*, 73:165123, Apr 2006.

[76] Wolter Siemons, Gertjan Koster, Hideki Yamamoto, Walter A. Harrison, Gerald Lucovsky, Theodore H. Geballe, Dave H. A. Blank, and Malcolm R. Beasley. Origin of charge density at laalo_3 on srtio_3 heterointerfaces: Possibility of intrinsic doping. *Phys. Rev. Lett.*, 98:196802, May 2007.

[77] Manfred Sigrist and T. M. Rice. Unusual paramagnetic phenomena in granular high-temperature superconductors—a consequence of d- wave pairing? *Rev. Mod. Phys.*, 67:503–513, Apr 1995.

[78] M Snoek, I Titvinidze, C Toke, K Byczuk, and W Hofstetter. Antiferromagnetic order of strongly interacting fermions in a trap: real-space dynamical mean-field analysis. *New Journal of Physics*, 10(9):093008, 2008.

[79] Yasutami Takada. Plasmon mechanism of superconductivity in two- and three-dimensional electron systems. *Journal of the Physical Society of Japan*, 45(3):786–794, 1978.

[80] K. S. Takahashi, M. Kawasaki, and Y. Tokura. Interface ferromagnetism in oxide superlattices of camno3/caruo3. *Applied Physics Letters*, 79(9):1324–1326, 2001.

[81] S. Thiel, G. Hammerl, A. Schmehl, C. W. Schneider, and J. Mannhart. Tunable quasi-two-dimensional electron gases in oxide heterostructures. 313(5795):1942–1945.

[82] Irakli Titvinidze, Andrej Schwabe, Niklas Rother, and Michael Potthoff. Dynamical mean-field theory of indirect magnetic exchange. *Phys. Rev. B*, 86:075141, Aug 2012.

[83] Yoshinori Tokura and Takahisa Arima. New classification method for layered copper oxide compounds and its application to design of new high t c superconductors. *Japanese Journal of Applied Physics*, 29(11R):2388, 1990.

[84] A Toschi, P Barone, M Capone, and C Castellani. Pairing and superconductivity from weak to strong coupling in the attractive hubbard model. *New Journal of Physics*, 7(1):7, 2005.

[85] A. Toschi, M. Capone, and C. Castellani. Energetic balance of the superconducting transition across the bcs—bose einstein crossover in the attractive hubbard model. *Phys. Rev. B*, 72:235118, Dec 2005.

[86] C. C. Tsuei and J. R. Kirtley. Pairing symmetry in cuprate superconductors. *Rev. Mod. Phys.*, 72:969–1016, Oct 2000.

[87] D. J. Van Harlingen. Phase-sensitive tests of the symmetry of the pairing state in the high-temperature superconductors—evidence for $d_{x^2-y^2}$ symmetry. *Rev. Mod. Phys.*, 67:515–535, Apr 1995.

[88] V. Vonk, M. Huijben, K. J. I. Driessen, P. Tinnemans, A. Brinkman, S. Harkema, and H. Graafsma. Interface structure of $\mathrm{LaAlO_3SrTiO_3}$ at el-

evated temperatures studied *in situ* by synchrotron x rays. *Phys. Rev. B*, 75:235417, Jun 2007.

[89] Feng Ye, Songxue Chi, Bryan C. Chakoumakos, Jaime A. Fernandez-Baca, Tongfei Qi, and G. Cao. Magnetic and crystal structures of $\mathrm{Sr_2IrO_4}$: A neutron diffraction study. *Phys. Rev. B*, 87:140406, Apr 2013.

[90] Rong Yu and Qimiao Si. Mott transition in multiorbital models for iron pnictides. *Phys. Rev. B*, 84:235115, Dec 2011.

[91] M. P. Zaitlin and A. C. Anderson. Phonon thermal transport in noncrystalline materials. *Phys. Rev. B*, 12:4475–4486, Nov 1975.

[92] Hongbin Zhang, Kristjan Haule, and David Vanderbilt. Effective $j{=}1/2$ insulating state in ruddlesden-popper iridates: An $\mathrm{LDA{+}DMFT}$ study. *Phys. Rev. Lett.*, 111:246402, Dec 2013.

[93] Zhicheng Zhong and Paul J. Kelly. Electronic-structure-induced reconstruction and magnetic ordering at the laalo 3 | srtio 3 interface. *EPL (Europhysics Letters)*, 84(2):27001, 2008.